Spring 2013

Experimental investigation of the turbulent axisymmetric wake with rotation generated by a wind turbine

Nathaniel P. Dufresne

University of New Hampshire, Durham

EXPERIMENTAL INVESTIGATION OF THE TURBULENT AXISYMMETRIC WAKE WITH ROTATION GENERATED BY A WIND TURBINE

BY

Nathaniel P. Dufresne, LTJG, USCG

B.S., NAME, United States Coast Guard Academy, 2009

Submitted to the University of New Hampshire
in partial fulfillment of
the requirements for the degree of

Master of Science

in

Mechanical Engineering

May 2013

UMI Number: 1523788

UMI®

Dissertation Publishing

UMI 1523788

ProQuest®

This thesis has been examined and approved.

Thesis Director, Martin M. Wosnik

Assistant Professor of Mechanical Engineering

M. Robinson Swift

Professor of Mechanical Engineering

Christopher M. White

Associate Professor of Mechanical Engineering

4 / 29 / 2013

Date

DEDICATION

This work is dedicated to my family for their never-ending love, support, and patience.

ACKNOWLEDGMENTS

TABLE OF CONTENTS

LIST OF TABLES

LIST OF FIGURES

ABSTRACT
EXPERIMENTAL INVESTIGATION OF THE TURBULENT AXISYMMETRIC WAKE WITH ROTATION GENERATED BY A WIND TURBINE

by

Nathaniel P. Dufresne, LTJG, USCG

University of New Hampshire, May, 2013

An experimental investigation of the axial and azimuthal (swirl) velocity field in the wake of a single 3-bladed wind turbine with rotor diameter of 0.91m was conducted, up to 20 diameters downstream. The turbine was positioned in the free stream, near the entrance of the 6m x 2.7m cross section of the University of New Hampshire (UNH) Flow Physics Facility. Velocity measurements were conducted at different rotor loading conditions with blade tip-speed ratios from 2.0 to 2.8. A Pitot-static tube and constant temperature hot-wire anemometer with a multi-wire sensor were used to measure velocity fields. An equilibrium similarity theory for the turbulent axisymmetric wake with rotation was outlined, and first evidence for a new scaling function for the mean swirling velocity component, $W_{\max} \propto x^{-1} \propto U_o^{3/2}$ was found; where W represents swirl, x represents downstream distance, and U_o represents the centerline velocity deficit in the wake.

CHAPTER 1

INTRODUCTION

The development and commissioning of sustainable energy technologies at large scale is arguably one of the most important challenges society will face over the next century. Wind energy conversion will undoubtedly play a significant role as an electrical energy source in the future. This is evident by the U.S. Department of Energy's published goal of 20% electrical energy from wind by the year 2030 [46]. The number of land based wind farms in the U.S. has increased dramatically over the last two decades. For example, installed wind power capacity has grown from 2.5 GW in 2000 to 60 GW at the end of 2012 [2]. The electric energy produced from wind has grown from 3.0 TWh in 1991, to 6.7 TWh in 2001, to 119.7 TWh in 2011, when it accounted for 2.9% of electric energy produced in the United States [44]. Most of the land-based wind resource in the United States is located in the central plains. Due to issues associated with electrical energy storage and transmission, land-based wind farms can only play a limited role as a source of electrical energy to the nation's population centers on the coasts.

Offshore wind farms combine a relatively mature energy conversion technology (wind turbines) with the advantages of a favorable wind climate and the ability to locate arrays within close proximity to major load centers. However, offshore wind installations still battle cost issues and there are lessons to be learned from the production data of existing offshore wind farms in Europe (none exist yet in the US). These production data indicate that turbines located downstream of the front row (relative to wind direction), show a significant reduction in energy output when com-

pared to the production of the first row. The associated losses can be dramatic, as shown in Figure 1-1 (from Barthelmie et al. 2009 [4]) for production data from the Danish offshore wind farm Horns Rev 1 (80x Vestas V80-2.0MW turbines, arranged in a slightly skewed 8x10 grid, with 7 diameter, or 560m spacing between turbines). It is clear that energy production falls off significantly downstream of the first row of turbines. Power data was analyzed by [4] for various inflow angles up to $+/-15°$ offset from turbine alignment. Downstream turbines are operating at power outputs of 60% to 80% of the first row. Turbine performance downstream is highly sensitive to alignment with respect to the first row of turbines. This sensitivity to turbine alignment shows that turbine wakes clearly interact with rotors downstream, having a negative effect on performance.
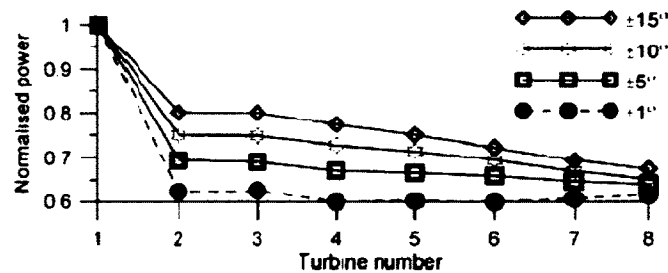
Figure 1-1. Normalized power at each turbine in a central row (West to East) at Horns Rev I, from Barthelmie et al (2009) [4].

The stall condition described by the data in Figure 1-1 was impressively visualized by nature (and a photographer with good timing) when the wind aligned with the wind farm grid and rare atmospheric conditions made the wind turbine wakes visible due to condensation in the lower pressure region downstream of the wind turbine rotor. This was captured in a now well-known photograph, shown in Figure 1-2 [37]. The wakes from the first row of wind turbines, and the compound effect of multiple wind turbine wakes further downstream can clearly be observed.

Figure 1-2. Metoerological conditions at Horns Rev I made the wake effects from upstream wind turbines visually apparent through cloud formation that occurred on 12 February 2008. *Photo courtesy of Vattenfall* [37]

The energy production losses due to wind turbine wake effects, when averaged over a year and all wind directions, typically range from 5% to over 15%, depending on the wind farm layout [32]. However, losses have been measured as high as 20% in large offshore wind farms with regularly-spaced wind turbines [4], [5]. Improved array spacing is necessary to obtain the maximum possible energy output per unit cost (driven by ocean or land area used $[m^2]$) and reduce turbulence loads on downstream rotors. Wind turbine array spacing optimization is still an active research area, e.g. Elkinton et al. [14], since much about the downstream velocity deficit, turbulence intensities, and wake-wake interactions remains unknown. Barthelmie et al. [4] summarize the state of knowledge in modeling and measuring wind turbine wakes in large offshore wind farms as having a "fundamental lack of understanding about the behavior...".

The cost of this limited understanding is significant. For example, consider an offshore wind farm with a capacity factor of 0.4: income loss per year is $3.46M (million) for each percent wake loss per installed GW capacity based on an average retail price of $0.116 per kWh [43]. Further, the increased levels of turbulence created by upstream turbines causes fatigue loading of downstream rotors and play a significant role in turbine service life. Gearboxes with a projected service life of 20 years have been observed to wear out in half that time [29]. The turbulent operating environment results in varying loads, accelerations, and vibration levels that are believed to promote this wear [33].

Vermeer et al. 2003 [48] presented a thorough summary of the numerous wind tunnel studies of wind turbines. However, many of them were either affected by blockage due to small tunnel cross-sectional area or suffered from low Reynolds number due to a small turbine size. In the cases where experiments were conducted with reasonable size turbines in large wind tunnels, detailed flow measurements were typically not conducted sufficiently far downstream, usually due to facility limitations imposed by the test section length or cross section. More recent wind tunnel work focused mainly

4

on the flow dynamics around miniature wind turbines for various array sizes placed in artificially thickened boundary layers, e.g. Lebron et al. 2009 [27], Cal et al. 2010 [7], Chamorro et al. 2011 [10].

Field studies of full scale wind turbines included nacelle-mounted Lidar systems (e.g. Trujillo et al. 2011 [41], Kern et al. 2010) [25], Sodar (e.g., Barthelmie et al. 2005, 2010 [3], [5]) and Sonic Anemometers to characterize the flow (Kelley et al. 2007 [24]), as well as data from meteorological towers (e.g., Vanderwende and Lundquist 2012 [47]). Field experiments have the inherent advantage of being able to directly measure the real world conditions experienced by wind turbines; however, the variability of the atmospheric conditions makes data analysis and interpretation difficult at best, and prevents the full potential of the data acquired this way from being realized. Utility scale wind turbines operate within the earth's atmospheric boundary layer which presents a highly variable inflow. Because of these atmospheric variations, it is usually quite challenging to use the information in order to improve parameterizations, develop scaling laws, and thus develop better numerical models.

To address this lack of data and understanding, a detailed study of wind turbine wakes has been initiated in the Flow Physics Facility (FPF) at the University of New Hampshire. The first stage of the study, reported here, involved measurements of the streamwise and azimuthal velocity components in the wake of a single wind turbine in a free stream. This study was designed to measure the recovery of the streamwise mean velocity deficit, as well as the redistribution and decay of the mean wake rotation introduced by the rotor, at various locations downstream. The goal was to characterize the wind turbine wake in the absence of a turbulent boundary layer inflow and without significant blockage effects, and to gain an understanding whether and when an equilibrium similarity state for the for the turbulent axisymmetric wake with rotation will be reached.

Performing these experiments in the UNH FPF allowed for a comparatively large model wind turbine ($\sim$ 1m diameter) to be used in a controlled environment. This combination of scale and inflow control yielded data sets containing statistics of the recovery of the wake downstream of a single wind turbine, to 20 diameters downstream. These data can be used for the development and validation of analytical and numerical models, and in further studies of wind farm turbulence and array optimization.

CHAPTER 2

THEORY

2.1 Axisymmetric Turbulent Wake Flows

Turbulent wakes are a class of free shear flows, meaning they evolve without the presence of walls – jets and shear layers are the other main classes [38]. Typically, distinct behavior exists for flows of the same class based on geometry (e.g., planar, axisymmetric) and/or wake generator (i.e, initial conditions) and/or Reynolds number.

Axisymmetric wakes have many applications, since any object that moves through a fluid creates a wake: examples include balls (golf, baseball, soccer), projectiles, parachutes, raindrops. Further, if the object is self-propelled, it creates a momentum-less wake; if it is towed, it creates a wake with a velocity deficit. If a device is designed to take energy out of a flow, such as a wind turbine, clearly the wake will have a velocity deficit. Wakes are very complicated flows that are – still – not very well understood. Therefore in most investigations simplified geometries are used, such as the wakes behind spheres or disks. Wakes are difficult to measure under the best of circumstances, especially if one tries to measure beyond the "near-wake", since the mean velocity deficit is very small and slowly decaying, and since turbulence intensities can be of the same order as the deficit.

In the absence of density differences that can add buoyancy force terms, the source of turbulence for the axisymmetric wake is the mean velocity gradient, or, more precisely, the Reynolds stresses working against the mean velocity gradient to produce turbulent kinetic energy (e.g., production terms in equation 5.26, Appendix 1). Tur-

7

bulent free shear flows are also characterized by entrainment, which moves surrounding, irrotational flow into the turbulent, vortical shear flow [38]. This is a general feature of all turbulent shear flows, and it can be shown from the cross-stream momentum equation that the mean pressure inside a turbulent shear flow is modulated by the turbulent stresses and slightly lower than than the reference pressure outside of the turbulent shear flow, therefore causing a weak mean flow towards the turbulent shear flow (c.f., derivation for the axisymmetric wake with swirl in Appendix, or [17]).

An early hot-wire experiment in the wake of an axisymmetric disk was carried out by Carmody in 1964 [9], who made detailed measurements in the wake of an axisymmetric disk wake at a Reynolds number based on diameter and free stream velocity of $Re_D = 70,000$. The wake appeared to be *self-similar* at about 15 diameters from the disk, meaning that the mean velocity profiles appeared to collapse when normalized by the centerline deficit and a lateral length scale determined from the profiles. Carmody's data show significant scatter, presumably due to anemometer limitations at that time. Bevilaqua and Lykoudis [6] investigated the wakes of a porous disk at $Re_D = 510,000$ and reported that it became self-similar in terms of mean velocity and Reynolds stress profiles within twenty diameters. They also measured the wake of a sphere at the same Reynolds number, which evolved to a *different* self-similar state than the porous disk. Cannon [8] investigated the axisymmetric far wake downstream of five different wake generators: a disk, a sphere and three porous disks with varying porosity, all having the same drag and Reynolds number based on the momentum thickness of $Re_\theta \sim U\theta/\nu$ =3500, where U is the free stream velocity, ν is the kinematic viscosity, and θ is the momentum thickness. The wakes had different growth rates, indicating that it is not just downstream distance and drag that dictate the evolution of the wake flow. Both the experiments by Bevilaqua and Lykoudis [6] and Cannon [8] provided evidence that the turbulence does not appear to "forget" how it was created, as commonly stated in text books (e.g, [39], [38]).

Johansson and George (2006) [22] investigated the axisymmetric disk wake with a Reynolds number based on diameter and free-stream velocity of 26,400 in a facility with extremely low background turbulence to downstream distances of $x/D = 150$. Although they worked in a facility with very accurate temperature control (c.f., [23]) using rakes of hot-wire anemometers, they found the influence of the thermal drift of the anemometers to be their greatest challenge to accurately measure the wake, due to the very small centerline velocity deficit and and accompanying low turbulence intensity. They used regression techniques and invoked momentum conservation to rectify the thermal issues, but by doing so were able to obtain results much further downstream than was previously thought possible. The mean streamwise velocity and streamwise turbulence intensity collapse well for $x/D > 30$.

Johansson et al (2003) [21] also demonstrated that the turbulent axisymmetric wake will admit to two different similarity solutions: Following George 1989 [17] they derived a high Reynolds number solution, consistent with the classical scaling of $\delta^* \sim x^{\frac{1}{3}}$ and $U_s = (U_{cl} - U_\infty) \sim x^{-\frac{2}{3}}$, and a low-Reynolds number, viscosity-dominated solution. Since the local Reynolds number of the axisymmetric wake, $Re_\delta = \frac{U_s \delta}{\nu} \sim x^{-\frac{1}{3}}$, decreases slowly, viscous effect will become more important as the wake evolves downstream and the wake will eventually drop out of the high Reynolds number similarity solution. The work by Johansson et al [21] helped explain many of the previous inconsistencies and conclusively showed that initial conditions do affect wake growth rate, contrary to the classical theory.

2.2 Axisymmetric Turbulent Wake with Swirl

The turbulent axisymmetric wake with swirl is also a flow with great practical importance and numerous applications: Any piece of fluid machinery creates a turbulent

9

wake with some swirl component[1]. Investigations of this flow can be distinguished as dealing with fluid power devices, propulsion devices and fundamental studies. Many applied propulsion studies of the swirling wake exist, for example on propellers [42]: A good number of wind turbine wake studies exist, but there seems to be a lack of fundamental studies of the turbulent axisymmetric wake with swirl, with the exception of some early work.

Reynolds [31] correctly derived the traditional high-Reynolds number scaling for the non-swirling wake, but then decided to forgo the mean momentum integral and derived a swirl-dominated wake solution where the swirl decays as $V_s \sim x^{-3/4}$ [31]. Steiger and Bloom [36] derived a linearized solution for swirling wakes which resulted in the the swirl component decaying exponentially.

The difficulty of measuring turbulent axisymmetric wakes with swirl is even greater that that for non-swirling wakes, since now there is also a weak mean azimuthal velocity component on the order of the turbulence fluctuations. Maybe it is this difficulty that has prevented more experimental studies from being carried out. The goal of the experimental measurements reported here was to provide a quality data set for the turbulent axisymmetric wake with rotation. This data set can then also be used to investigate the existence of an equilibrium similarity solution (i.e., test the derived scaling functions) at various locations downstream of the rotor.

2.3   Self-preservation (similarity solutions) of turbulent flows

Self-similarity, or self-preservation, exists when a flow has evolved to a state where profiles can be brought into congruence ("collapsed") using scaling functions which depend only on one of the new similarity variables. The idea of self-preservation

---

[1]Although it can be shown directly from Euler's turbomachinery equation that the hallmark of a well-designed Francis Turbine, for example, should be to have no swirl at its exit and to convert all of the incoming tangential velocity component to shaft work.

in turbulent flows has been around since the 1930s. A new understanding of self-preservation with similarity solutions and scaling functions derived from the conditions for existence of similarity imposed by the governing equations was outlined by George in 1989 [17]. This type of equilibrium similarity has since been applied to free shear flows such as plane and temporal wakes by Ewing (1995) [15], Moser et al. (1998) [28], to axisymmetric wakes by Johansson et al (2003) and Johansson (2002) [21] [20] and to an axisymmetric jet with swirl by Shiri (2010) [34]. The application of a similarity solution for a swirling turbulent wake has not been attempted before to the authors' knowledge. Questions remain with regards to mean axial velocity deficit and azimuthal velocity decay at downstream locations, wake growth, and scaling of turbulence quantities.

2.4 Governing Equations

The theory derived below will follow the approach of previous free shear flow investigation listed above (Johansson 2002, Shiri 2010), beginning with the Reynolds-averaged Navier-Stokes (RANS) equations of motion. The governing equations are derived in Appendix 1, and an order of magnitude analysis is carried out in Appendix 2. The axisymmetric wake coordinates used here are shown in Figure 2-1 as used in Johannson 2002 [20].

The reduced governing equations for the turbulent axisymmetric wake with swirl are as follows. The mean continuity equation reduces to:

$$\frac{\partial U}{\partial x} + \frac{1}{r}\frac{\partial (rV)}{\partial r} = 0 \tag{2.1}$$

The streamwise (x) momentum equation reduces to:

$$U_\infty \frac{\partial (U - U_\infty)}{\partial x} = -\frac{1}{r}\frac{\partial}{\partial r}(r\overline{uv}) + \left\{ \frac{\partial}{\partial x}\left(\overline{v^2} - \overline{u^2} + \int_0^\infty \frac{1}{r}(\overline{w^2} - \overline{v^2}) + W^2 \right) \right\} \tag{2.2}$$
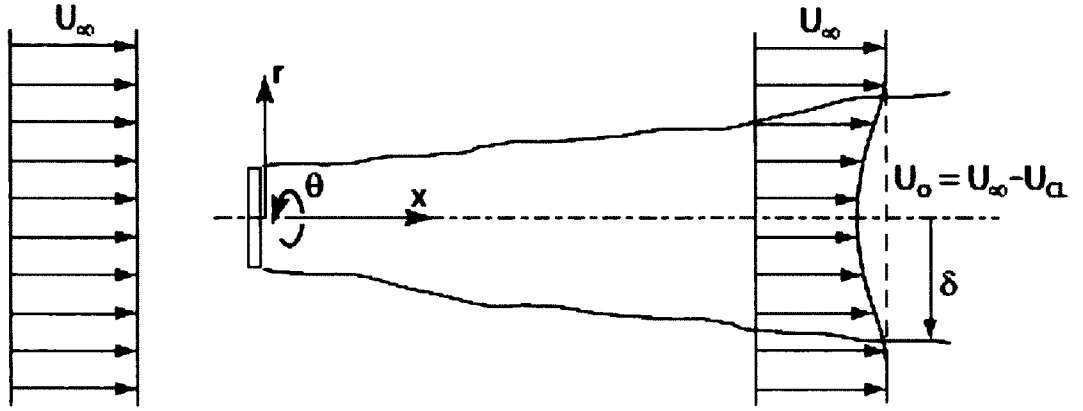
Figure 2-1. Axisymmetric wake coordinates and definitions. U_∞ is the free stream velocity. U_{cl} is the wake centerline velocity. U_o is the centerline wake deficit. δ is the wake half-width. x, r, and θ represent the cylindrical coordinate system of the wake with the origin at the center of the rotor. [20]

Where the terms in curly brackets in the x-momentum equation are of second order, but are kept for now to be able to investigate their contribution to the momentum integral. The radial (r) momentum equation becomes:

$$\frac{1}{\rho}\frac{\partial P}{\partial r} = \frac{W^2}{r} - \frac{\partial \overline{v^2}}{\partial r} + \frac{\overline{w^2} - \overline{v^2}}{r}$$ (2.3)

This can be integrated with respect to r to obtain the mean pressure distribution in the wake. The azimuthal (θ) momentum equation becomes:

$$U_\infty \frac{\partial W}{\partial x} = \frac{1}{r}\frac{\partial}{\partial r}(r\overline{vw})$$ (2.4)

To first order, the leading order inertial term is balanced by the radial gradient of the $\overline{uv}$-Reynolds shear stress (from Appendix 2).

2.4.1 Streamwise and angular momentum conservation

From the governing equations, integral parameters can be derived. One of the two fundamental integrals of the RANS equations for the fully developed turbulent swirling wake is M_x, which is the total rate of transfer of kinematic linear momentum across any downstream plane, say at location x. At high Reynolds numbers this reduces to:

$$M_x(x) = M_o = 2\pi \int_0^\infty \left[U_\infty(U - U_\infty) - \frac{W^2}{2} + \overline{u^2} - \frac{\overline{v^2} + \overline{w^2}}{2} \right] r \, dr \qquad (2.5)$$

Since there are no net forces other than pressure, which is accounted for in the linear momentum equation using a control volume containing the wake generator plane and the wake plane, M_x must remain equal to its source value, which is equal to the net drag imparted by the wake generator, for all downstream positions x.

The second fundamental parameter is the rate at which kinematic angular momentum is swept across any downstream plane, $G_\theta(x)$. From the integration of the angular momentum equation (eqn. 2.4) with the same assumptions as above, this can be shown to reduce to:

$$G_\theta(x) = G_o = 2\pi \int_0^\infty [U_\infty W + \overline{uw}] r^2 \, dr \qquad (2.6)$$

Like the linear momentum, $G_\theta(x)$ should remain constant at its source value, G_o, since in an infinite environment there is no external torque acting on any control volume containing the wake generator plane and any plane downstream perpendicular to the wake axis.

2.4.2 Reynolds stress transport equations

The mean momentum and continuity equations are not sufficient to determine constraints on the similarity solution/scaling functions for all quantities of interest.

Individual Reynolds stress transport equations, and a condition on the pressure-strain-rate terms from continuity (incompressibility) also need to be considered. The transport equation for the Reynolds stress components to first order (after order of magnitude analysis) are as follows:

$\overline{u^2}$ balance

$$U_\infty \frac{\partial}{\partial x}\left(\frac{1}{2}\overline{u^2}\right) = -\overline{uv}\frac{\partial}{\partial r}(U - U_\infty) - \frac{1}{r}\frac{\partial}{\partial r}\left(r\frac{1}{2}\overline{u^2 v}\right)$$
$$+\frac{\overline{p}\frac{\partial u}{\partial x}}{\rho} - \frac{1}{\rho}\frac{\partial}{\partial x}\overline{pu} + \nu\frac{1}{r}\frac{\partial}{\partial r}\left\{r\frac{\partial}{\partial r}\left(\frac{1}{2}\overline{u^2}\right)\right\} - \epsilon_u$$

(2.7)

$\overline{v^2}$ balance

$$U_\infty \frac{\partial}{\partial x}\left(\frac{1}{2}\overline{v^2}\right) = -\frac{1}{r}\frac{\partial}{\partial r}\left(r\frac{1}{2}\overline{v^3}\right) + \frac{\overline{vw^2}}{r} + \frac{\overline{p}\frac{\partial v}{\partial r}}{\rho}$$
$$-\frac{1}{\rho}\frac{\partial}{\partial r}\overline{pv} + \nu\frac{\partial}{\partial r}\left\{\frac{1}{r}\frac{\partial}{\partial r}\left(r\frac{1}{2}\overline{v^2}\right)\right\} - \epsilon_v$$

(2.8)

$\overline{w^2}$ balance

$$U_\infty \frac{\partial}{\partial x}\left(\frac{1}{2}\overline{w^2}\right) = -\frac{1}{r}\frac{\partial}{\partial r}\left(r\frac{1}{2}\overline{uw^2}\right) - \frac{\overline{vw^2}}{r}$$
$$+\nu\frac{\partial}{\partial r}\left\{\frac{1}{r}\frac{\partial}{\partial r}\left(r\frac{1}{2}\overline{w^2}\right)\right\} - \epsilon_w$$

(2.9)

$\overline{uv}$ balance

$$U_\infty \frac{\partial}{\partial x}(\overline{uv}) = -\overline{v^2}\frac{\partial}{\partial r}(U - U_\infty) - \frac{1}{r}\frac{\partial}{\partial r}\left(r\overline{uv^2}\right) + \frac{\overline{uw^2}}{r}$$
$$+\frac{\overline{p\left(\frac{\partial u}{\partial r} + \frac{\partial v}{\partial x}\right)}}{\rho} - \frac{1}{\rho}\left(\frac{\partial}{\partial r}\overline{pu} + \frac{\partial}{\partial x}\overline{pv}\right)$$
$$+\nu\frac{\partial}{\partial r}\left\{\frac{1}{r}\frac{\partial}{\partial r}\left(r\frac{1}{2}\overline{uv}\right)\right\} - \epsilon_{uv}$$

(2.10)

14

2.5 Similarity Solution

Similarity solutions are now substituted into all governing equations derived above. The similarity solutions are products of scaling functions which depend only on streamwise location, and similarity profiles which depend on a new similarity variable and possibly initial conditions. An important difference to the classical analysis of turbulent shear flows, e.g. [39], is that scaling functions are not assumed a priori, but will be determined from conditions on the existence of similarity solutions derived from the governing equations. The similarity functions will be of the following form:

$$U - U_\infty = U_s(x)f(\eta, *); \quad -\overline{uv} = R_{s,uv}(x)g(\eta, *)$$

$$W = W_s(x)h(\eta, *); \quad -\overline{uw} = R_{s,uw}(x)i(\eta, *)$$

$$\tfrac{1}{2}\overline{u^2} = K_u(x)k_u(\eta, *); \quad \tfrac{1}{2}\overline{v^2} = K_v(x)k_v(\eta, *)$$

$$\tfrac{1}{2}\overline{w^2} = K_w(x)k_w(\eta, *); \quad \tfrac{1}{2}\overline{u^2 v} = T_{u^2 v}t_{u^2 v}(\eta, *) \tag{2.11}$$

$$\overline{\tfrac{p}{\rho}\tfrac{\delta u}{\delta x}} = P_u(x)p_u(\eta, *); \quad \tfrac{1}{\rho}\overline{pu} = P_u^D(x)p_u^D(\eta, *)$$

$$\varepsilon_u = D_u(x)d_u(\eta, *)$$

where $\eta = r/\delta(x)$ and (*) denotes a dependence on initial conditions (wake generator, e.g., turbine type and operating condition). After substituting the similarity solutions and clearing terms, the x-momentum equation takes the following form

$$\left[\frac{\delta}{U_s}\frac{dU_s}{dx}\right]f - \left[\frac{d\delta}{dx}\right]\eta f' = \left[\frac{R_{s,uv}}{U_\infty U_s}\right]\frac{(\eta g)'}{\eta} + \left[\frac{\nu}{U_\infty \delta}\right]\frac{(\eta f')'}{\eta} \tag{2.12}$$

where the terms in square brackets depend on downstream position x only, and the non-bracketed terms depend on the new similarity variable only. In order for a similarity solution to exist, all bracketed terms must have the same x-dependence. This

15

can be further simplified with the momentum integral and $\delta \equiv \delta_*$ and $U_s \equiv U_o = (U_\infty - U_{cl})$:

$$U_s \delta^2 \int_0^\infty f\eta d\eta = U_\infty \theta^2 \quad \rightarrow \quad \frac{U_s}{U_\infty} = \left[\frac{\theta}{\delta_*}\right]^2 \tag{2.13}$$

resulting in:

$$-\left[\frac{d\delta}{dx}\right](\eta^2 f)' = \left[\frac{R_{s,uv}}{U_\infty U_s}\right]\frac{(\eta g)'}{\eta} + \left[\frac{\nu}{U_\infty \delta}\right]\frac{(\eta f')'}{\eta} \tag{2.14}$$

Substitution of similarity solutions in the the Reynolds stress component equations and clearing terms leads to the following equations:

Streamwise normal stresses:

$$\left[U_\infty \frac{dK_u}{dx}\right]k_u - \left[\frac{U_\infty K_u}{\delta}\frac{d\delta}{dx}\right]\eta k_u' = -\left[\frac{R_{s,uv}U_s}{\delta}\right]f' - \left[\frac{T_{u^2 v}}{\delta}\right]\frac{(\eta t_{u^2 v})'}{\eta}$$
$$+ \left[\frac{dP_u{}^D}{dx}\right]p_u{}^D - \left[\frac{P_u{}^D}{\delta}\frac{d\delta}{dx}\right]\eta(p_u{}^D)' + \left[\frac{\nu K_u}{\delta^2}\right]\frac{(\eta k_u')'}{\eta} - [D_u]d_u \tag{2.15}$$

Radial normal stress equation:

$$\left[U_\infty \frac{dK_v}{dx}\right]k_v - \left[\frac{U_\infty K_v}{\delta}\frac{d\delta}{dx}\right]\eta k_v' = -\left[\frac{T_{v^3}}{\delta}\right]\frac{(\eta t_{v^3})}{\eta} + \left[\frac{T_{vw^2}}{\delta}\right]\frac{t_{vw^2}}{\eta}$$
$$+ [P_v]p_v + \left[\frac{P_v{}^D}{\delta}\right](p_v{}^D)' + \left[\frac{\nu K_v}{\delta^2}\right]\frac{(\eta k_v')'}{\eta} - [D_v]d_v \tag{2.16}$$

Angular normal stress equation:

$$\left[U_\infty \frac{dK_w}{dx}\right]k_w - \left[\frac{U_\infty K_w}{\delta}\frac{d\delta}{dx}\right]\eta k_w' = -\left[\frac{T_{uw^2}}{\delta}\right]\frac{(\eta t_{uw^2})}{\eta}$$
$$+ \left[\frac{T_{vw^2}}{\delta}\right]\frac{t_{vw^2}}{\eta} + \left[\frac{\nu K_w}{\delta^2}\right]\frac{(\eta k_w')'}{\eta} - [D_w]d_w \tag{2.17}$$

(uv) Reynolds shear stress equation:

$$-\left[u_\infty \frac{dR_{s,uv}}{dx}\right]g - \left[\frac{U_\infty R_{s,uv}}{\delta}\frac{d\delta}{dx}\right]\eta g' = \left[\frac{K_v U_s}{\delta}\right]f'k_v - \left[\frac{T_{uv^2}}{\delta}\right]\frac{(\eta t_{uv^2})'}{\eta}$$

$$+\left[\frac{T_{uw^2}}{\delta}\right]\frac{t_{uw^2}}{\eta} + [P_{uv}]p_{uv} - \left[\frac{P_u^D}{\delta}\right](p_u^D)' - \left[\frac{dP_v^D}{dx}\right](p_v^D) \qquad (2.18)$$

$$-\left[\frac{P_v^D}{\delta}\frac{d\delta}{dx}\right]\eta(p_v^D)' - \left[\frac{\nu R_{s,uv}}{\delta^2}\right]\left(\frac{(\eta g)'}{\eta}\right)' - [D_{uv}]d_{uv}$$

Conditions for the existence of similarity

From the equations above , the conditions for the existence of similarity solutions are, from x-momentum:

$$\left[\frac{\delta}{U_s}\frac{dU_s}{dx}\right] \sim \left[\frac{d\delta}{dx}\right] \sim \left[\frac{R_{s,uv}}{U_\infty U_s}\right] \sim \left[\frac{\nu}{U_\infty\delta}\right] \qquad (2.19)$$

Here the symbol " $\sim$ " means "has the same x-dependence as." From the first and second terms, it can be seen that the Reynolds stress scaling function depends on the growth rate of the wake.

$$R_{s,uv} \sim U_\infty U_s \frac{d\delta}{dx} \qquad (2.20)$$

contrary to traditional wake analyses, e.g. [39, 38]. From the transport equation for the streamwise normal stresses we find the following conditions:

$$\frac{\delta}{K_u}\frac{dK_u}{dx} \sim \frac{d\delta}{dx} \sim \frac{T_u\delta}{U_\infty K_u} \sim \frac{D_u\delta}{U_\infty K_u} \sim \frac{\nu}{U_\infty\delta} \qquad (2.21)$$

A similarity solution, for large local Reynolds number, $U_\infty\delta/\nu$, (viscosity is identically equal to zero) is only possible if:

$$\frac{d\delta}{dx} \sim \frac{D_u\delta}{U_\infty K_u} \qquad (2.22)$$

17

From the other Reynolds stress transport equations, the remaining constraints are found:

$$K_u \sim K_v \sim K_w \sim U_s{}^2$$
$$D_u \sim D_v \sim D_w \sim \frac{U_s{}^3}{\delta} \tag{2.23}$$

When considering all of the constraints above, it can be shown that the mean flow has similarity solution with scaling functions of the following form:

$$\frac{\delta_*}{\theta} = a\left[\frac{x-x_o}{\theta}\right]^{\frac{1}{3}} \tag{2.24}$$

$$\frac{U_s}{U_\infty} = b\left[\frac{x-x_o}{\theta}\right]^{-\frac{2}{3}} \tag{2.25}$$

These are the same as in the classical solution, e.g. Johansson et al. (2003) [21], but the scaling functions for higher moments (Reynolds stresses etc) are shown to be more complicated by Johansson et al. 2003. Also, since the axisymmetric turbulent wake is a flow with diminishing local Reynolds number $(U_s\delta_*/\nu)$, as can be seen from the scaling function above, the flow will eventually "fall out" of this infinite Reynolds number, viscosity-independent similarity solution, but may arrive at another, viscous-dominated low-Reynolds number similarity solution [21].

Effects of Swirl

To investigate the behavior of the swirling component of mean velocity, we now also consider the $W, <uw>, <vw>$ equations. The rate at which kinematic angular momentum is swept downstream (from integrated angular momentum equation) can be written as

$$G_\theta(x) = G_o = 2\pi \int_0^\infty [U_\infty W + \overline{uw}]r^2 dr \tag{2.26}$$

18

Note that the extraction of linear momentum and the addition of angular momentum impose an additional length scale (from the source conditions) as $L_* = G_o/M_o$. We can neglect the $< uw >$-term and substitute the similarity solutions.

$$G_x = [U_\infty W_{max} \delta_*^3] 2\pi \int_0^\infty f\ g\ \eta^2 d\eta \qquad (2.27)$$

With $\delta^* \sim x^{\frac{1}{3}}$ and $U_\infty =$ constant, the azimuthal velocity has to decay as

$$\frac{W_s}{U_\infty} = \left[\frac{x - x_o}{\theta}\right]^{-1} \qquad (2.28)$$

In general, it should be noted that properly normalized mean velocity profiles always collapse, and the source-dependent differences will show up in the wake spreading rate and the higher turbulent moments. If a numerical model for the axisymmetric, turbulent, swirling wake cannot reproduce scaling behavior predicted by an equilibrium similarity solution, then it is not capturing the essential wake physics.

CHAPTER 3

EXPERIMENTS

3.1 Experimental Facility

The UNH Flow Physics Facility (FPF) is the worlds largest flow-physics-quality turbulent boundary layer wind tunnel. The test section has a width of 6 m, height of 2.7 m, and length of 72 m. The tunnel height increases downstream in order to compensate for the growing boundary layers and maintain a zero pressure gradient throughout the test section. The facility has been undergoing extensive qualification measurements since it became operational in the fall of 2010 [49]. In its present configuration (construction phase 1, open circuit), test section velocities of up to 14 m/s can be achieved and free stream turbulence intensities of less than 0.5% are attained at all downstream tunnel locations. Spanwise variation in mean wall shear stress was shown to be $+/-1\%$ when outside the effects of the side wall boundary layers [16]. The FPF was designed to investigate high Reynolds number turbulent boundary layers with adequate spatial resolution. It can achieve Reynolds numbers, expressed as scale ratios of $\delta^+ = \delta u_\tau / \nu \approx 20,000$. The appropriate boundary layer heights measured on the floor of the FPF at each downstream location are shown in Table 3.1. For a boundary layer height $\delta = 1m$ at a $\delta^+ \approx 20,000$, the viscous length scale is found to be $\eta = \nu / u_\tau = 50 \mu m$, within what can be measured with state-of-the-art flow measurement techniques.

The large cross-sectional area allows the use of a model rotor of diameter up to 1 m, while maintaining a blockage ratio of less than 5% based on swept area. Testing of larger turbines is possible depending on experimental goals with regards

Table 3.1. Boundary layer height based on downstream location in the UNH FPF as measured by Vincenti et al. [49]

Downstream Location	Boundary Layer Height	Test Section Velocity
4 (m)	.08 (m)	7 (m/s)
8 (m)	.14 (m)	7 (m/s)
16 (m)	.24 (m)	7 (m/s)
32 (m)	.43 (m)	7 (m/s)
66 (m)	.73 (m)	7 (m/s)

to measurements in the far wake. The large cross-section and length of the test section allow measurements to be taken far downstream without interference from the boundary layers on the walls. The large scale models permitted by this facility allow for higher resolution wake measurements; using a larger wake generator inherently increases the Kolmogrov length scales (smallest scales of turbulent motion) in the wake [11]. This improves the spatial resolution of traditional measurement techniques.

3.2 Wake Generator-Model Wind Turbine

A Rutland 910 Windcharger turbine, manufactured by Marlec Engineering Co Ltd., was used as the wind turbine model for turbulent wake measurements, and as the "swirling wake generator." The turbine has a rotor diameter of 0.91 m and uses an AC generator with dual rectifiers to provide a DC power supply of 24V. The turbine can accommodate up to six airfoil blades, which can be inserted into the molded hub (which encompasses the entire generator assembly). The device was tested with three blades in order to better simulate the swirl induced by tip vortices on utility-scale wind turbines (which are commonly three blade designs). Wake measurements were taken up to 20 rotor diameters downstream of the test device, which adequately covers the range of reasonable spacing for wind turbine arrays.

An adjustable resistive load bank was used to vary the rotor loading configuration. With zero load on the device, rotation rates of up to 415 rotations per minute

(rpm) were achieved with an inflow velocity of 7 m/s. Rotation rates were measured using a Monarch Instruments ROLS-W sensor with a Monarch Instruments ACT-1B tachometer. This sensor uses a class 2 laser beam with a continuous pulse duration and a speed range of 1-250,000 rpm.

The turbine was placed 5 m downstream of the FPF inlet and turbulence management section. This distance was chosen as a conservative downstream location to ensure sufficient decay of grid turbulence generated by the turbulence management section at the inlet, but also remains close enough to the tunnel inlet to avoid any wake interactions with naturally grown wall-bounded flows within the area of concern. The hub height was exactly centered between the floor and ceiling of the test section at 1.35 m. This resulted in a 0.9 m ($x/D = 1$) distance from the blade tips to the ceiling (or floor). The distance from the blade tips to the side walls was 2.55 m ($x/D = 2.8$). The turbine was mounted on a single section of 1.5 inch black iron pipe. This minimized the impact that the mounting system had on the wake. The test device is shown in the test section in Figure 3-1. An illustration of the model turbine with the traversing system and hot-wire probe is shown in Figure 3-2. A 40x zoom of the hot-wire probe is shown in order to clarify probe orientation with respect to the turbine.

Dynamic similarity is achieved when the ratio of inertial and viscous forces, or chord Reynolds number (Re_c) and relative velocity vector diagrams, i.e., the tip speed ratio (TSR) of model and prototype device are the same. Reynolds number similarity can often not be achieved, since for geometrically similar models with scale ratio $L_r = D_{prototype}/D_{model}$ it would require to run the model test at L_r times the free stream velocity (and rotate at L_r^2 times the RPM of the prototype for full similarity). However, a threshold value for the Reynolds number should be exceeded to ensure that the turbine operates in the right flow regime to capture the essential turbine physics. Here, the rotor was driven by the flow, hence it was not possible to match the blade
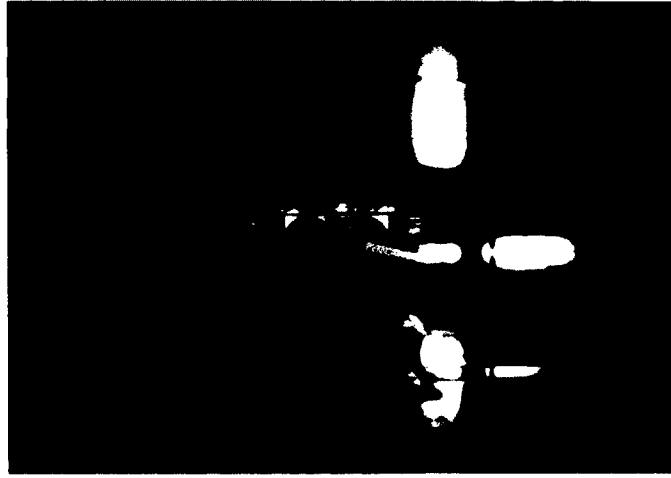
Figure 3-1. Experimental setup: model wind turbine in test section of UNH Flow Physics Facility. This view is looking downstream at the rotor with the wind tunnel drive fans in the background.
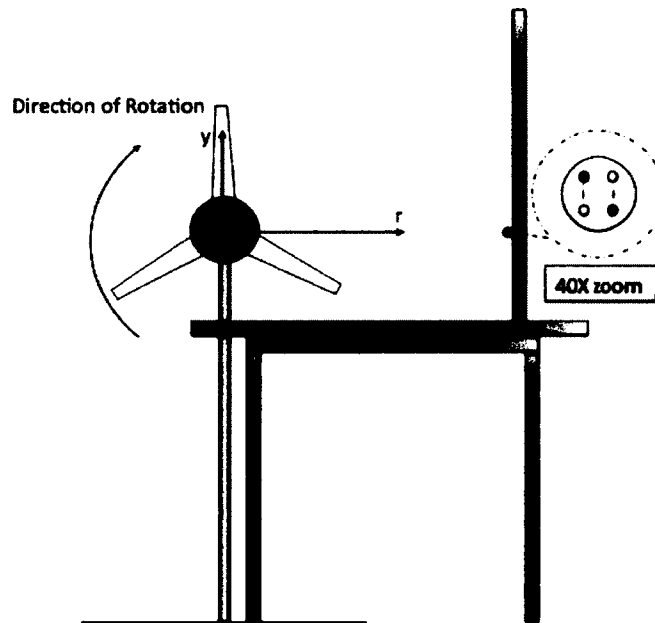
Figure 3-2. Illustration of model wind turbine in the foreground with traversing system in the background. The sensor was traversed outward (radially) from the center of the turbine parallel to the floor. A zoomed in illustration of the X-wire shows orientation with respect to the test device in order to capture the streamwise and azimuthal velocities. Based on the traversing direction, azimuthal velocity will be seen in the wall normal direction.

tip Reynolds number of the model to a full scale turbine. Kinematic similarity of velocity vector diagrams required that the tip speed ratio, which is the ratio between the rotational velocity of the blade tip and the incoming flow and is represented by the variable $\lambda = \frac{\omega R}{U_\infty}$, of model and prototype is matched.

This is a more achievable value given the maximum rotation rate of the test device used. Experimental results provided here were obtained using λ values ranging from 2.0 to 2.8. At 7 m/s , the Reynolds numbers based on relative velocity and chord at the blade tip ($c = 0.04$m), $Re_c = \frac{w_{rel}c}{\nu}$, ranged from approximately 46,000 to 62,000 [1]. The Reynolds numbers based on turbine diameter was approximately 475,000. The Reynolds number based on chord length, Re_c, is important for turbine performance and near-wake whereas the Reynolds number based on diameter, Re_D, is important for overall wake behavior and array spacing. Table 3.2 shows the non-dimensional Reynolds number based on various length scales for each tip-speed ratio.

A plan view of the experimental setup with measurement positions is shown in Figure 3-3. A flow sensor was positioned downstream of the turbine using a stream-lined 2-dimensional traversing system. Two Velmex, Inc. Bi-slides were used to create a 1.3 m^2 coverage area in a plane parallel to that of the turbine. Phidgets, Inc. model #1063 stepper motor controllers were used to control the movement of the traversing system. Foil shape sections were designed to mount directly to the Bi-slide traversing frame in order to reduce traverse blockage and interference with the sensor. A hot-wire sensor can be seen mounted to the Bi-slide in Figure 3-4. This view is looking directly downstream, in the background are the tunnel drive fans located in the plenum. The fans are twin Aerovent 4 VJ fans and are powered by ABB ACS800-37 Variable Frequency Drive (VFD) systems rated at 400 horsepower each.

---

[1] Relative velocity w_{rel} was obtained from a vector addition of free stream velocity, U_∞, and rotational velocity, ωR
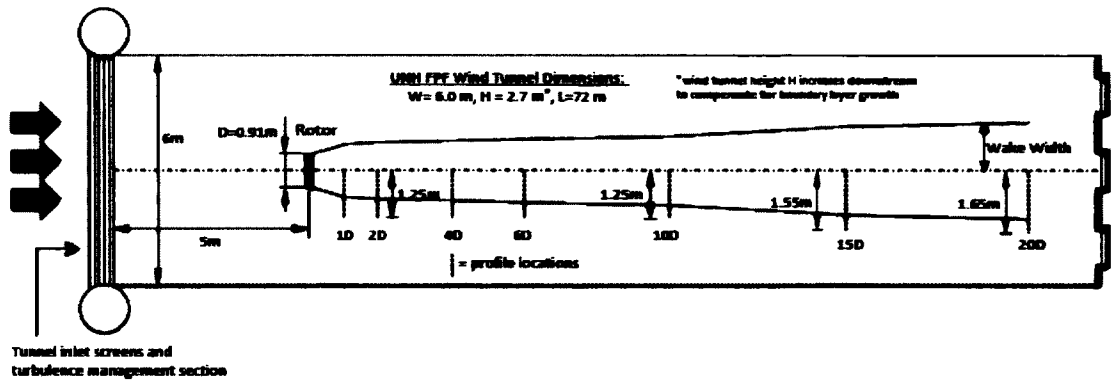
Figure 3-3. Plan view of experimental setup in the UNH Flow Physics Facility. The turbine is positioned $5m$ from the tunnel inlet. Measurement locations are shown at seven locations downstream of the turbine and normalized by turbine diameter.

3.3 Experimental Techniques

3.3.1 Pitot-Static Tube

Initial flow measurements were performed using a pitot-static tube with a 0.635 cm outer diameter. The pitot-tube was traversed through the rotor wake at multiple downstream locations to determine the mean streamwise velocity deficit at each location. A pitot-static tube uses a stagnation pressure port and a static pressure port to capture a pressure difference (= dynamic pressure ($\frac{1}{2}\rho v^2$)), which can then be converted to a velocity for a given temperature and barometric pressure.

An MKS Baratron type 270 high accuracy pressure transducer with a range of 10 torr (1.33 kPa) was used to measure the differential pressure. Limitations of pitot-static tube measurements include the inability to capture turbulent fluctuations. The transducer itself is capable of very high sampling rates, however the pressure

Table 3.2. Reynolds number based on chord length at various radial locations and Reynolds number based on rotor diameter.

Tip-Speed Ratio	Radial Position	$Re_c = \frac{w_{rel}c}{\nu}$	$Re_c = \frac{w_{rel}c}{\nu}$
2.0	r=12 cm	43,850	472,000
2.0	r=24 cm	46,800	472,000
2.0	r=36 cm	48,100	472,000
2.0	r=45.5 cm	45,900	472,000
2.5	r=12 cm	46,700	472,000
2.5	r=24 cm	53,900	472,000
2.5	r=36 cm	57,800	472,000
2.5	r=45.5 cm	56,200	472,000
2.8	r=12 cm	48,500	472,000
2.8	r=24 cm	58,200	472,000
2.8	r=36 cm	63,500	472,000
2.8	r=45.5 cm	62,150	472,000

Figure 3-4. Hot-wire sensor mounted to the Velmex Bi-Slide traversing system in the test section of the UNH Flow Physics Facility. The tunnel drive fans can be seen in the background. The traverse has airfoil inserts (NACA 0024) to reduce measurement interference.

fluctuations are damped by the air column in the tubing that connects the pitot-static tube to the transducer, eliminating the possibility of accurately measuring velocity fluctuations.

3.3.2 Hot-Wire Anemometry

In order to capture the velocity fluctuations due to the eddies in the turbulent flow, it was necessary to use a measurement technique that can temporally resolve rapid changes in velocity. A hot-wire anemometer is very sensitive to rapid fluctuations in velocity and its small sensing element offers little disturbance to the flow. Hot-wire anemometers use a very thin wire, which is welded to prong supports and then placed in the flow in an orientation where the active sensing region of the wire is exposed to the dominant flow direction(s). Here a constant temperature hot-wire anemometry system was used. The temperature of the wire is held constant by a variation in current, which corresponds to a change in wire resistance caused by the convective cooling of the wire by the flow. Higher fluid velocities result in a higher rate of cooling. The electronic circuitry of the anemometer maintains the temperature of the wire, and is therefore sensitive to the rate of cooling. This is then translated to a voltage output, which has a non-linear relationship with the fluid velocity.

The results shown here were obtained using an AA Lab Systems model AN-1003 10-channel Constant Temperature Hot-Wire Anemometer. After proper calibration, this system has the ability to measure fluid velocities with accuracy up to 0.005% (for single wires). The response time between measurement and instrument output can reach a minimum of 1.2 μs [1]. To capture two components of velocity, the sensor uses two 5 μm diameter tungsten wires with an exposed length of 1 mm. For an 'X'-wire, the wires are arranged in a configuration that enables two components of velocity to be measured simultaneously. This is accomplished by comparing the output voltages

of both wires with those of the voltages obtained during calibration with a known inflow magnitude and direction.

The hot-wire sensors that were used in these experiments were constructed in-house at the University of New Hampshire. They consist of three basic parts: the probe, prongs, and sensing wire. The probe is isolated from the anemometer circuitry and acts as a rigid way to mount the sensing element(s). There are two prongs per sensing element, which are soldered to wires inside the probe. The wires connect to individual anemometer channels via BNC connectors and are thus part of the circuit which delivers current to and from the sensing element. The sensing element is a 5 μm in diameter tungsten wire which is soldered to each prong to complete the circuit. The tungsten does not easily solder to the stainless steel prongs therefore it is copper plated at both ends, where it will attach to the prongs, leaving a 1 mm section uncoated to act as the sensing region. The increased diameter and thermal insulation of the copper plating makes the plated area relatively insensitive to changes in flow velocity. This allows the length of wire which is sensitive to the flow (known as the active sensing region) to be precisely controlled, by plating everything except for a small standardized section of wire. Maintaining a standard length for the active sensing region provides consistent measurements and electrical characteristics between sensors. This standardization makes individual sensors behave similarly with each anemometer channel. The copper plating is accomplished using the electroplating process. Electroplating (or electrodeposition) uses electrical current to produce a metallic coating on a surface, by negatively charging the surface to be plated and submerging it into a solution containing positively charged metallic ions [13].

The wire mounting apparatus can be seen in Figure 3-5. The tungsten wire is taped to the u-shaped section of stainless steel (labeled 'A' in Figure 3-6), which then threads into a mounting post on a micro traverse. This allows the wire to be articulated throughout the apparatus with precision movements. The wire is first

28

positioned over the plating channels (labeled 'B' in Figure 3-6). The channels lead to two pools which are machined with 1 mm separation. This separation zone will be the length of the active sensing region of the wire. The pools and channels are filled with a copper sulfate solution which is detailed in Table 3.3. The copper electrodes which run through the channels are part of the plating circuit shown in Figure 3-7. The tungsten wire is submerged in the copper sulfate solution to complete the circuit. This can be seen in Figure 3-8.
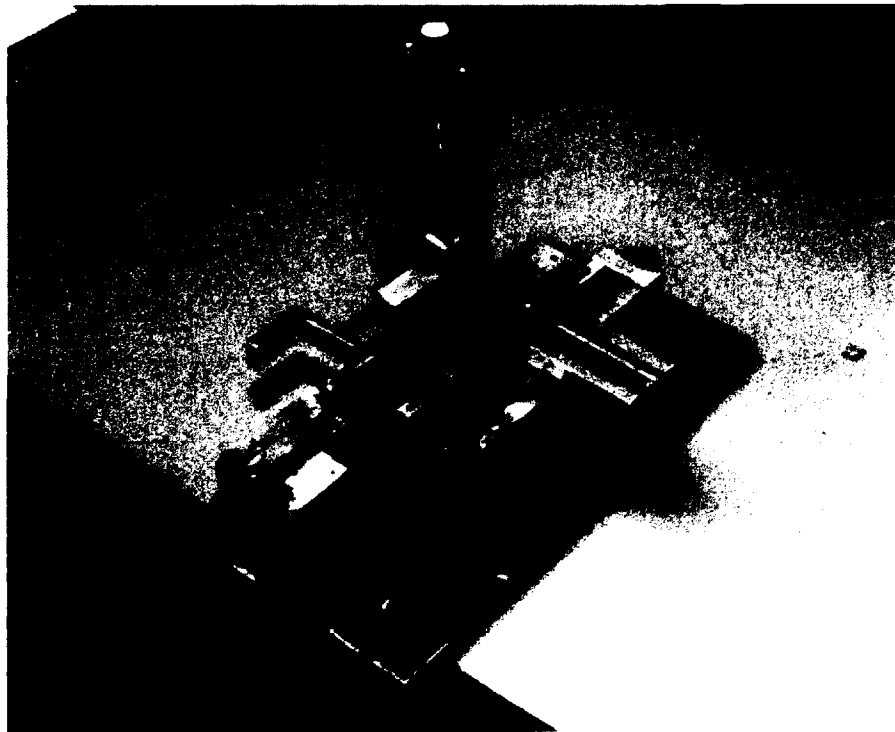
Figure 3-5. Hot-wire mounting apparatus. A 3-axis micro traverse is used to position the tungsten wire for copper plating and soldering to the prong tips.

It has been observed that when approximately 6.22 Joules pass through the plating circuit, the resultant plating diameter is approximately 50 μm which yields an approximate cold wire resistance of 3.5 Ω. This cold wire resistance has been shown through previous experiments by Vincenti et al. 2012 [49] to perform well with the AA Labs AN-1003 Anemometer. The plating process takes exactly 10 minutes. After

Figure 3-6. Tungsten wire holder (A) and copper plating pools (B). The micro traverse positions the wire over the plating pools (submerging the wire in the copper sulfate), which completes the electroplating circuit.

Table 3.3. Copper Sulfate Solution used during the sense wire electroplating process

Quantity	Ingredient	Notes
100 ml	Distilled H_2O	Room Temperature
25 g	Copper(II) sulfate pentahydrate	CuSO4 5H20
3.5 ml (6.44 g)	Sulfuric Acid	> 95% purity

plating is complete, the channels can be removed from the mounting apparatus and replaced with the probe. It is essential that the prongs be thoroughly cleaned prior to soldering. Stainless steel flux is used in conjunction with lead tin (37/63) solder to mount the wire to the prongs. The soldering is done by hand with a Weller soldering iron. Proper contact is verified using a multimeter to measure the resistance across the prongs. An image of the plated wire ready for soldering can be seen in Figure 3-9.

The multi-wire probe uses one long and one short prong for each wire to allow the wires to be mounted at a 45° angle (X-wire). The wires are oriented opposite of each other, which allows two components of velocity to be determined. Because an

30

87.4 kΩ

Wire
Holder

30V
DC

+

-

Plating
Pools
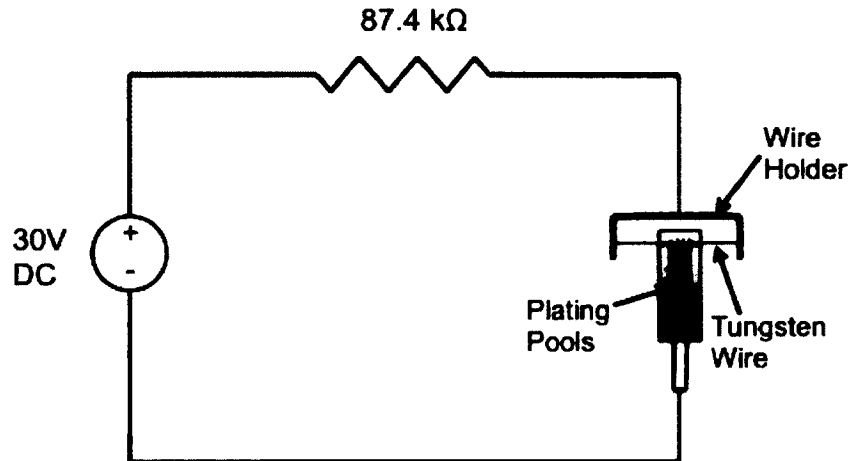
Tungsten
Wire

Figure 3-7. Electroplating circuit used to copper plate the ends of the tungsten wire for soldering to the prong tips.

individual hot-wire is not sensitive to the direction of flow (only the overall convective cooling), it is important that the flow and experimental conditions are well understood prior to orienting the probe. The X-wire probe needs to be oriented in a manner where the wires are sensitive to the inflow angle of the resultant velocity vector, which will allow that resultant vector to be broken down into two components of velocity. If there is a significant contribution from a third component of velocity, the sensor will not be able to differentiate the cooling effects from the two dominant velocity components with that of the third. This requires the assumption that there are only two dominant directions of flow and that the probe is oriented in a manner that will allow differences to be seen in the convective cooling rates of each wire with changes in the mean flow direction as can be seen in Figure 3-10.

The calibration of the multi-wire sensors was performed in situ with an articulating jet, which has the ability to adjust the mean flow $+/-30°$ in any direction. The calibration unit is capable of adjusting the jet outlet velocity in increments of 0.01 m/s up to 15 m/s. The sensor used here was calibrated at velocities of 2, 4, 6, 8, and 10 m/s and inflow angles of $+30°$ to $-30°$ in 5° increments. This covers the range of

Figure 3-8. Tungsten wire immersed in copper sulfate solution during electroplating process. *Image courtesy of Paschal Vincenti.*

speeds and inflow angles that the sensor will encounter during the experiment. The calibration jet can be seen in Figure 3-11.

The non-linear relationship between anemometer voltage output and velocity over the wire can be inferred from the calibration. This relationship can then be interpolated for each voltage output during the experiment to determine velocity. Thermal changes over the course of an experiment can cause anemometer output voltages to drift and no longer properly correspond with the voltages obtained during calibration for a particular inflow vector. For this reason, hot-wire calibrations should be performed before and after each experiment and then interpolated based on temperature variation, if temperature can not be highly controlled, to give a more accurate voltage to velocity relationship for the experimental measurements. This does however impose some uncertainty on the measurement results.
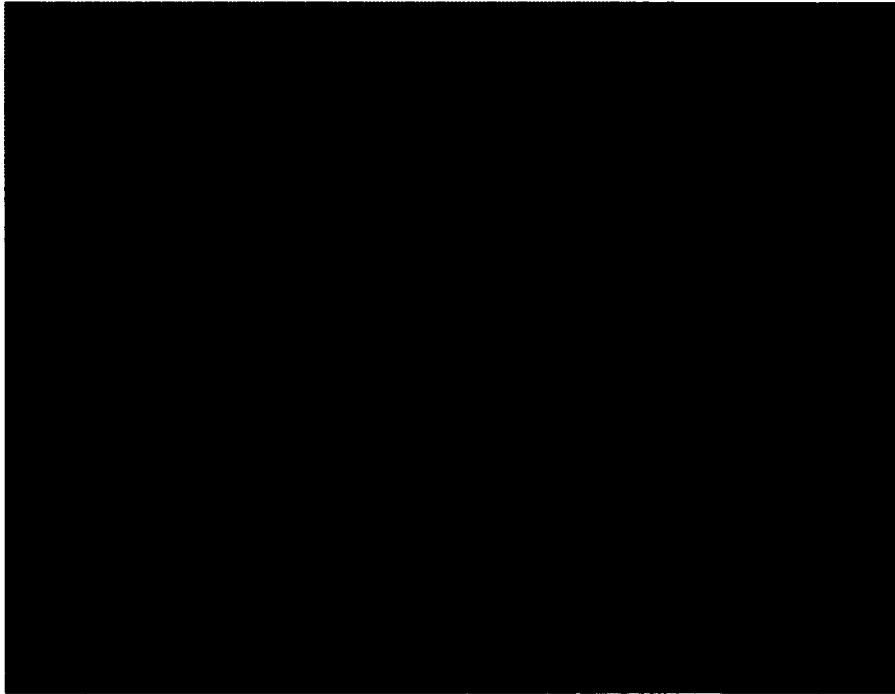
Figure 3-9. Tungsten wire after being plated is ready for mounting to the probe. *Image courtesy of Paschal Vincenti.*
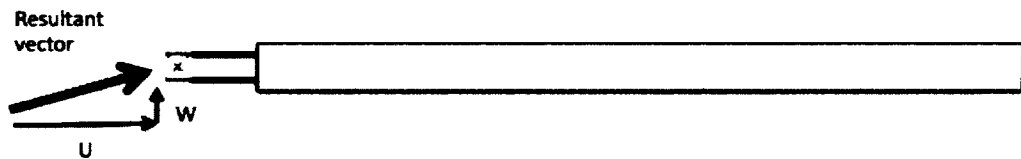
Figure 3-10. Diagram illustrating the dominant flow directions that can be resolved with an X-wire. The U component shown here represents the streamwise velocity and the W component represent the azimuthal velocity.
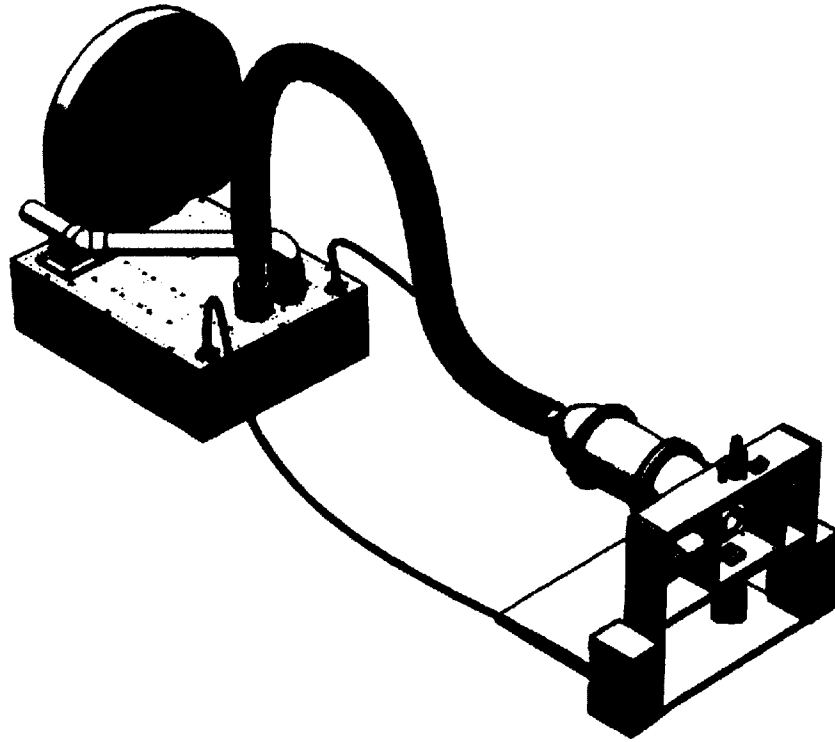
Figure 3-11. Hot-wire calibration unit which was designed and built at the University of New Hampshire specifically for calibration of multi-wire hot-wire sensors. The jet nozzle can be articulated $+/-30°$ in any direction with a fan controlled outlet velocity up to 15 m/s which is accurate to .01 m/s.

Table 3.4 provides details on the experiments performed during the single wake characterization. A total of 21 experiments were run, varying measurement technique, rotor loading conditions, and measurement field. The use of proven measurement techniques combined with the scale of the UNH Flow Physics Facility enables high fidelity wake measurements, and characterization of the axisymmetric turbulent wake with rotation.

Table 3.4. Experiments performed during single wind turbine wake characterization

Location	Tip-Speed Ratio	Measurement Device	Measurement Field
1D	2.8	Pitot-static tube	0.79 m x 0.79 m grid
2D	2.8	Pitot-static tube	0.79 m x 0.79 m grid
4D	2.8	Pitot-static tube	0.79 m x 0.79 m grid
6D	2.8	Pitot-static tube	0.79 m x 0.79 m grid
10D	2.8	Pitot-static tube	0.79 m x 0.79 m grid
14D	2.8	Pitot-static tube	0.79 m x 0.79 m grid
20D	2.8	Pitot-static tube	0.79 m x 0.79 m grid
1D	2.0	Hot-wire Anemometry	1.25 m
2D	2.0	Hot-wire Anemometry	1.25 m
4D	2.0	Hot-wire Anemometry	1.25 m
6D	2.0	Hot-wire Anemometry	1.25 m
10D	2.0	Hot-wire Anemometry	1.25 m
15D	2.0	Hot-wire Anemometry	1.55 m
20D	2.0	Hot-wire Anemometry	1.65 m
1D	2.5	Hot-wire Anemometry	1.25 m
2D	2.5	Hot-wire Anemometry	1.25 m
4D	2.5	Hot-wire Anemometry	1.25 m
6D	2.5	Hot-wire Anemometry	1.25 m
10D	2.5	Hot-wire Anemometry	1.25 m
15D	2.5	Hot-wire Anemometry	1.55 m
20D	2.5	Hot-wire Anemometry	1.65 m

CHAPTER 4

RESULTS

Velocity measurements were performed in the wake of the model wind turbine at 1, 2, 4, 6, 10, 15 (14 for pitot tube), and 20 diameters downstream of the rotor plane. Pitot-tube measurements were performed with the rotor operating in an unloaded condition, which yielded a tip-speed ratio of 2.8. Hot-wire measurements were performed with the test device operating at tip-speed ratios of 2.0 and 2.5. These two tip-speed ratios correspond to power coefficients ($C_p = \frac{P}{\frac{1}{2}\rho A V^3}$) for the wind turbine of 9.5% and 6.3%, respectively. The power coefficient, C_p, is a measure of turbine efficiency, comparing the amount of power extracted by the device to the amount of power available in the free stream (based on rotor swept area). Note that the C_p given here is a combined efficiency for rotor and power take-off (generator). Power coefficients were kept relatively low on purpose in order to maximize turbine rotation rate, leading to a comparatively "lightly loaded" rotor. Table 4.2 summarizes the performance of the test device during experiments. All experiments were performed with a tunnel free stream velocity of nominally 7 m/s. Small variations in tunnel free stream velocity were present in these experiments due to density changes, which affect the overall test section velocity. Rather than continuous adjustments to maintain a constant velocity, the tunnel fans were run at a constant RPM which is controlled by the variable frequency drives (VFD's). During processing, each experimental dataset is scaled against its own free-stream velocity eliminating the effects of small variations in inlet velocity and allowing for comparison between experiments.

Table 4.1. Rutland 910 Windcharger performance during experiments in the UNH Flow Physics Facility.

	$\lambda = 2.0$	$\lambda = 2.5$
Test Section Velocity	7 m/s	7 m/s
Load Bank Resistance	55 Ω	160 Ω
Generator Current Output	0.48 A	0.23 A
Measured Turbine Power	12.7 W	8.46 W
Available Power	133.85 W	133.85 W
Coefficient of Performancs	.095	.063

Table 4.2. Comparison of free-stream velocity measurements for each experiment using a Pitot-static tube and hot-wire anemometry. The free-stream velocities obtained by the hot-wire and Pitot-tube are large for certain experiments. This may be due to the measurement sensors being placed in different locations ($\sim$0.25 m apart when both sensors are located in the free stream.

Date	x/D	TSR	$T_{start}(^{o}C)$	$T_{end}(^{o}C)$	$U_{inf,HW}(m/s)$	$U_{inf,Pitot}(m/s)$
28FEB13	1	2.5	6.5	6.7	6.75	6.83
28FEB13	1	2.0	6.8	6.1	6.67	6.85
02MAR13	2	2.5	3.0	5.8	6.90	6.94
02MAR13	2	2.0	6.8	6.9	6.72	6.85
02MAR13	4	2.5	6.9	3.8	7.04	6.89
02MAR13	4	2.0	3.8	2.8	6.83	7.02
04MAR13	6	2.5	-1.3	2.7	6.84	7.09
09MAR13	15	2.5	7.9	5.2	7.08	7.17
10MAR13	20	2.5	4.2	5.2	7.01	7.07
10MAR13	20	2.0	5.2	4.4	7.01	7.13
11MAR13	10	2.5	5.9	10.6	7.13	6.90
11MAR13	15	2.0	10.6	8.9	7.01	7.20
11MAR13	6	2.0	8.6	6.9	6.89	7.10
25MAR13	10	2.0	7.2	5.8	7.11	6.97
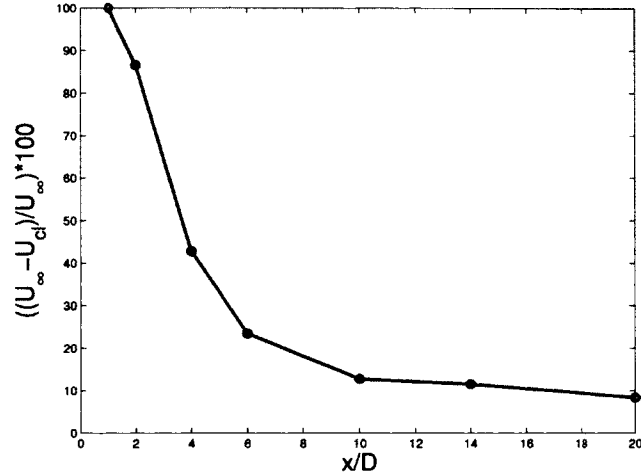
Figure 4-1. Downstream evolution of the mean centerline velocity deficit. U_{cl} is the velocity at the centerline and D is the rotor diameter.

4.1 Pitot-Static Tube

Despite the previously mentioned limitations of the Pitot-static tube with respect to measuring turbulent fluctuations, it produced valuable information regarding mean velocity deficit in the wake of the model wind turbine. The mean velocity deficit at the centerline is shown as a percentage of the free stream in Figure 4-1. At 6 diameters downstream a wake recovery of about 79% (21% deficit) is found and at 20 diameters a wake recovery of about 92% (8% deficit) is found.

A full "quarter wake map" was measured at positions $x/D = 1, 2, 4, 6, 10, 14$, and 20, and is shown in Figure 4-2. Flow is from left to right, and the model turbine is positioned 1 diameter in front of the slice furthest to the left at x/D=0. Sampling points were evenly spaced at 2.54 cm (1 inch) and extend 0.79 m (31 inches) in both the horizontal and vertical directions. The profiles overlapped the centerline of the rotor by 2.54 cm (1 inch) in both directions. As expected, wake growth is comparatively small due to the low rotor thrust coefficient. Figure 4-2 provides a good visual of the velocity deficit at all radial positions at various downstream locations. Quantitative

38

information presented in Figures 4-1, 4-3, and 4-4 was obtained by averaging the data points in the vertical and horizontal directions from the wake center.
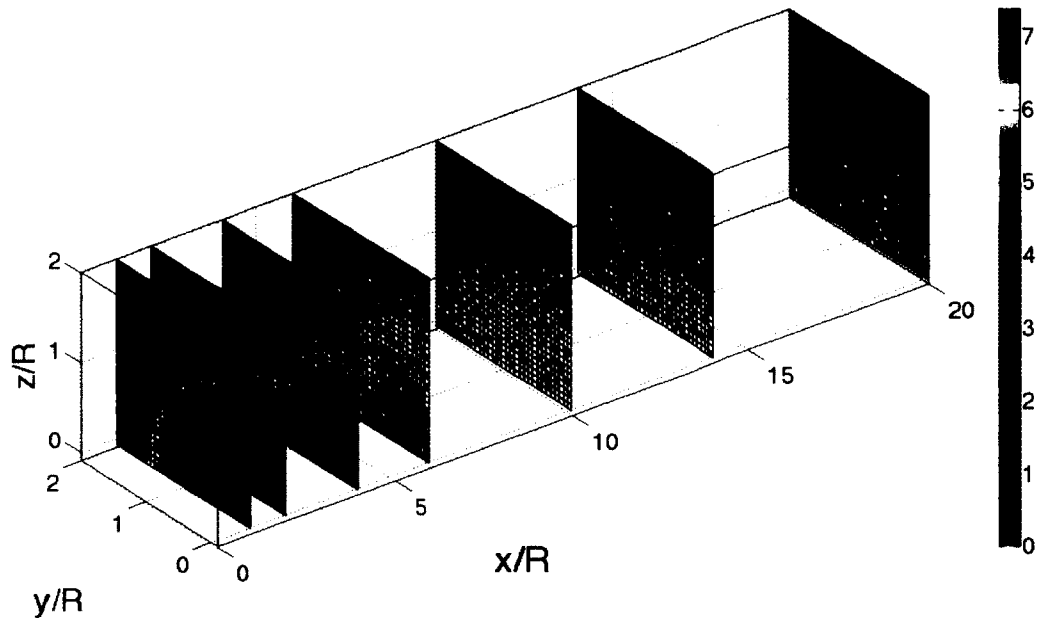
Figure 4-2. Quarter-wake map at multiple locations downstream of the rotor. Flow was from left to right with the turbine placed one rotor diameter upstream (to the left) of the first slice. R represents the turbine radius.

Figure 4-3 shows the mean velocity at several downstream locations normalized with the free stream velocity. Important to note from Figure 4-3 is the fact that the Pitot-static tube does not appear to fully reach the free stream at some of the farther downstream locations. This was a limitation of the traversing system used during data acquisition for the Pitot-tube measurement (30 inch / 0.75 meter travel). There also does not appear to be significant wake growth, which is expected due to the low rotor thrust coefficient used. Recall that a low thrust coefficient was used in attempt to maximize the blade tip-speed ratio, to better simulate the flow characteristics of a full scale turbine.
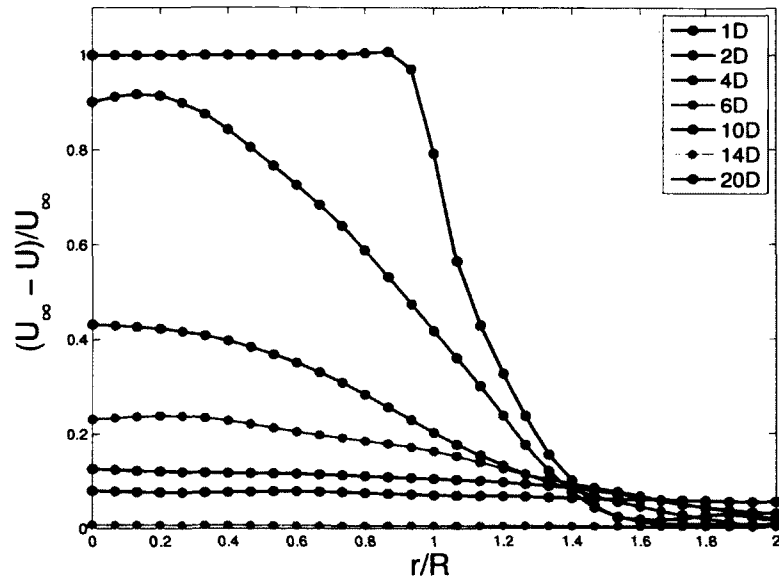
Figure 4-3. Mean velocity profiles at multiple locations downstream of lightly loaded rotor operating at tip-speed ratio $\simeq$ 2.8 (scaled to free stream velocity). R represents the turbine radius and r is the radial position.
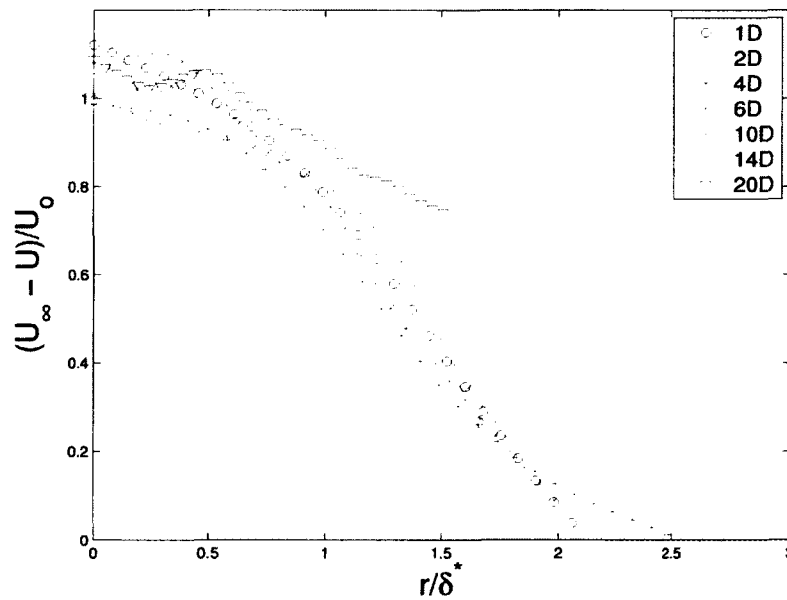
Figure 4-4. Similarity solution of the mean velocity profiles at multiple locations downstream of lightly loaded rotor operating at tip-speed ratio $\simeq$ 2.8 ($U_o = U_\infty - U_{cl}$).

Figure 4-4 shows the same data in the similarity variable derived previously, where the mean velocity is normalized with the centerline velocity deficit ($U_o = U_\infty - U_{cl}$) and the radial position is normalized with the displacement radius, δ^* ($\delta^* = \lim_{r \to \infty} \frac{1}{U_o} \int_0^r (U_\infty - U) r dr$). The profiles do appear to collapse onto one another as seen in other axisymmetric wake experiments such as Johansson 2002 [20], however, the data collapse is not very good due to the Pitot-tube not reaching the free stream for the further downstream locations. Scaling the data with an integral length scale such as δ_* makes it more noticeable in Figure 4-4 than in Figure 4-3 that the traversing system did not quite reach the free stream, especially at the 14 and 20 diameter locations. An upgrade was made to the traversing system for the hot-wire measurements to increase travel to 1.25 m.

4.2 Hot-Wire Anemometry

Velocity measurements were performed at $x/D = 1, 2, 4, 6, 10, 15,$ and 20, using an X-wire hot-wire sensor. A sampling rate of 10 kHz was used with a sample time of 60 seconds per point. The probe was traversed horizontally (with respect to the test section floor) from the center of the turbine out. The traversing spacing was decreased to 1 cm (2.54 cm for the Pitot-tube experiments) in order to improve spatial resolution of the high gradients that are present within the wake flow. Sampling time and point spacing was chosen in order to maximize data collection and traversing length within a 2.5 hour time span. 2.5 hours was used as a maximum experiment time in order to limit thermal drift of the hot-wire sensor. A full wake map was not reasonable with these sample times, however it is not necessary since the wake was proven to be axisymmetric with the Pitot-tube measurements. A 1-dimensional profile provides the same quantitative information.

4.2.1 Data Analysis

Multi-wire hot-wire data is analyzed using voltages that were obtained during calibrations prior to and immediately following experiments. The calibrations were done with known velocities, which were then compared to the output voltages to create an interpolation table covering a range of anemometer output voltages. These calibrations were designed to cover all ranges of resultant vector magnitudes and directions that may be encountered during experimentation. As mentioned previously, calibration was run at speeds up to 10 m/s and inflow angles up to $+/-30°$. Therefore the assumption was made that the resultant velocity vector that forms from the two dominant flow directions will not exceed 30° from the zero angle of the probe. In other words, the most dominant flow direction was assumed to be more than double the magnitude of the secondary flow direction, which is a reasonable assumption for a weakly swirling axisymmetric flow. This yields a resultant velocity vector that is less than 30° off the angle of the probe orientation. It is shown later than the magnitude of the azimuthal velocity is an order of magnitude less than the streamwise velocity.

The individual hot-wire voltages that are obtained during calibration are interpolated using a grid fit method. From this, a table is made for each wire that contains a series of interpolations that are representative of inflow speed and angle. The hot-wire voltages obtained during the experiments are then compared to these interpolation tables to determine the corresponding magnitude and direction of the resultant flow. It is important to note that due to wire orientation, a single wire may have the same cooling rate for different inflow conditions (speed and direction). This is why multi-wire sensors are required to resolve multiple components of flow. During data analysis, interpolation tables for both wires are referenced in conjunction to determine the resultant inflow vector. Using this information, the magnitude of the flow in the two dominant directions can be determined.

After initial processing of the X-wire data, the following problems needed to be addressed: (1) Although the azimuthal velocity always approached a constant value in the free stream for each profile, for some profiles this value was non-zero. The absolute value for azimuthal mean velocity was discovered to be highly sensitive towards small variations in calibration flow angles, whereas the absolute value of stream-wise mean velocity was rather insensitive towards small variations in calibration flow angles. This is due to the magnitude of the azimuthal velocities being an order of magnitude smaller than the stream-wise velocities. (2) The ambient temperature often changed sufficiently during the course of each profile to result in significantly different calibrations before and after each profile. The average temperature change during experiments was observed to be approximately 2°C with a maximum (worst case) of 4.7°C. This added a slight shift to each data set when compared to itself with both calibrations. However, the data themselves exhibited the expected trends when compared to previously obtained axisymmetric wake data and were deemed valid. Ambient temperature changes are expected due to the open return design and lack of thermal control in phase 1 of the UNH FPF. The source of flow angle variation was believed to originate in the set-up of the calibration jet. The following corrective measures were taken in the re-processing of the X-wire data:

- Calibration angles were adjusted to force the mean azimuthal velocity in the free stream to be zero. The angular adjustments that were made for each profile can be seen in Table 4.3. The effect of an angle change on azimuthal velocity can be seen in Figure 4-5. It was confirmed in facility qualification measurements that no mean swirl exists in the free stream [49] . General trends in the data were unaffected by this adjustment.

- The ambient temperature variation with time during each profile was incorporated in post-processing. Based on the calibrations before and after each profile, a linearly interpolated calibration was applied to each data point if temperature

variation was linear. The difference can be seen in Figure 4-6. If a non-linear
ambient temperature variation occurred, piecewise linear interpolation was ap-
plied.
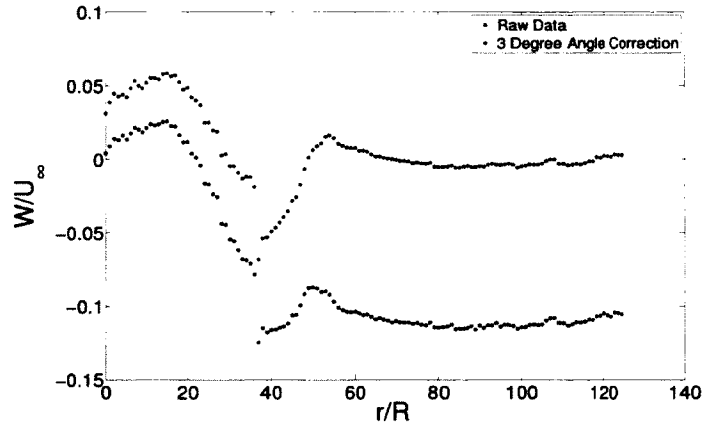
Figure 4-5. Effect of adjustment to the calibration angle for the same profile $(x/D =$
1 TSR=2.0). Small angle changes have a significant effect on the azimuthal velocity
due to the smaller magnitude when compared to the streamwise velocity.
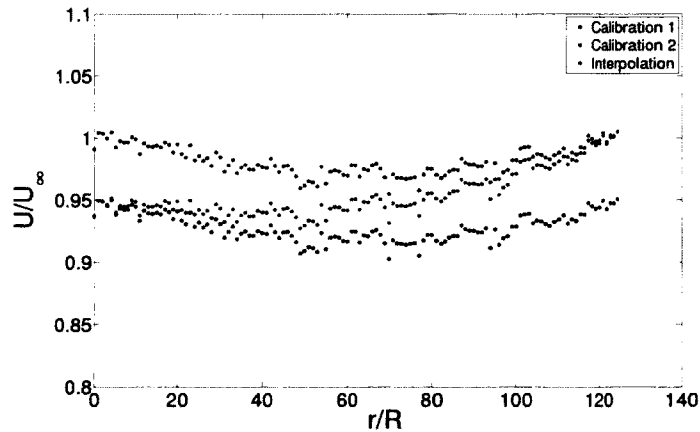
Figure 4-6. Variations in velocity measurements based on voltage comparisons be-
tween calibration 1 and calibration 2. There is significant thermal drift over 2.5 hours
between calibrations. The interpolation between the two calibrations produces the
correct wake profile. Profile location is $x/D = 20$ with TSR=2.0

Table 4.3. Angle adjustments that were applied to each profile in order to force the mean azimuthal velocity to zero in the free stream (which was verified in measurements by Vincenti et al. 2012 [49])

Tip-Speed Ratio	Downstream Location	Calibration 1	Calibration 2
2.0	1D	$+3^o$	$+2^o$
2.0	2D	$+2.25^o$	$+1.5^o$
2.0	4D	$+2^o$	$+3.5^o$
2.0	6D	$+1.75^o$	$+2.25^o$
2.0	10D	$+2^o$	$+1.5^o$
2.0	15D	$+2.5^o$	$+2.25^o$
2.0	20D	$+2^o$	$+1^o$
2.5	1D	$+1.5^o$	$+2.75^o$
2.5	2D	-0.5^o	$+2.25^o$
2.5	4D	-1°	$+2^o$
2.5	6D	$+3.75^o$	$+1.75^o$
2.5	10D	$+2.25^o$	$+2.25^o$
2.5	15D	$+3^o$	$+2.25^o$
2.5	20D	$+1^o$	$+1.5^o$

4.2.2 Wake Data

Mean stream-wise velocity data is shown in Figure 4-7. The stream-wise profiles are similar to the Pitot-static tube measurements, with the exception of the area directly behind the turbine in the near wake, where the Pitot-static tube measurements were saturated. In all referenced figures, the blade tips extend to a radial position of approximately 45.5 cm. There do not appear to be any major differences between the two operating conditions with the exception of the near wake region. The higher tip-speed ratio has a steeper gradient near the blade tips, and appears to accelerate the flow just outside the wind turbine rotor. The $x/D = 1$ and $x/D = 2$ profiles appear to have a greater velocity deficit with $\lambda = 2.5$. They also show a more defined peak in velocity prior to reaching the free stream. In other words, the higher tip-speed ratio case appears more "solid" to the flow.

Azimuthal velocity profiles for each downstream location are shown in Figure 4-8. Figure 4-8 is a dimensional plot showing the magnitude of swirl vs radial position.

Multiple peaks are present in downstream locations at $x/D = 1, 2$, and 4. The outer peaks in azimuthal velocity are due to tip vortices which are shed from the blade tips. These tip vortices break down quicker than the mean swirl which is still present up to $x/D = 20$ and peaks at a downstream location of $x/D = 6$. A strong hub vortex can also be seen at the lower radial positions in the near wake. Mean swirl is induced as the oncoming flow is deflected by the rotor blades and rotates opposite of the rotor. Positive azimuthal velocity indicates swirl in the opposite direction of the rotor. It is clear that more swirl and a stronger blade tip vortex is induced when the rotor is operating at $\lambda = 2.0$. This concurs with previous expectations due to the increase in power extraction, and the resulting higher loading of the turbine blades. Mean azimuthal velocity is an order of magnitude smaller than mean stream-wise velocity. This confirms our assumption made prior to calibration that the dominant direction of flow would be more than double that of secondary flow direction. Note that the mean swirl should cross zero at $r = 0$. This can easily be obstructed by having a slightly off centerline position for $r = 0$, i.e. a very slight misalignment of the wake flow.

George 1994 determined that a high Reynolds number similarity solution for free shear flows only applies if a clear inertial subrange appears in the power spectrum. This is evident for local Reynolds numbers ($Re_{\delta^*} = \frac{U_o \delta^*}{\nu}$) greater than 1600. When $Re = 400$ the existence of the inertial subrange becomes questionable and by $Re = 200$ it no longer exists. [18] [21]. It is clear from Figure 4-9 that the infinite Reynolds number assumption is valid in these experiments. It is also shown in Figure 4-10 that sample spectra taken at multiple radial locations appear to follow a $-5/3$ slope showing the existence of at least a decade and a half of inertial subrange. Along with this, it must be shown that the turbulence intensity ratios (u'/U_o and w'/U_o) reach a constant value in order for the similarity theory to be valid. This is difficult to conclude due to the fact that these experiments only span downstream distances
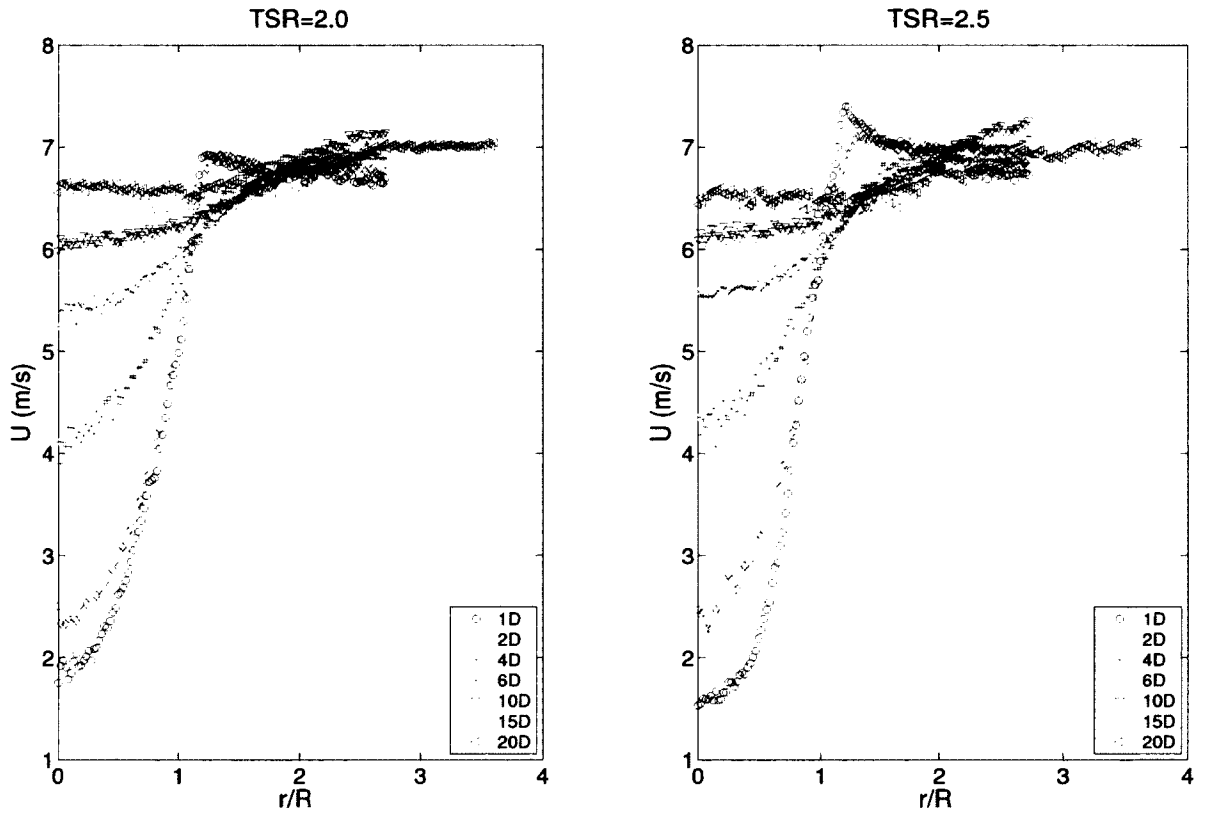
Figure 4-7. Mean streamwise velocity in the wake of the model wind turbine obtained using an X-wire hot-wire sensor. R represents the turbine radius of 0.455m and r is the radial position.
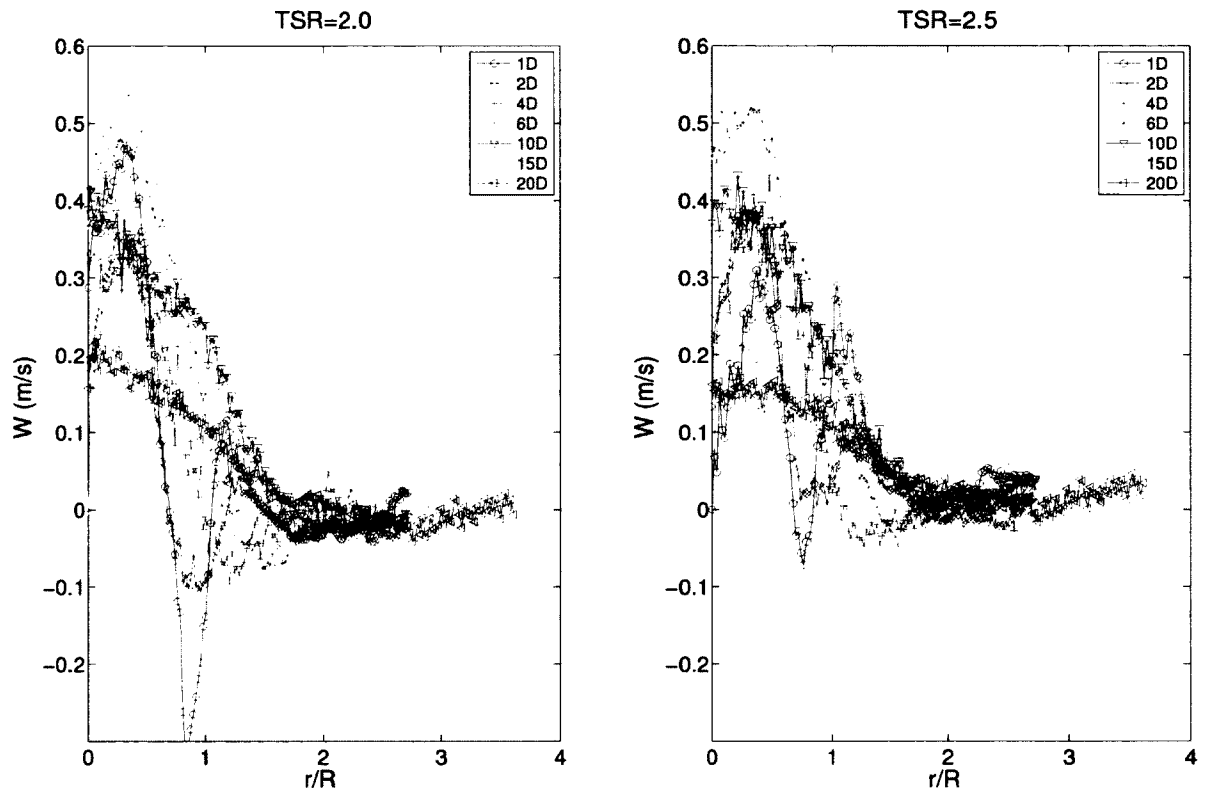
Figure 4-8. Mean azimuthal velocity in the wake of the model wind turbine obtained using an X-wire hot-wire sensor. R represents the turbine radius of 0.455m and r is the radial position.

which are comparable to the beginning of the traditional 'far wake' region. These turbulence intensity ratios are presented in Figure 4-11 and Figure 4-12 and do appear to be trending toward a constant value.
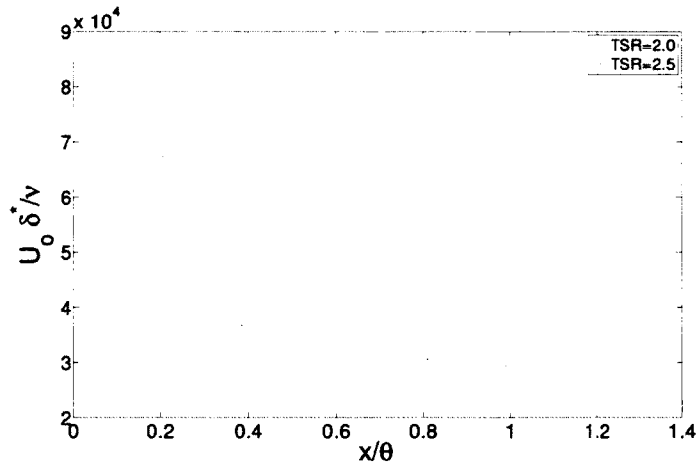
Figure 4-9. Local Reynolds number ($Re_{\delta^*} = \frac{U_o \delta^*}{\nu}$) for each downstream location. θ is the momentum thickness.

Figure 4-13 shows the mean stream-wise velocity profiles normalized by the free-stream velocity. This gives a visual representation of mean velocity deficit in the wake of the rotor. Again, the higher tip-speed ratio appears to show a larger velocity deficit, but only in the near wake. Figure 4-14 shows the same data normalized by the velocity difference between free stream and centerline (U_o) vs. δ^* , the scaling parameters derived from the similarity solution in Chapter 2. The profiles do appear to collapse onto one another as observed in other axisymmetric wake experiments (e.g. Johansson 2002), confirming that the wake quickly evolves to self-similar profiles for the mean streamwise velocity deficit. This similarity scaling shows more scatter at the downstream locations, but this is a result of a significantly smaller centerline velocity deficit, which emphasizes small variations when scaled with this parameter. Due to the sensitivity imposed by small variations in the centerline velocity deficit, rather than use the streamwise velocity at $r = 1$, an average of the streamwise velocity at

49
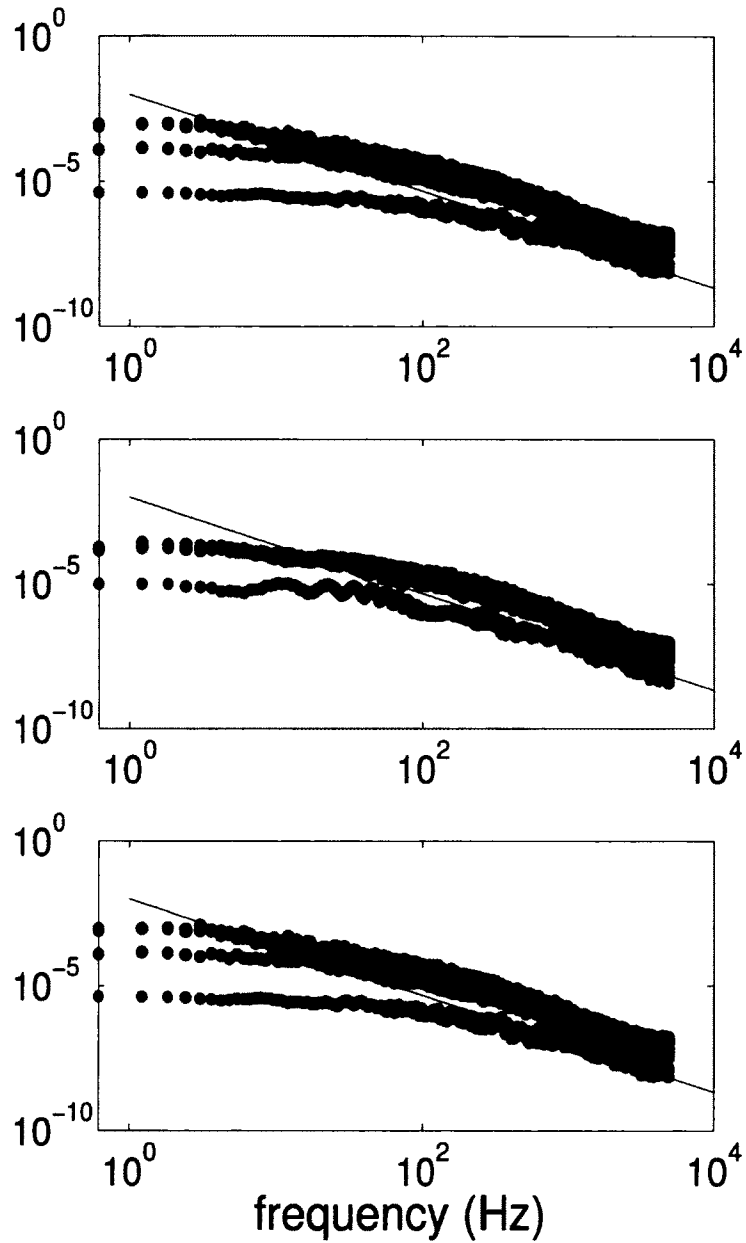
Figure 4-10. Sample streamwise spectra at TSR=2.0. Radial locations of $r = 1$ cm (top), $r = 23$ cm (middle), and $r = 46$ cm (bottom) are presented Comparisons at the $x/D = 1$to 6 follows a $-5/3$ slope which shows the existence of an inertial subrange. $x/D = 1$ is shown in blue, $x/D = 2$ is shown in green, $x/D = 4$ is shown in red, and $x/D = 6$ is shown in aqua.
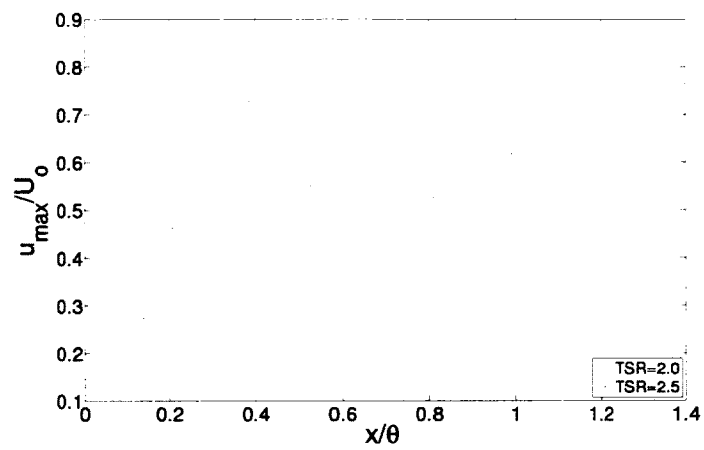
Figure 4-11. Maximum streamwise velocity fluctuations at each downstream location.
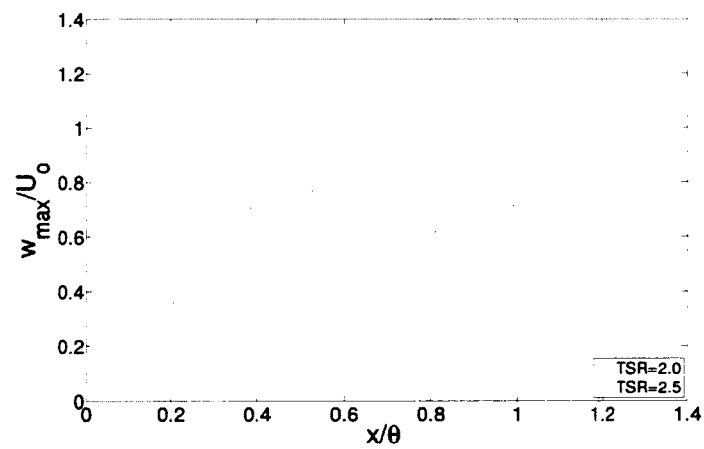
Figure 4-12. Maximum azimuthal velocity fluctuations at each downstream location.

$r = 1$ to $r = 5$ was used to obtain a representation of the velocity deficit that was unaffected by scatter in the data.

Figure 4-15 shows the mean azimuthal velocity normalized by $U_o^{\frac{3}{2}}$ (centerline velocity deficit), the scaling predicted by the condition for a similarity solution in equation 2.24 (since $U_o^{\frac{3}{2}} \sim x^{-1}$). Due to the presence of tip vortices, the near wake profiles do not collapse. The azimuthal flow in the wind turbine wake is complicated: tip vortices break down, mean swirl is induced at the rotor and a hub vortex forms and decays until, further downstream, a self-similar rotating wake emerges. The $x/D = 15$ and $x/D = 20$ profiles appear to collapse with the similarity scaling parameter $U_o^{\frac{3}{2}} \sim x^{-1}$ for $\lambda = 2.0$. With $\lambda = 2.5$, the four furthest downstream profiles ($x/D = 6$ to 20) all appear to reach a self-similar state. Due to the magnitude of the azimuthal velocity being an order of magnitude lower than the stream-wise velocity, this similarity scaling is highly sensitive to the centerline velocity deficit. The far wake does appear to conform to these similarity profiles, but more experiments will be needed at further downstream locations to confirm that mean swirl has truly become self-similar.

Figure 4-16 and Figure 4-18 show the fluctuating component of velocity in both the stream-wise and azimuthal directions, respectively. Free stream velocity fluctuations are extremely small, which is an important verification that both the facility and the measurement techniques are performing as expected. The velocity fluctuations in the turbulent wake are an order of magnitude less than the free stream (convection) velocity and are of the same order as the mean azimuthal velocity. This is important, because it means that azimuthal velocity fluctuations are on the same order as the azimuthal mean velocities. In most cases, turbulence intensities greater than 100% exist in the azimuthal direction. In the $x/D = 10, 15,$ and 20 profiles, the fluctuations do not appear to reach a free stream value at the outer radial positions. This is an indication that although the mean velocities have reached free stream values at
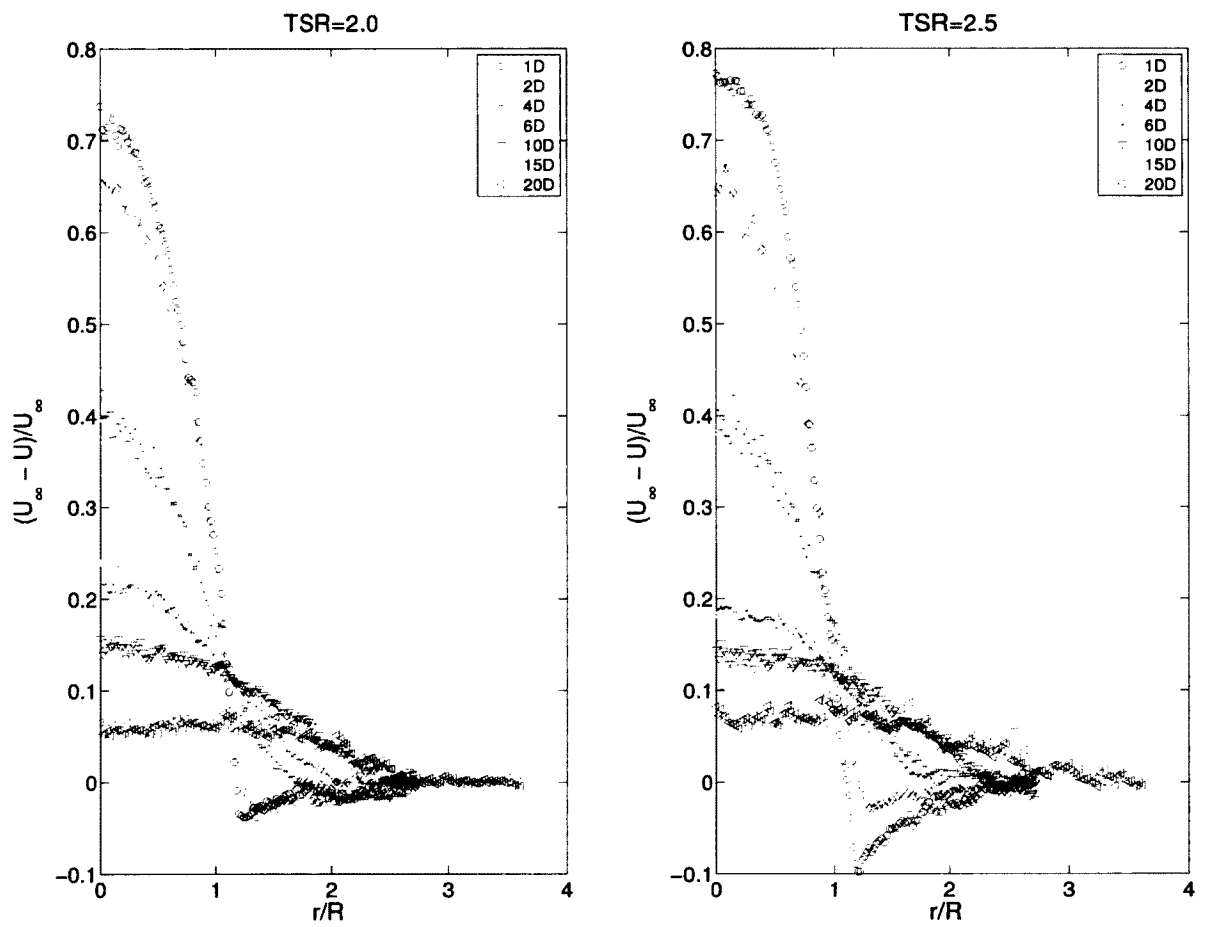
Figure 4-13. Streamwise velocity normalized by the free stream velocity (U_∞). R represents the turbine radius and r is the radial position.
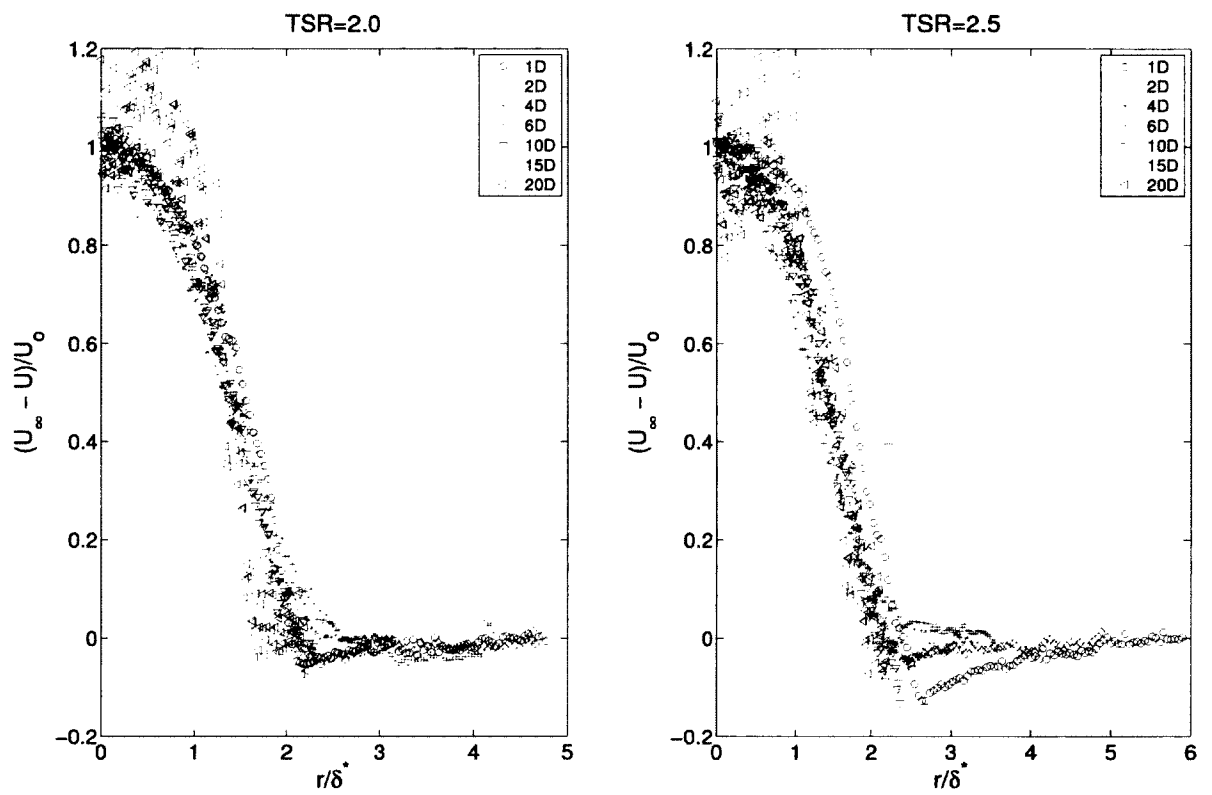
Figure 4-14. Streamwise velocity normalized by scaling parameters U_o and $\delta*$.
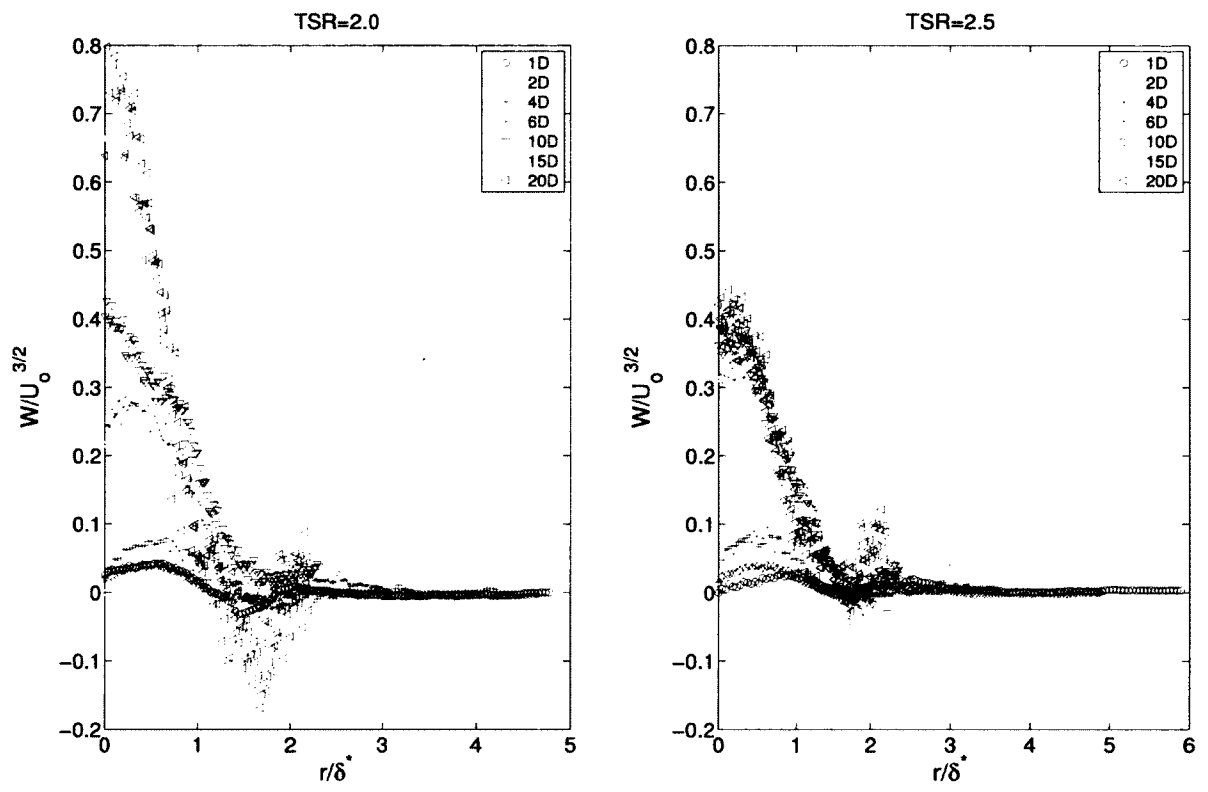
Figure 4-15. Azimuthal velocity normalized by scaling parameters U_o and $\delta*$.

these radial positions, noticeable wake effects in the turbulence remain at the furthest radial positions of these downstream profiles.

At $x/D = 1$, multiple peaks are present along the length of the blade tip in both the stream-wise and azimuthal fluctuations. Again, this is due to the vortices shed at the blade tips. These gradients appear to smooth out quickly as they are no longer present further downstream. Peak fluctuations in the stream-wise velocity occur at the radial position that coincides with the blade tips, whereas peak azimuthal velocity fluctuations migrate towards the centerline. There is very little difference between the two rotor loading conditions.

Streamwise velocity fluctuations scaled with U_o are shown in Figure 4-17. Similar to the azimuthal mean velocity, the near wake profiles do not collapse into the similarity solution yet. At the higher tip-speed ratio, the $x/D = 10, 15$, and 20 appear to begin collapsing, whereas the lower tip-speed ratio does not follow suit. This is also similar to the azimuthal mean velocity scaling, showing that an increase in power extraction appears to delay agreement with the similarity scaling until further downstream.

Azimuthal velocity fluctuations are seen in Figure 4-19. The scaling parameters have a similar affect as with the streamwise velocity fluctuations. At the higher tip-speed ratio, the $x/D = 10, 15$, and 20 appear to begin collapsing, whereas the lower tip-speed ratio does not follow suit. Reynolds shear stress (the apparent turbulent stress) is compared for the various downstream locations in Figure 4-20. Reynolds stress in the free-stream is very low as would be expected given the turbulence statistics above. The Reynolds stress is observed to decay rapidly as it seems to practically disappears at $x/D = 15$ and $x/D = 20$ (at the scale plotted here). The limited amount of swirling wake data available in literature gives little reference to the expected magnitude of the Reynolds stress, but the rate of recovery downstream is certainly of interest.
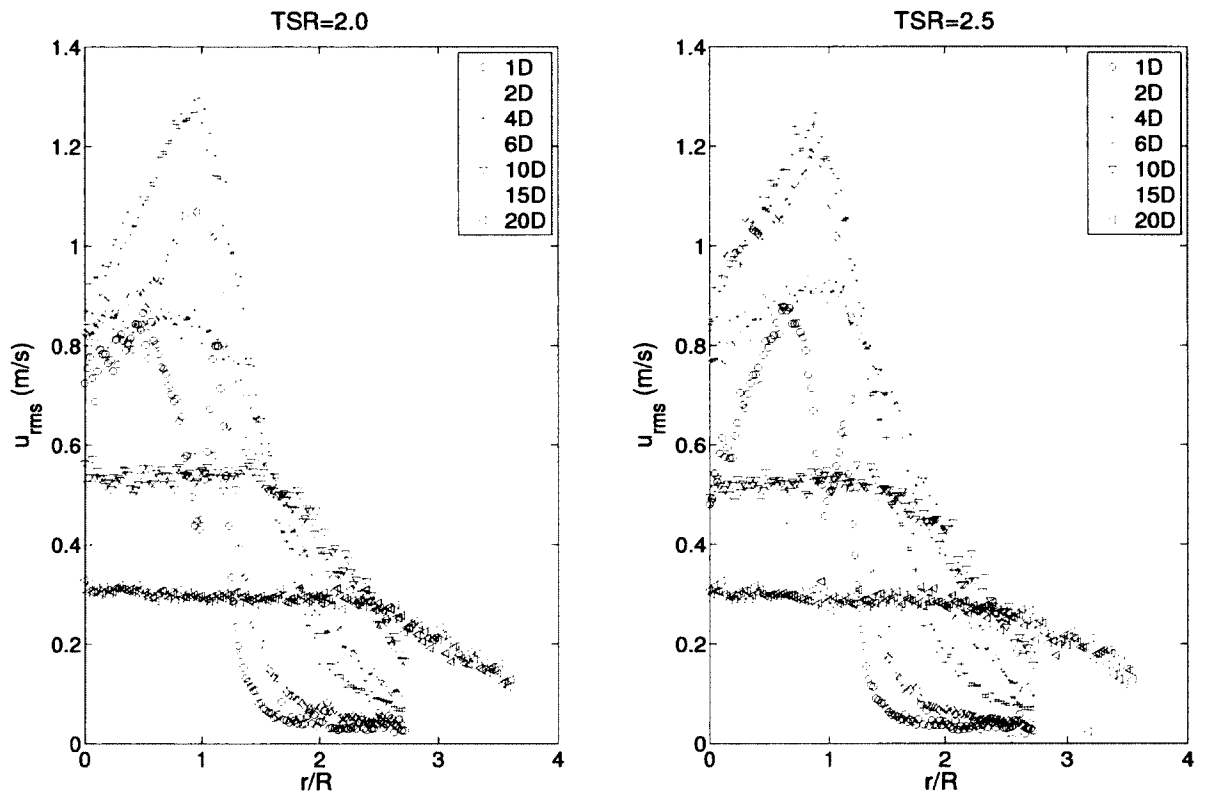
Figure 4-16. Streamwise velocity fluctuations. R represents the turbine radius and r is the radial position.
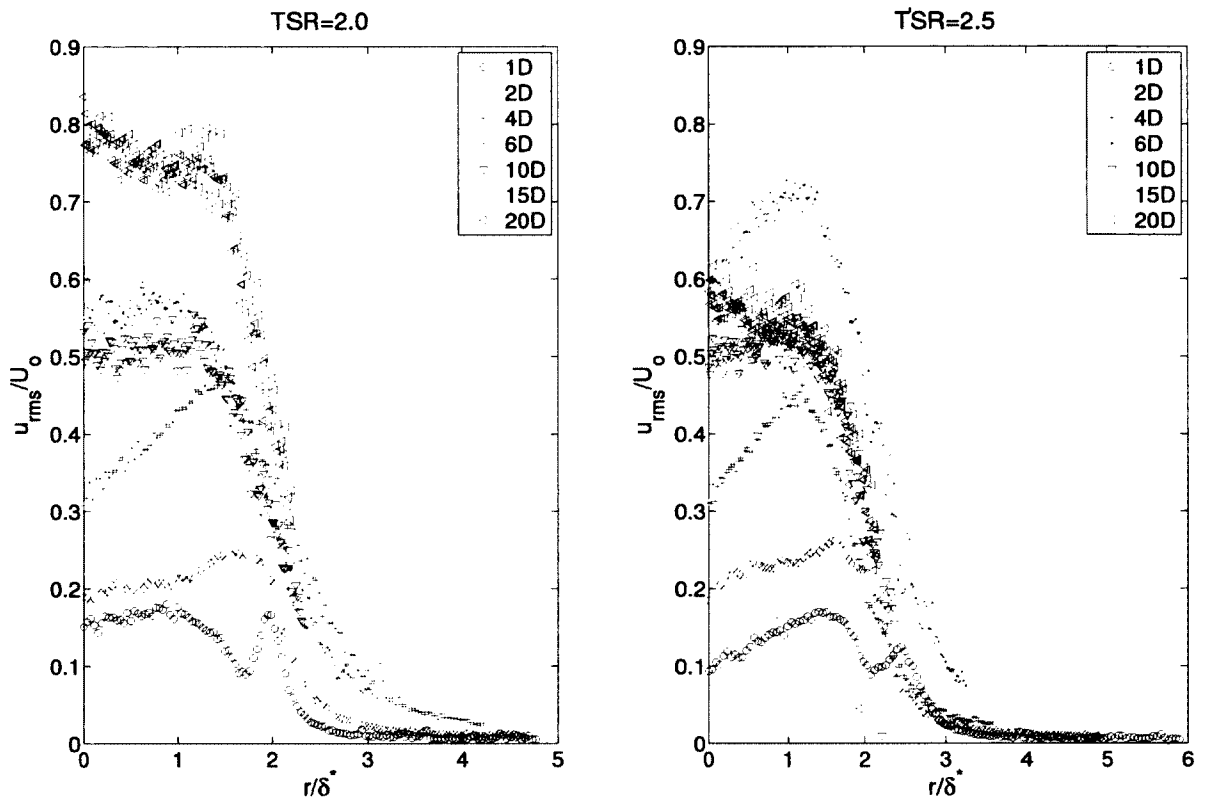
Figure 4-17. Streamwise velocity fluctuations normalized by scaling parameters U_o and $\delta*$.
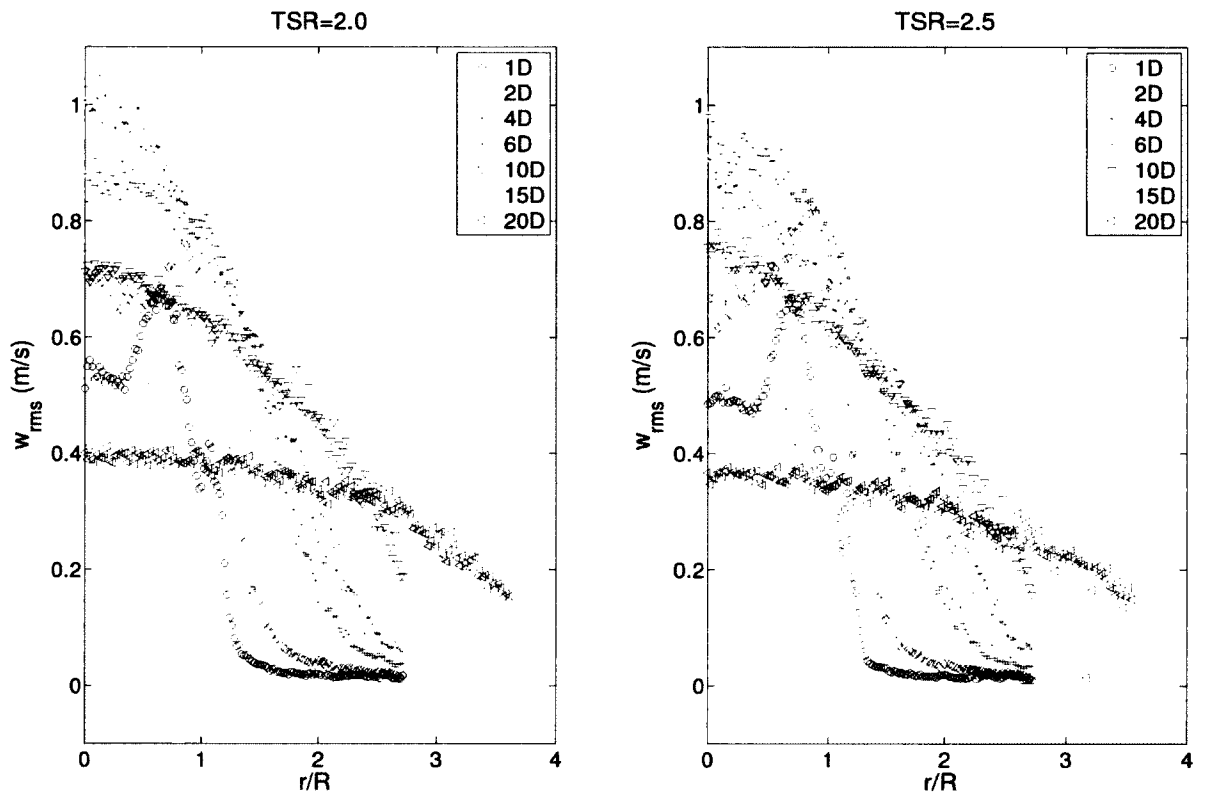
Figure 4-18. Azimuthal velocity fluctuations. R represents the turbine radius and r is the radial position.
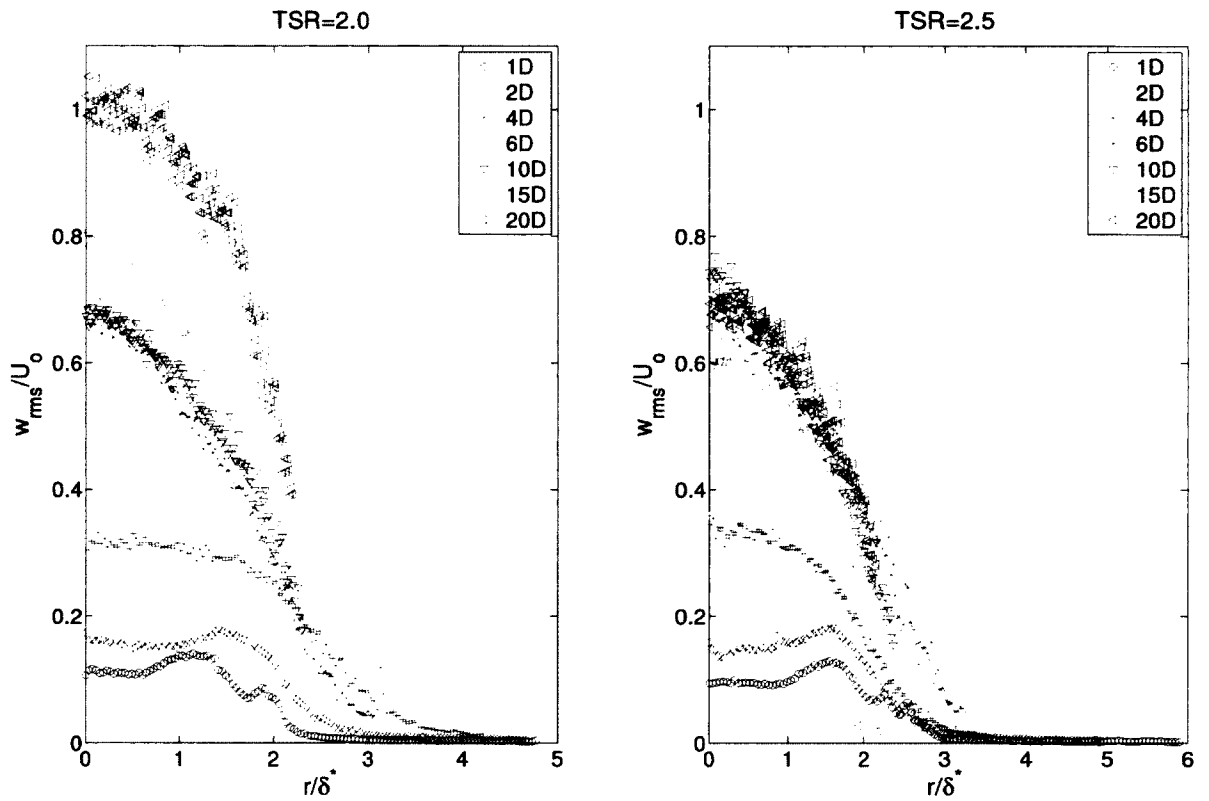
Figure 4-19. Azimuthal velocity fluctuations normalized by scaling parameters U_o and $\delta*$.
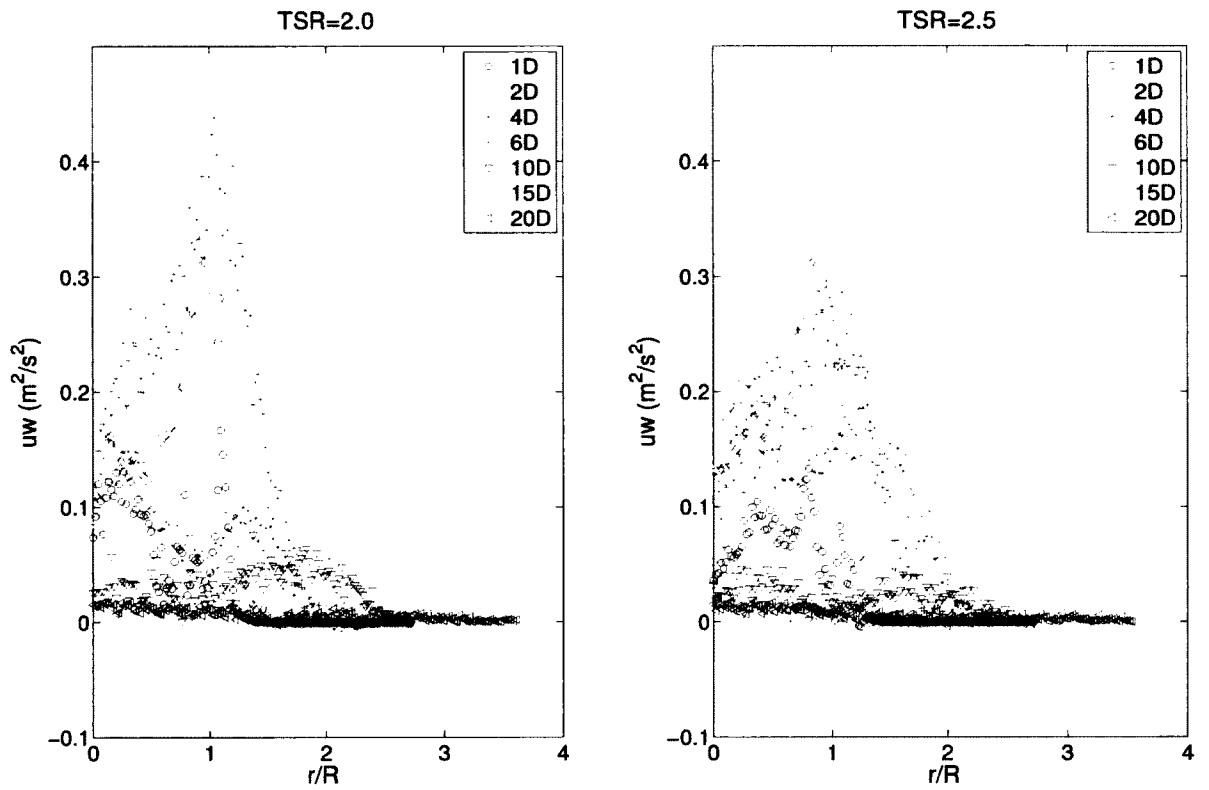
Figure 4-20. Reynolds shear stress. R represents the turbine radius and r is the radial position.

Figure 4-21 shows the evolution of the mean velocity deficit and the maximum azimuthal velocity with downstream distance from the rotor, which is another way of representing the wake recovery rate. The similarity solution for the turbulent axisymmetric wake with rotation dictates a mean velocity deficit decay rate with $x^{-2/3}$ and a decay of rotation with x^{-1} where x is downstream distance. The mean velocity deficit does appear to be converging on this decay rate, but more profiles at further downstream locations would help to confirm this.

The shedding of tip vortices and the hub vortex complicate the picture for evolution of the mean swirl in the near-wake. However, at downstream locations beginning with $x/D = 6$ (which is where the tip vortices decay) the mean swirl appears to begin to follow this x^{-1} decay rate. Again, profiles taken further downstream would help to confirm this. Future wake studies in the UNH FPF are needed to better determine the wake recovery rates of wind turbine wakes. The wake width is defined by the δ^* scaling parameter (displacement radius). This is plotted against downstream location in Figure 4-22. Wake growth rate can be seen to approximately conform to follow and $x^{1/3}$ trend. In these experiments, the wakes appear to be growing at a slightly higher rate than this estimate. This agrees with the slightly faster recovery of the centerline velocity deficit which is seen in Figure 4-21.

The decay rates presented above are derived from the infinite Reynolds number similarity solution of the reduced order equations. The infinite Reynolds number assumption sets the viscous terms of the momentum equations to zero and is required for the similarity theory to be valid. However, the similarity solution only becomes valid as the wake becomes independent of its origins. This eliminates the use of any Reynolds number associated with the wake generator in the verification of the inviscid assumption. The local Reynolds number was calculated at various downstream location using the δ^* length scale. This was presented earlier in Figure 4-9.
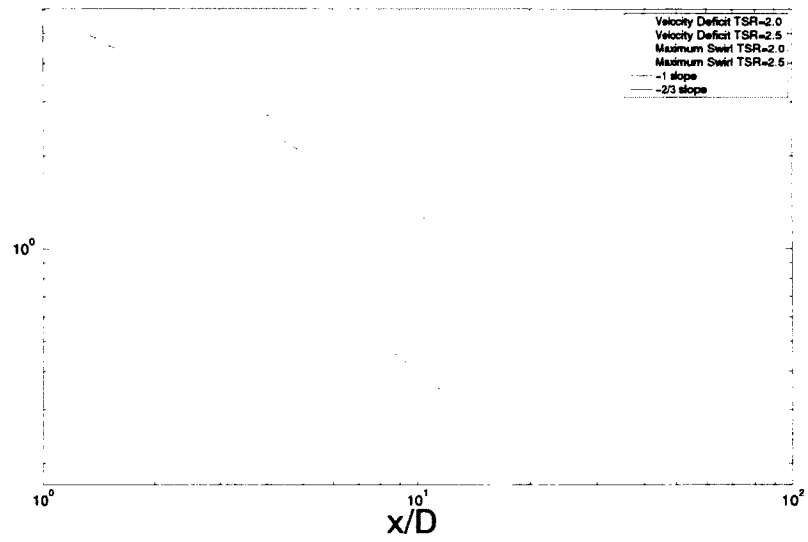
Figure 4-21. Velocity deficit and maximum swirl at each downstream location.
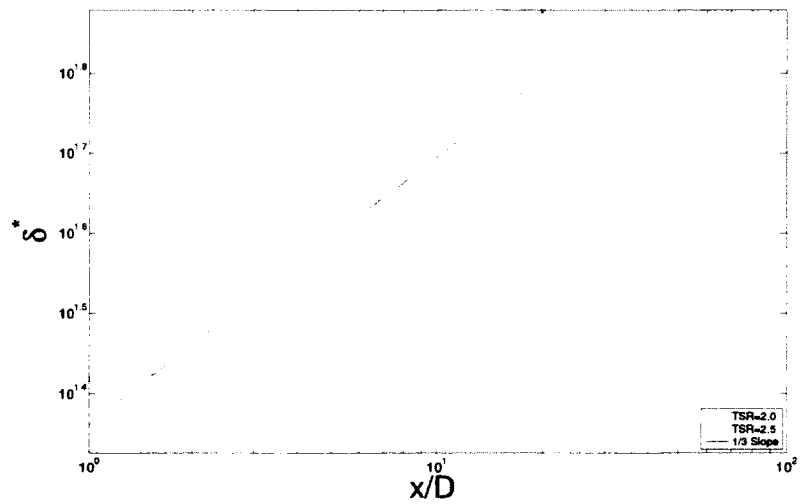
Figure 4-22. δ^* at each downstream location.
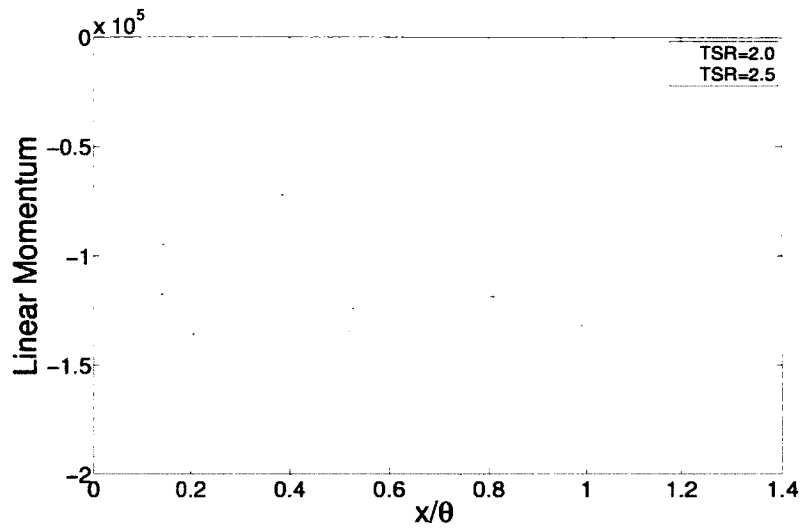
Figure 4-23. Streamwise momentum for both tip-speed ratio's at each downstream location. Momentum thickness is represented by θ. Streamwise momentum is determined using the integral presented in Chapter 2.
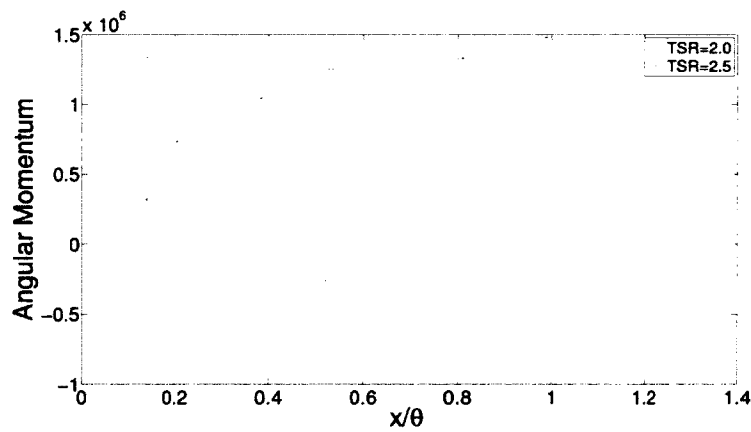
Figure 4-24. Angular momentum for both tip-speed ratio's at each downstream location. Momentum thickness is represented by θ. Angular momentum is determined using the integral presented in Chapter 2.

64
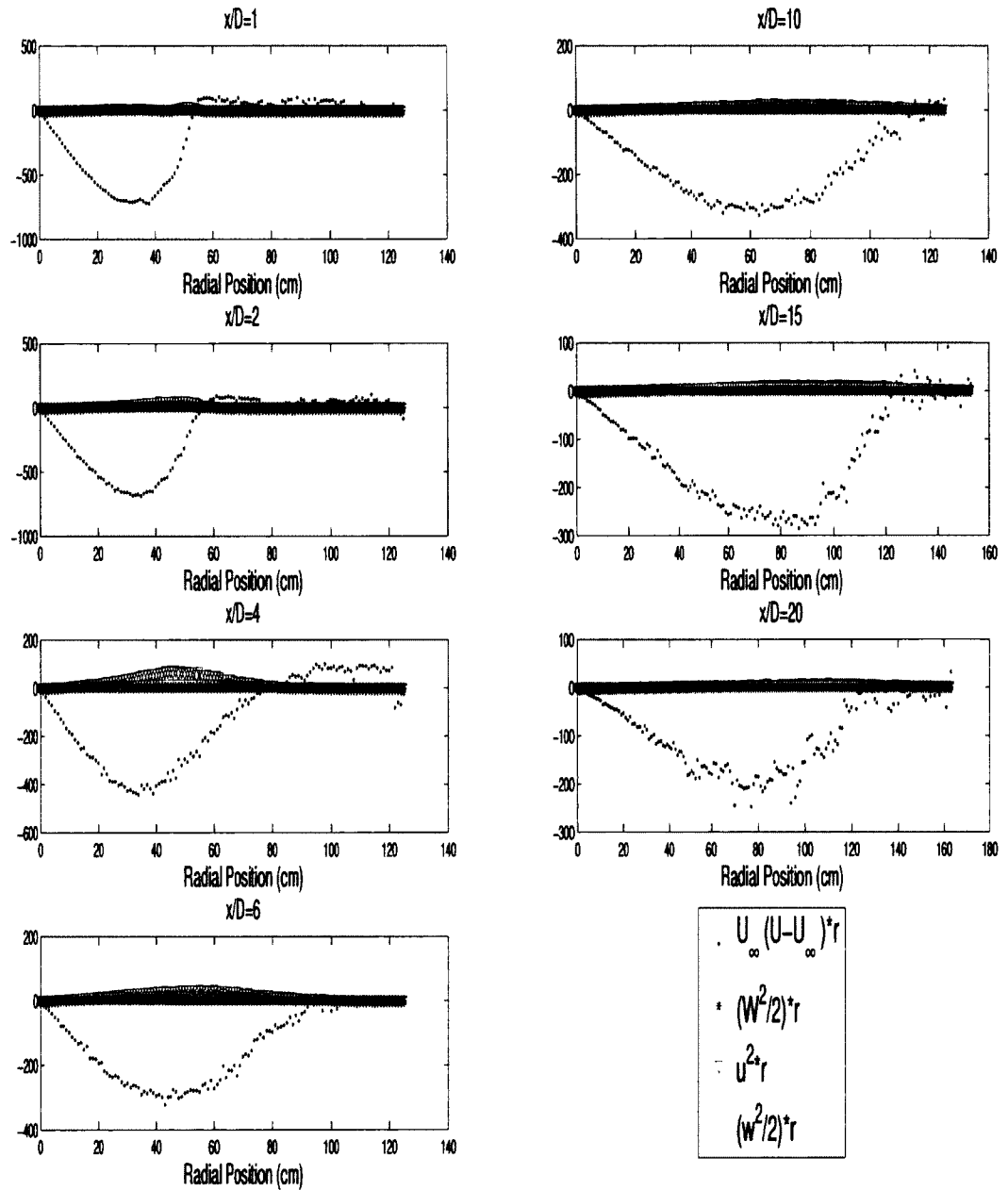
Figure 4-25. Terms of the streamwise momentum integrand plotted separately to show the impact of each term on the streamwise momentum integral plotted in Figure 4-23 (TSR=2.0)
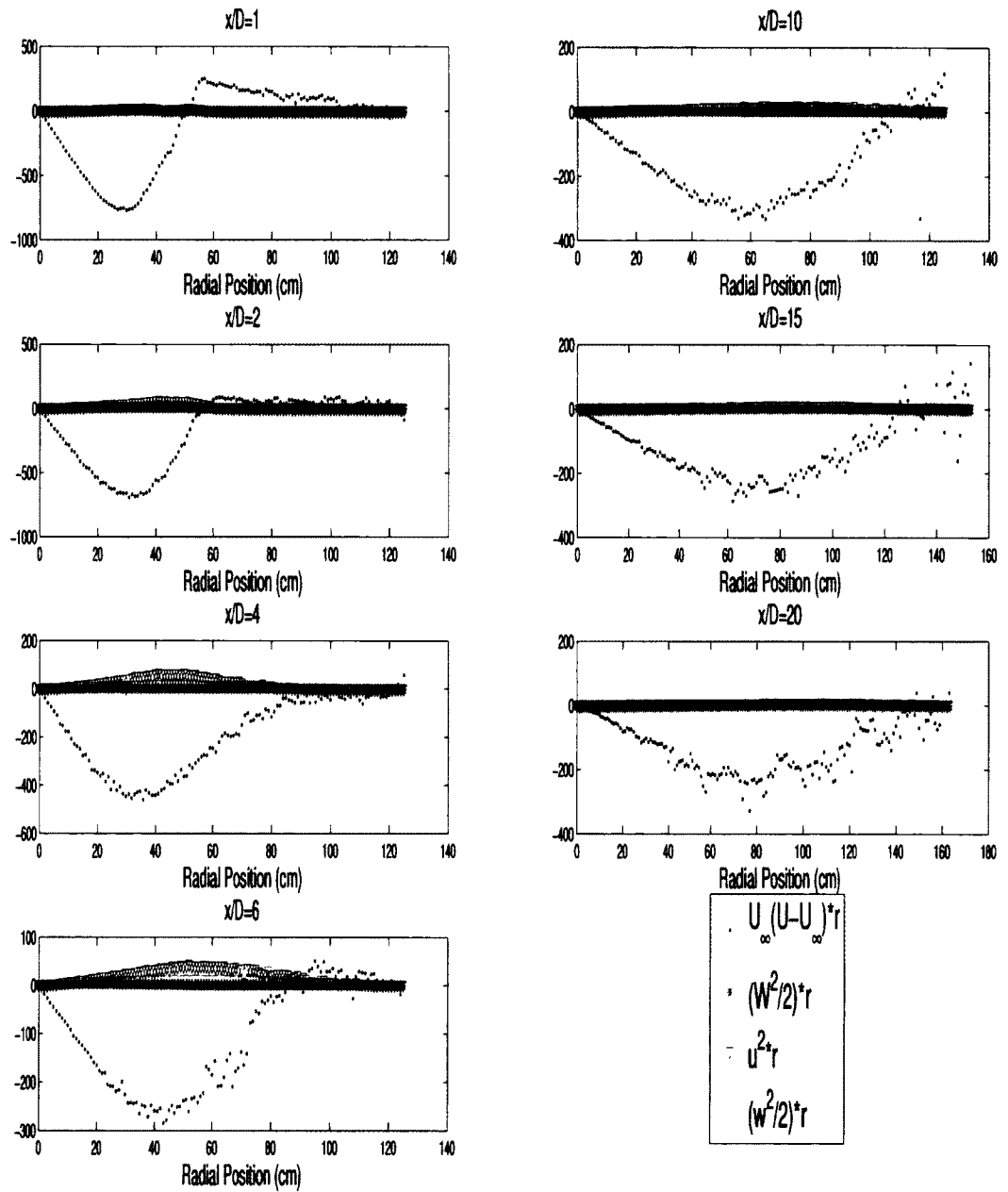
Figure 4-26. Terms of the streamwise momentum integrand plotted separately to show the impact of each term on the streamwise momentum integral plotted in Figure 4-23 (TSR=2.5)

The rate at which kinematic linear and angular momentum is swept downstream is presented in Figure 4-23 and Figure 4-24, based on the integral equations introduced in equations 2.5 and 2.6, respectively. Both quantities should remain constant as discussed in Chapter 2, and are seen to do so only approximately. Each term in the integrand of equations 2.5 and 2.6 is plotted separately for each downstream location in Figures 4-25, 4-26, 4-27, and 4-28. This allows the impact that each term has on the total kinematic momentum to be visualized. It can be seen that the second order turbulence terms increase downstream as Reynolds stresses work against the mean gradient to produce turbulent kinetic energy, however, they remain of second order, thereby validating the order of magnitude analysis. The second order terms reach their maximum at $x/D = 6$, after which they decay (and spread out) together with the first order term.

Time series were also analyzed in the time domain using autocorrelations at four radial positions for each downstream location in both the stream-wise and azimuthal directions. Correlations were analyzed for the first 10,000 samples (1 second $\approx$ 6 revolutions). These can be seen in Figure 4-29 for the stream-wise direction and Figure 4-30 for the azimuthal direction. The radial positions analyzed include: the centerline, half-radius, blade tip, and free-stream. The autocorrelation is a statistical measure which identifies the time over which a process is correlated with itself [19].

For the stream-wise direction, periodic trends are visible for all radial positions with the exception of data near the wake centerline. The highest frequency periodic forcing is apparent in the near wake at the blade tip (r=46). This is due to the tip vortices which are shed from the blade tips. As these vortices break down (downstream), the higher frequency forcing changes to a lower frequency correlation typical of a random process (turbulence) which is present until the furthest downstream locations ($x/D = 15$ and $x/D = 20$). At the centerline this periodic forcing is not present. At r=120, it would be expected that no periodic correlation exists. This is seen at
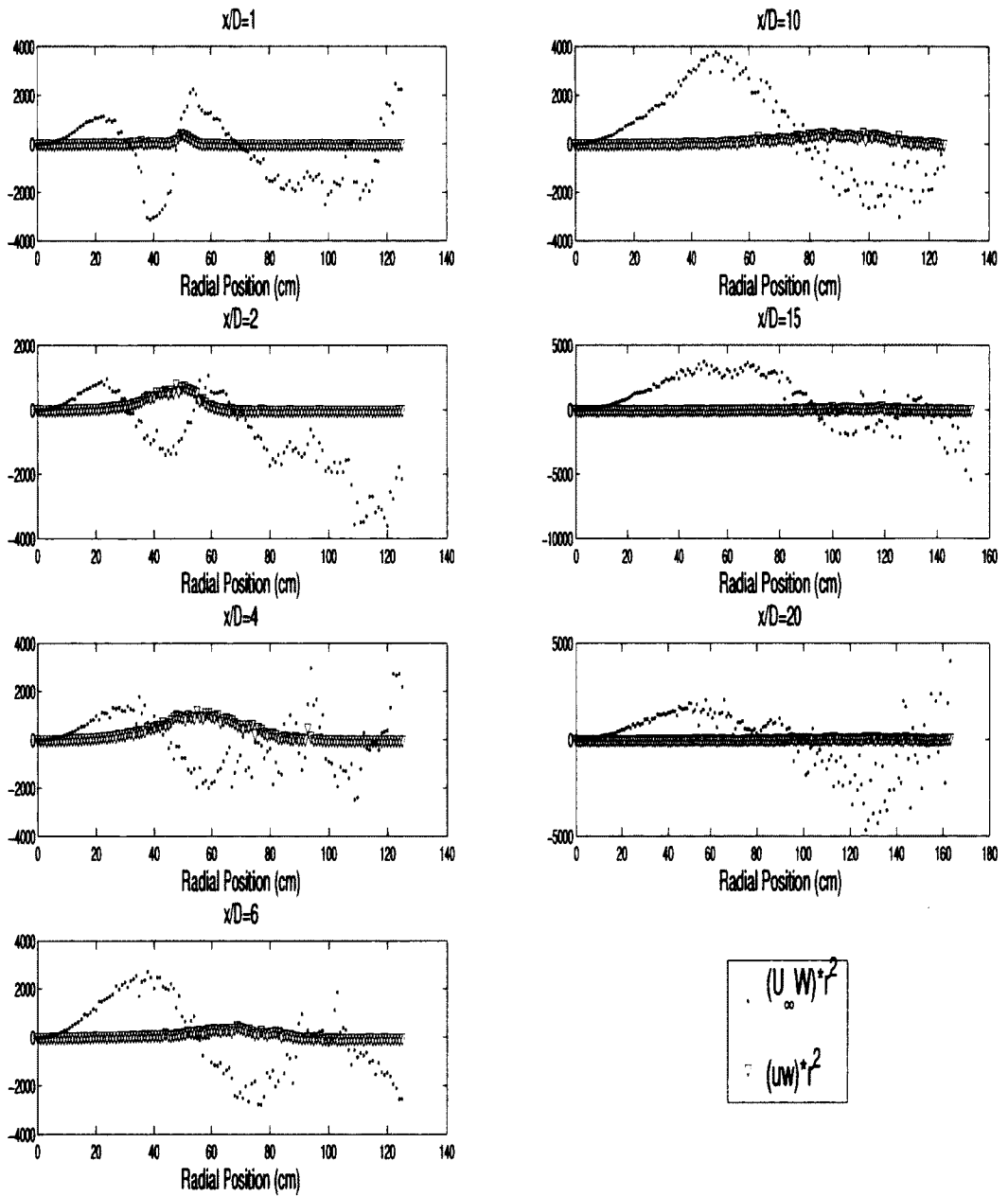
Figure 4-27. Terms of the angular momentum integrand plotted separately to show the impact of each term on the angular momentum integral plotted in Figure 4-24 (TSR=2.0)

68
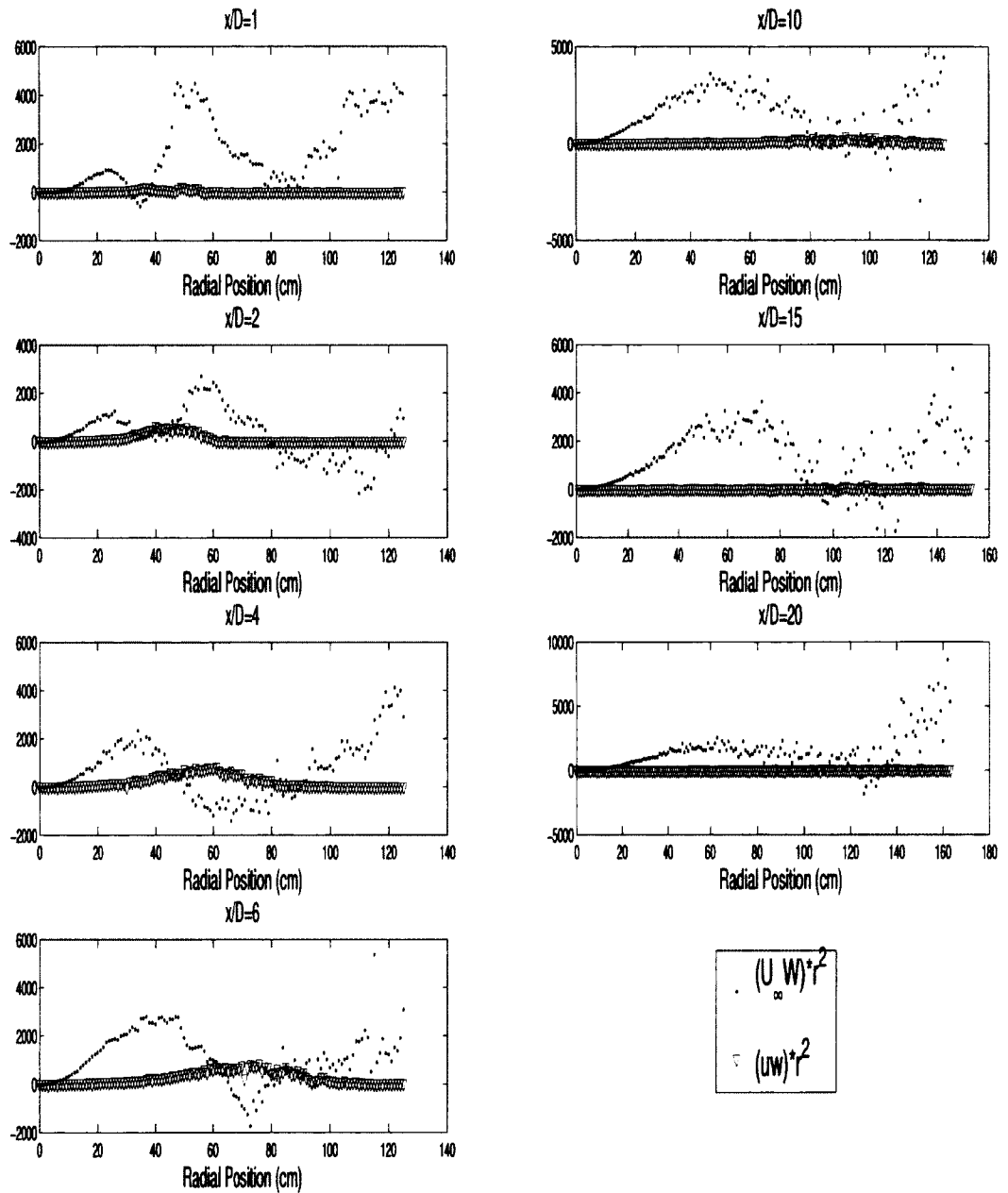
Figure 4-28. Terms of the angular momentum integrand plotted separately to show the impact of each term on the angular momentum integral plotted in Figure 4-24 (TSR=2.5)

$x/D = 1$ and $x/D = 2$, however the experiments further from the rotor appear to show this periodic forcing again. This is due to the turbulence which remains at this radial location downstream. Although not apparent in the means, there still appears to be wake effects visible in the turbulence statistics.

The autocorrelations in the azimuthal direction are shown in Figure 4-30. They show trends similar to those of the stream-wise autocorrelations, with the exception of the wake centerline. Periodic trends are seen at the wake centerline at all locations beyond $x/D = 1$. This concurs with the mean swirl, which does not appear to go all the way to zero at the centerline, as would be expected.

The integral scale can be calculated by integrating the correlation coefficient. This represents the time scale that a measurement is correlated with itself [19]. The integral scale was calculated for each downstream location and the same radial positions as the presented autocorrelations. These are shown in Figure 4-31 for $\lambda = 2.0$ and Figure 4-32 for $\lambda = 2.5$. The integral scale based on the stream-wise component is on the left hand side and the azimuthal component is on the right hand side. It is difficult to draw any conclusions from these, which may be due to the duration at which they are integrated over. Each auto-correlation was only done for the first 10,000 samples (or 1 second), in an attempt to find the zero-crossing. This may not be enough time to obtain valuable insight from the integration.
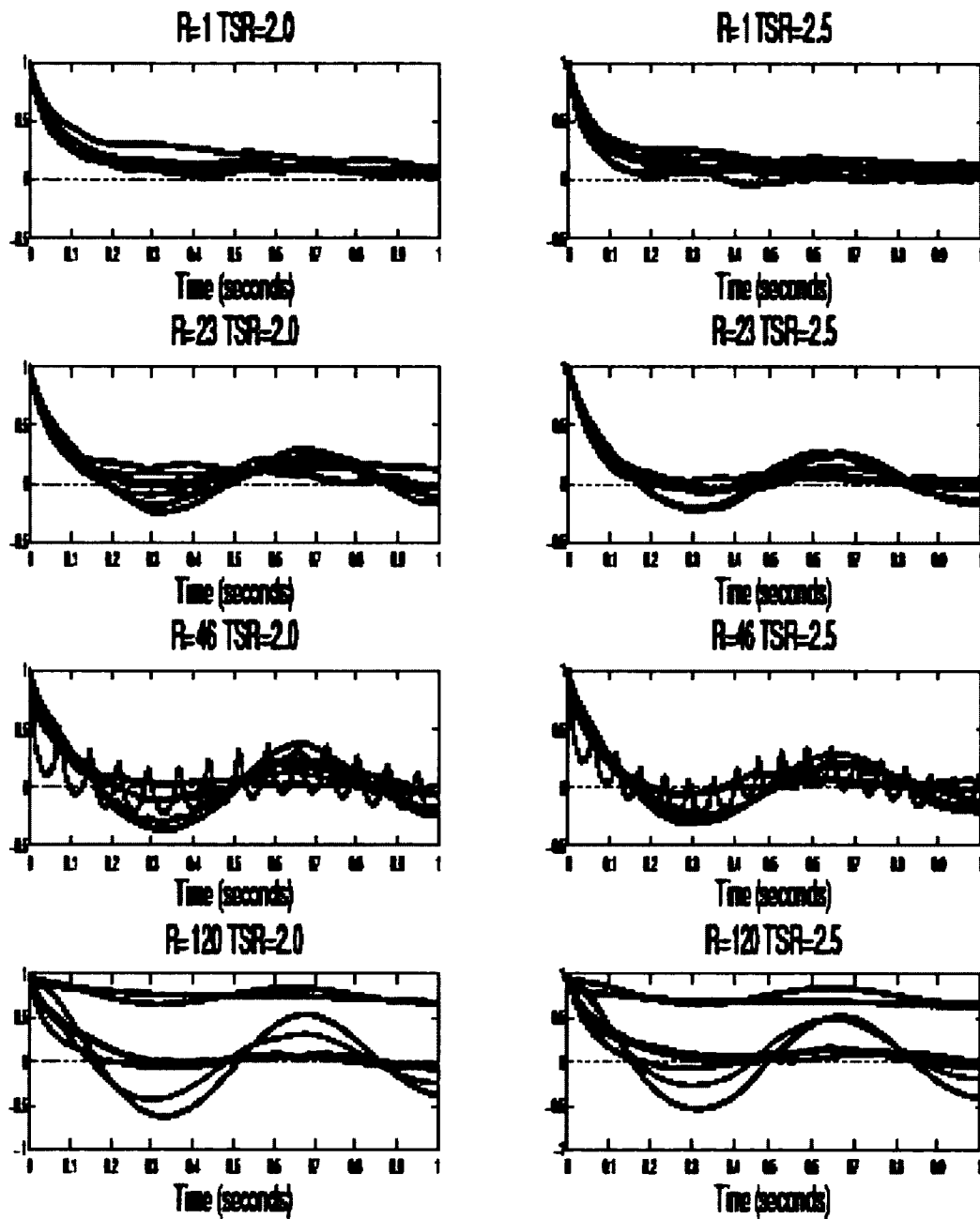
Figure 4-29. Streamwise auto-correlation at four separate radial positions. (TSR=2.0 on left, TSR=2.5 on right).Each color represents a different downstream location: 1D-red, 2D-green, 4D-red, 6D-aqua, 10D-purple, 15D-yellow, 20D-black.
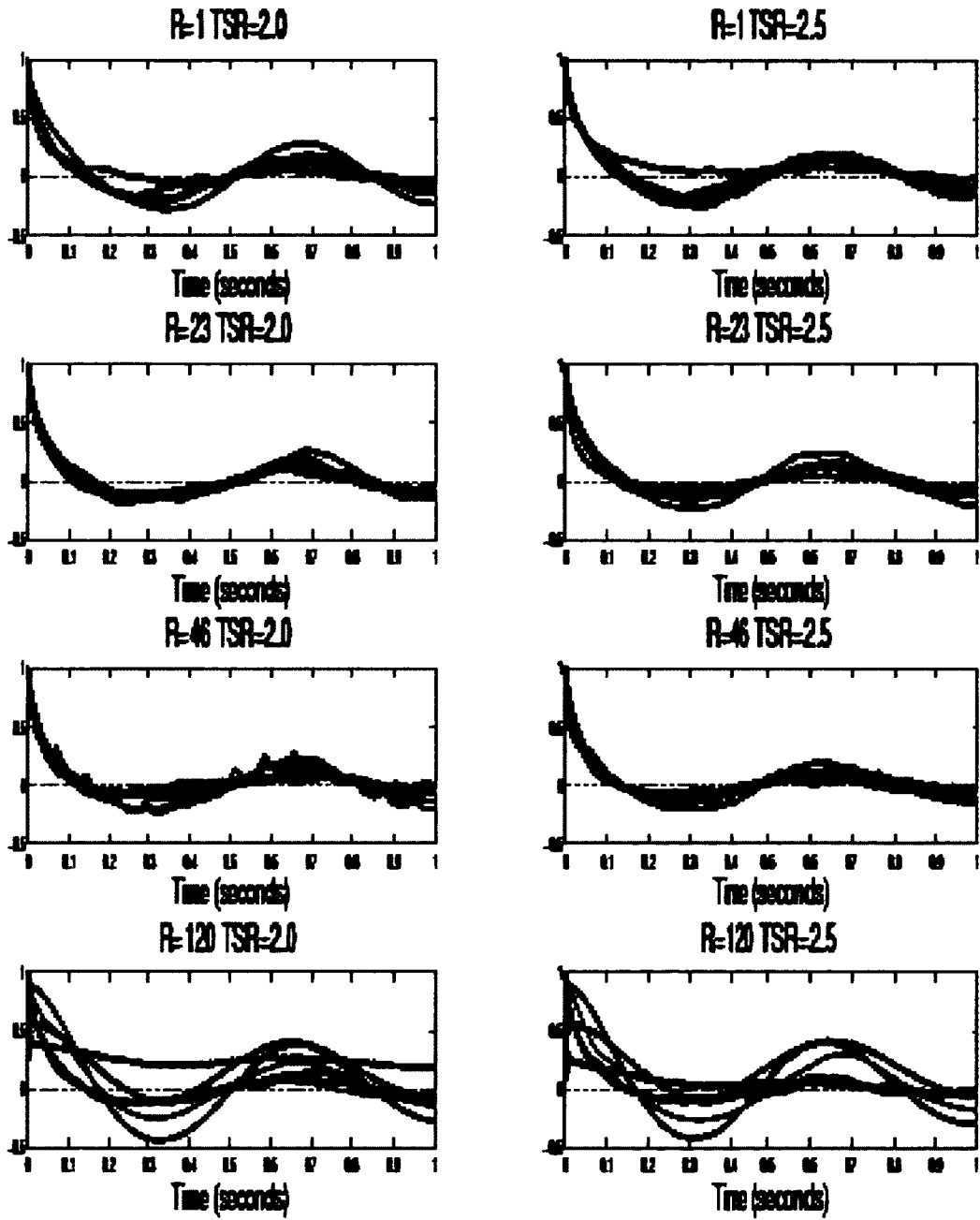
Figure 4-30. Azimuthal auto-correlation at four separate radial positions. (TSR=2.0 on left, TSR=2.5 on right). Each color represents a different downstream location: 1D-red, 2D-green, 4D-red, 6D-aqua, 10D-purple, 15D-yellow, 20D-black.
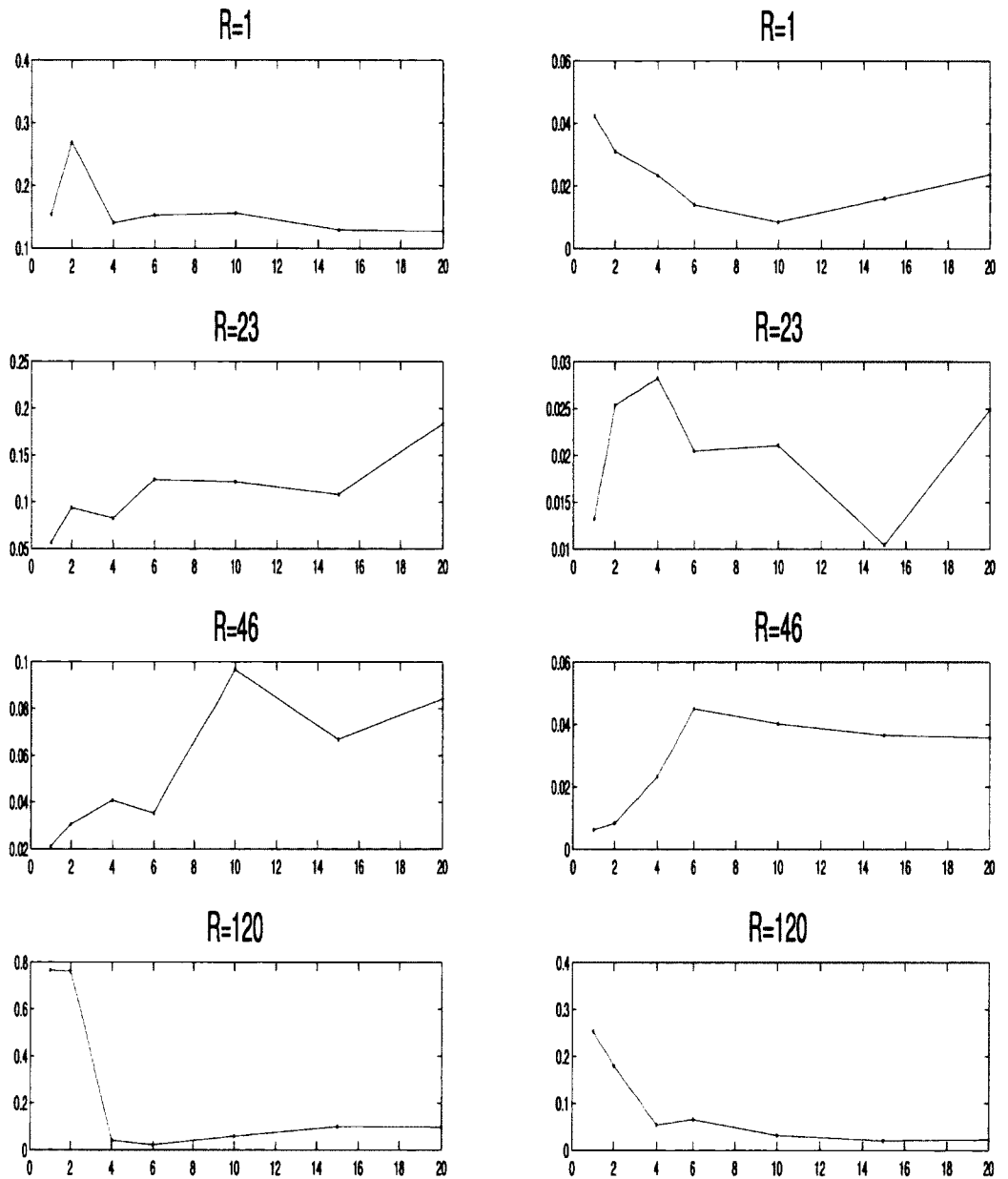
Figure 4-31. Integral scale at four separate radial positions for TSR=2.0 (streamwise on left, azimuthal on right).
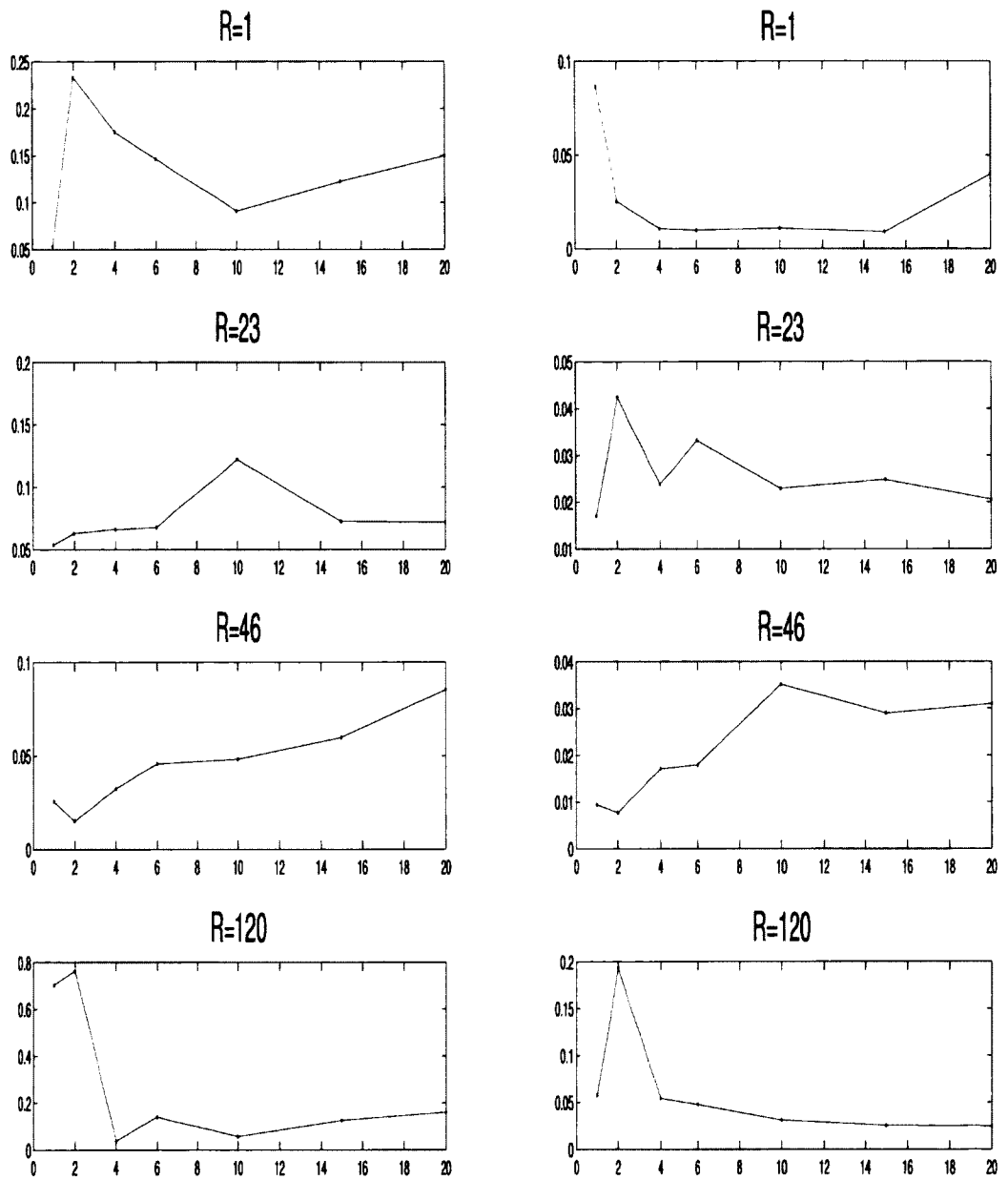
Figure 4-32. Integral scale at four separate radial positions for TSR=2.5 (streamwise on left, azimuthal on right).

CHAPTER 5

SUMMARY AND CONCLUSIONS

There is a need for detailed experimental data on turbulent axisymmetric wakes with rotation, with application to wind turbines, both at the (large) wind tunnel scale where conditions can be controlled and at the field scale. The improvement of wind turbine array spacing and the correspondent increase in energy production are dependent on our understanding of the wakes of upstream turbines as well as the interaction between multiple wakes. It is important to characterize the wake of a single wind turbine before beginning a study of wake-wake interactions. An experimental investigation of the single turbine wake was performed a the UNH Flow Physics Facility. Pitot-static tube and hot-wire anemometry measurements were performed at seven locations up to 20 rotor diameters downstream from the wind turbine. These measurements offer valuable information regarding the recovery of the wake and turbulence statistics in this region.

Measurements of the axial and azimuthal velocity fields in the rotating, turbulent wake downstream of a single 3-bladed wind turbine with rotor diameter of 0.91m were conducted, in the test section of the UNH Flow Physics Facility with a 6m x 2.7m cross section and 72m long test section. Measurements were performed up to 20 turbine diameters downstream with two types of probes: First, a pitot-static tube survey was performed to establish the spreading rate and the extent of the mean velocity deficit downstream. These results showed that the centerline velocity had recovered to 79% (21% deficit) at 6 diameters downstream, and that it had recovered to about 92% (8% deficit) at 20 diameters downstream.

Constant temperature anemometry with an X-wire was used to measure stream-wise and azimuthal velocity profiles. The X-wire measurements taken at 1 diameter show the existence of a 'near wake' rotational component. An increase in turbulent fluctuations in the radial location of the blade tip shows the shedding of tip vortices, which appear to contribute to the rotational component of the wake.

An equilibrium similarity analysis that derives scaling function from conditions for similarity obtained from the equations of motion was outlined. The experimental results were used to evaluate scaling functions for various flow quantities. The mean velocity deficit collapsed with the traditional scaling of $U_o \sim (U_\infty - U_{cl}) \sim x^{-\frac{2}{3}}$, while first evidence for a new scaling function for the mean swirling component $W_{max} \sim x^{-1} \sim U_o^{\frac{3}{2}}$ was found.

The similarity solution for the mean velocity deficit appears to be reached closer to the wake generator than in previous studies. Whether this is in part due to the swirl, or simply a result of the high initial Reynolds number based on turbine diameter and free stream velocity of almost 500,000 could not be established in this study and needs to be investigated further. This single turbine wake data set also provides pertinent information required for the continuation of these wind turbine wake and array optimization studies. The insight gained from these studies can ultimately be used to guide wind farm array spacing and help minimize array losses.

BIBLIOGRAPHY

[1] AA Lab Systems LTD. AN-1003 Hot Wire and Film Anemometry System. User's Manual. Wilmington, DE.

[2] American Wind Energy Association (AWEA). Web. 08 Apr. 2013.

[3] Barthelmie R.J.; Folkerts L; Larsen G; Rados K; Pryor S; Frandsen S; Lange B; Schepers G (2005) Comparison of wake model simulations with offshore wind turbine wake profiles measured by sodar. *J. Atmospheric and Oceanic Technology* 23:888-901.

[4] Barthelmie, R.J., et al. (2009) Modelling and measuring flow and wind turbine wakes in large wind farms offshore. *Wind Energy*, 12, 431-444.

[5] Barthelmie R.J.; Pryor SC; Frandsen ST; Hansen KS; Schepers JG; Rados K; Schlez W; Neubert A; Jensen LE; Neckelmann S (2010) Quantifying the Impact of Wind Turbine Wakes on Power Output at Offshore Wind Farms. *J. Atmospheric and Oceanic Technology* 27:1302-1317.

[6] M. Bevilaqua, P. S. Lykoudis (1978) Turbulence memory in self-preserving wakes. *J. Fluid Mech.* 89, 589.

[7] Cal RB; Lebron J; Castillo L; Kang HS; Meneveau C (2010) Experimental study of the horizontally averaged flow structure in a model wind-turbine array boundary layer. *J. Renewable and Sustainable Energy 2*, 13-106.

[8] C. Cannon (1991) Large-scale structures and the spatial evolution of wakes behind axisymmetric bluff bodies. Ph.D. thesis, Department of Aerospace and Mechanical Engineering, University of Arizona.

[9] Carmody, T (1964) Establishment of the wake behind a disk. *J. Basic Eng.* 86, 869.

[10] Chamorro L.P., Arndt R.E.A. Sotiropoulos F. (2011) Turbulence properties within a staggered wind farm. An experimental study. *Boundary-Layer Meteorol.* 141, 349-367.

[11] Davidson, P. A. (2004) Turbulence: An Introduction for Scientists and Engineers. Oxford, UK: Oxford UP, Print.

[12] Dufresne N; Wosnik M (2013) Experimental investigation and similarity solution for the axisymmetric turbulent wake with rotation. *Proc. ASME Fluids Engineering Division Summer Meeting*, Paper FED2013-0000, July 7-13, Incline Village, NV.

[13] Electrochemistry Encyclopedia. – Electroplating. Ernest B. Yeager Center for Electrochemical Sciences (YCES), Web. 05 Apr. 2013.

[14] Elkinton, C.N., Manwell, J.F., McGowan J.G. (2008) Optimizing the Layout of Offshore Wind Energy Systems. *Marine Technology Society Journal*, Volume 42, Number 2, pp.19-26, Summer 2008

[15] Ewing, D. (1995). Utilizing a Two Point Similarity Hypothesis to Determine Optimal Orthogonal Functions in Free Shear Layers. PhD thesis, State University of New York at Buffalo.

[16] Forsythe J; Klewicki J; White C; Wosnik M (2010) Status Update on the Flow Physics Facility at the University of New Hampshire. *Bull. Amer. Phys. Soc.*, Vol.55, No.16, p.306

[17] George, W.K. (1989) The Self-Preservation of Turbulent Flows and Its Relation to Initial Conditions and Coherent Structures. *Advances In Turbulence.*

[18] George, W.K. (1995) Some new ideas for similarity of turbulent shear flows, *Proc. ICHMT Symposium on Turbulence, Heat and Mass Transfer, Lisbon*, Portugal (1994), edited by K. Hanjalic and J. C. F. Pereira-Begell, New York.

[19] George, W.K. Lectures in Turbulence for the 21st Century. Chalmers University of Technology, Gothenburg, Sweden. Lecture.

[20] Johansson, Peter B.V. (2002) The Axisymmetric Turbulent Wake. Ph.D. Thesis. Chalmers University of Technology.

[21] Johansson, Peter B.V., George, W.K., Gourlay, M.J. (2003) Equilibrium Similarity, Effects of Initial Conditions and Local Reynolds Number on the Axisymmetric Wake. *Physics of Fluids* 15.3: 603-617.

[22] Johansson, Peter B.V.; George, William K. (2006) The far downstream evolution of the high-Reynolds-number axisymmetric wake behind a disk. Part 1. Single-point statistics. Journal of Fluid Mechanics, v 555, May, 2006, p 363-385

[23] Johansson A V (1992) A low speed wind-tunnel with extreme flow quality - design and tests. *Prog.* ICAS Congress, pp. 1603-1611. ICAS-92-3.8.1.

[24] Kelley, N.D, Jonkman B.J.; Scott, GN, Pichugina, YL (2007) Presented at the *American Wind Energy Association Wind Power Conference and Exhibition* Los Angeles, California June 3-7.

[25] Kern, S., Belloni, C., Aalburg, C. (2010) Wake model benchmarking using Li-DAR wake measurements of multi MW turbines. *European Wind Energy Conference 2010*, Warsaw, Poland, ISBN: 978-1-61782-310-7

[26] Klewicki (2011) Brief Status Report on the Flow Properties in the UNH Flow Physics Facility (FPF), Internal report to FPF Scientific Steering Committee, November.

[27] Lebron J., Cal RB., Kang H-S., Castillo L., Meneveau C., (2009) Interaction Between a Wind Turbine Array and a Turbulent Boundary Layer. *11th Americas Conference on Wind Engineering* - San Juan, Puerto Rico June 22-26.

[28] Moser, R.D., Rogers, M.M., and Ewing, D.W. (1998) Self-similarity of time-evolving plane wakes. *Journal of Fluid Mechanics*, 367:255289.

[29] Musial W; Butterfield S; McNiff B (2007) Improving Wind Turbine Gearbox Reliability. *European Wind Energy Conference*, Milan, Italy, May 710, Conference Paper NREL/CP-500-41548.

[30] Panton, R.L. (1984) Incompressible Flow. 3rd ed. John Wiley & Sons Inc.

[31] Reynolds, A.J. (1962) Similarity in Swirling Wakes and Jets. *Fluid Mech.*, vol. 14, pp 241-243.

[32] Schlez W., Neubert A., Smith G. (2006) New developments in precision wind farm modeling. *German Wind Energy Conference* DEWEK, Bremen, Germany.

[33] Sheng S. Editor (2010) Wind Turbine Micropitting Workshop: A Recap. *Technical Report NREL/TP-500-46572.*

[34] Shiri, A. (2010) Turbulence Measurements in a Natural Convection Boundary Layer and a Swirling Jet. Ph.D. Thesis. Chalmers University of Technology.

[35] Spurk, J.H. (1993) Stroemungslehre. *Springer Verlag*, Berlin-Heidelberg.

[36] Steiger M.H and Bloom M.H. (1962) Linearized Swirling Wakes. *Physics of Fluids* v5, Issue 9 1027-32.

[37] Stark, Anne M. (2011) In the Wake of Wind. *Lawrence Livermore National Laboratory NR-11-04-06* (26 Apr. 2011). Web.

[38] Tennekes, H. and Lumley, J. (1972) A first course in Turbulence. MIT Press, Cambridge, MA.

[39] Townsend A.A. (1976) The Structure of Turbulent Shear Flow. Cambridge University Press, Cambridge, UK.

[40] Tropea, Cameron; Yarin, Alexander L.; Foss, John F. (Eds.) (2007), *Springer Handbook of Experimental Fluid Mechanics.*

[41] Trujillo J., Bingol F., Larsen G.C., Mann J., Kuhn M. (2011) Light detection and ranging measurements of wake dynamics. Part II: two-dimensional scanning. *Wind Energy* 14:61-75.

[42] J.K.E. Tunaley (2010) Ships Turbulent Propeller Wake: Combined Swirling and Linear Momentum Wake. *LRDC Technical Report*, April 2010.

[43] United States Department of Energy, Energy Information Administration (EIA), Office of Energy Markets and End Use, Annual Energy Review 2010, DOE/EIA-0384, available at http://www.eia.gov/totalenergy/data/annual/

[44] United States Department of Energy, Energy Information Administration (EIA), Office of Energy Markets and End Use, Annual Energy Review 2011, DOE/EIA-0384, available at http://www.eia.gov/totalenergy/data/annual/

[45] United States Department of Energy, Energy Information Administration (EIA), Office of Energy Markets and End Use, International Energy Outlook 2010, DOE/EIA-0484, available at http://www.eia.gov/oiaf/ieo/pdf/0484(2010).pdf

[46] United States Department of Energy: 20% Wind Energy by 2030 Increasing Wind Energys Contribution to U.S. Electricity Supply DOE/GO-102008-2567, July 2008, http://www.nrel.gov/docs/fy08osti/41869.pdf

[47] Vanderwende B.J., and Lundquist J.K. (2012) The modification of wind turbine performance by statistically distinct atmospheric regimes. *Environmental Research Letters*, 7: 034-035.

[48] Vermeer L.J., Sorensen J.N., Crespo A. (2003) Wind turbine wake aerodynamics. *Progress in Aerospace Sciences 39* 467-510

[49] Vincenti P., Morrill-Winter C., Klewicki J., White C., Wosnik M. (2012) Canonical boundary layer properties at high Reynolds number as measured in the UNH Flow Physics Facility. *Bull. Amer. Phys. Soc.*, 57 No.17, p.279.

[50] Wosnik, M. (2011) Equilibrium Similarity Theory for Axisymmetric Turbulent Wakes with Rotation. *American Physical Society Division of Fluid Dynamics Annual Meeting.* Baltimore, MD.

Appendix 1: Governing Equations

The governing equations for the turbulent axisymmetric wake with swirl are derived in cylindrical coordinates (x, r, θ). The instantaneous velocity components in the in axial, radial and azimuthal directions are $\tilde{u}$, $\tilde{v}$ and $\tilde{w}$, respectively. Gravitational forces are neglected. The flow is assumed to be steady state (really: stationary in the mean), hence temporal derivatives $(\partial/\partial t)$ are also neglected.

5.1 Continuity and Momentum Equations

The continuity and momentum equations for a Newtonian fluid in cylindrical coordinates are given by (e.g., [35, 30]):

Continuity Equation:

$$\frac{\partial}{\partial x}(\rho\tilde{u}) + \frac{1}{r}\frac{\partial}{\partial r}(\rho r\tilde{v}) + \frac{1}{r}\frac{\partial}{\partial \theta}(\rho\tilde{w}) = 0 \tag{5.1}$$

Momentum Equation in Streamwise (Axial) Direction:

$$\tilde{u}\frac{\partial \tilde{u}}{\partial x} + \tilde{v}\frac{\partial \tilde{u}}{\partial r} + \tilde{w}(\frac{1}{r}\frac{\partial \tilde{u}}{\partial \theta}) = -\frac{1}{\rho}\frac{\partial \tilde{p}}{\partial x} + \frac{2}{\rho}\nabla \cdot (\mu\tilde{S}_x) \tag{5.2}$$

Momentum Equation in Radial Direction:

$$\tilde{u}\frac{\partial \tilde{v}}{\partial x} + \tilde{v}\frac{\partial \tilde{v}}{\partial r} + \tilde{w}\left(\frac{1}{r}\frac{\partial \tilde{v}}{\partial \theta} - \frac{\tilde{w}}{r}\right) = -\frac{1}{\rho}\frac{\partial \tilde{p}}{\partial r} + \frac{2}{\rho}\nabla \cdot (\mu\tilde{S}_r) \tag{5.3}$$

Momentum Equation in Tangential Direction:

$$\tilde{u}\frac{\partial \tilde{w}}{\partial x} + \tilde{v}\frac{\partial \tilde{w}}{\partial r} + \tilde{w}\left(\frac{1}{r}\frac{\partial \tilde{w}}{\partial \theta} + \frac{\tilde{v}}{r}\right) = -\frac{1}{\rho}\left(\frac{1}{r}\frac{\partial \tilde{p}}{\partial \theta}\right) + \frac{2}{\rho}\nabla \cdot (\mu\tilde{S}_\theta) \tag{5.4}$$

The viscous terms on the right hand side of the component momentum equations are generally defined as follows (neglecting the 2nd viscosity):

$$2\nabla \cdot (\mu\tilde{S}_x) \equiv 2\frac{\partial}{\partial x}\left(\mu\frac{\partial \tilde{u}}{\partial x}\right) + \frac{1}{r}\frac{\partial}{\partial r}\left(r\mu(\frac{\partial \tilde{u}}{\partial r} + \frac{\partial \tilde{v}}{\partial x})\right) + \frac{1}{r}\frac{\partial}{\partial \theta}\left(\mu(\frac{\partial \tilde{w}}{\partial x} + \frac{1}{r}\frac{\partial \tilde{u}}{\partial \theta})\right) \tag{5.5}$$

$$2\nabla \cdot (\mu\tilde{S}_r) \equiv \frac{\partial}{\partial x}\left(\mu(\frac{\partial \tilde{u}}{\partial r} + \frac{\partial \tilde{v}}{\partial x})\right) + 2\frac{1}{r}\frac{\partial}{\partial r}\left(r\mu\frac{\partial \tilde{v}}{\partial r}\right) + \frac{1}{r}\frac{\partial}{\partial \theta}\left(\mu(r\frac{\partial}{\partial r}(\frac{\tilde{w}}{r}) + \frac{1}{r}\frac{\partial \tilde{v}}{\partial \theta})\right)$$

$$- 2\mu\left(\frac{1}{r^2}\frac{\partial \tilde{w}}{\partial \theta} + \frac{\tilde{v}}{r^2}\right) \tag{5.6}$$

$$2\nabla \cdot (\mu\tilde{S}_\theta) \equiv \frac{\partial}{\partial x}\left(\mu(\frac{\partial \tilde{w}}{\partial x} + \frac{1}{r}\frac{\partial \tilde{u}}{\partial \theta})\right) + \frac{1}{r^2}\frac{\partial}{\partial r}\left(\mu r^2(r\frac{\partial}{\partial r}(\frac{\tilde{w}}{r}) + \frac{1}{r}\frac{\partial \tilde{v}}{\partial \theta})\right)$$

$$+ \frac{1}{r}\frac{\partial}{\partial \theta}\left(2\mu(\frac{1}{r}\frac{\partial \tilde{w}}{\partial \theta} + \frac{\tilde{v}}{r})\right) \tag{5.7}$$

The assumption of incompressibility is reasonable for wakes with rotation generated by wind turbines. Viscosity is a function of temperature, however, it can be as-

sumed to be constant here (If variation of viscosity with temperature is of concern, then derivations of governing equations should be carried out by keeping viscosity in inside the divergence ($\nabla \cdot (\mu \mathbf{S}_{ij})$). Note that decomposing viscosity(μ) into mean and fluctuating parts would add viscosity-velocity correlations and thereby significant complexity!). *Reynolds decomposition* is now applied to divide the instantaneous components in the equations above into a mean (uppercase) and fluctuating (lowercase) part:

$$
\begin{array}{lll}
\text{Streamwise (axial) velocity}(x) & : & \tilde{u} = U + u \\
\text{Radial velocity}(r) & : & \tilde{v} = V + v \\
\text{Tangential Velocity}(\theta) & : & \tilde{w} = W + w \\
\text{Pressure} & : & \tilde{p} = P + p
\end{array}
$$

These terms are substituted into the continuity and momentum equations, which are then averaged. The mean continuity equation becomes:

Averaged Continuity Equation:

$$
\frac{\partial U}{\partial x} + \frac{1}{r}\frac{\partial (rV)}{\partial r} + \frac{1}{r}\frac{\partial W}{\partial \theta} = 0 \tag{5.8}
$$

The mean momentum equations become:

Averaged Momentum Equation in Streamwise (Axial) Direction:

$$
U\frac{\partial U}{\partial x} + V\frac{\partial U}{\partial r} + \frac{W}{r}\frac{\partial U}{\partial \theta} = -\frac{1}{\rho}\frac{\partial P}{\partial x} + \nu\left[\frac{\partial^2 U}{\partial x^2} + \frac{1}{r}\frac{\partial}{\partial r}\left(r\frac{\partial U}{\partial r}\right) + \frac{1}{r^2}\frac{\partial^2 U}{\partial \theta^2}\right]
$$
$$
- \left(\frac{\partial \overline{u^2}}{\partial x} + \frac{\partial \overline{uv}}{\partial r} + \frac{1}{r}\frac{\partial \overline{uw}}{\partial \theta} + \frac{\overline{uv}}{r}\right) \tag{5.9}
$$

Averaged Momentum Equation in Radial Direction:

$$
U\frac{\partial V}{\partial x} + V\frac{\partial V}{\partial r} + \frac{W}{r}\frac{\partial V}{\partial \theta} - \frac{W^2}{r} = -\frac{1}{\rho}\frac{\partial P}{\partial r} + \nu\left[\frac{\partial^2 V}{\partial x^2} + \frac{\partial}{\partial r}\left(\frac{1}{r}\frac{\partial}{\partial r}(rV)\right) + \frac{1}{r^2}\frac{\partial^2 V}{\partial \theta^2} - \frac{2}{r^2}\frac{\partial W}{\partial \theta}\right]
$$
$$
- \left(\frac{\partial \overline{uv}}{\partial x} + \frac{\partial \overline{v^2}}{\partial r} + \frac{1}{r}\frac{\partial \overline{vw}}{\partial \theta} - \frac{\overline{w^2} - \overline{v^2}}{r}\right) \tag{5.10}
$$

Averaged Momentum Equation in Tangential Direction:

$$
U\frac{\partial W}{\partial x} + V\frac{\partial W}{\partial r} + \frac{W}{r}\frac{\partial W}{\partial \theta} + \frac{VW}{r} = -\frac{1}{r\rho}\frac{\partial P}{\partial \theta} + \nu\left[\frac{\partial^2 W}{\partial x^2} + \frac{\partial}{\partial r}\left(\frac{1}{r}\frac{\partial}{\partial r}(rW)\right) + \frac{1}{r^2}\frac{\partial^2 W}{\partial \theta^2} + \frac{2}{r^2}\frac{\partial V}{\partial \theta}\right]
$$
$$
- \left(\frac{\partial \overline{uw}}{\partial x} + \frac{\partial \overline{vw}}{\partial r} + \frac{1}{r}\frac{\partial \overline{w^2}}{\partial \theta} + \frac{\overline{vw}}{r}\right) \tag{5.11}
$$

The averages of non-linear occurrences of fluctuating velocities in the averaged momentum equations are generally non-zero. The resulting terms were re-written

with the help of the fluctuating continuity equation and moved to the right-hand side of the momentum equations since they act as apparent stresses, also referred to as "Reynolds stresses" (cf. [38]

Since the flow is axisymmetric, there must be symmetry with respect to the θ-direction, i.e, $(\partial/\partial\theta = 0)$. In other words, the flow is statistically homogeneous flow in tangential direction. However, there is expected to be a mean swirl component, and $W \neq 0$. The averaged continuity and momentum equations thus further simplify:

Averaged Continuity Equation:

$$\frac{\partial U}{\partial x} + \frac{1}{r}\frac{\partial(rV)}{\partial r} = 0 \tag{5.12}$$

The mean momentum equations become:

Averaged Momentum Equation in Streamwise (Axial) Direction:

$$U\frac{\partial U}{\partial x} + V\frac{\partial U}{\partial r} = -\frac{1}{\rho}\frac{\partial P}{\partial x} + \nu\left[\frac{\partial^2 U}{\partial x^2} + \frac{1}{r}\frac{\partial}{\partial r}\left(r\frac{\partial U}{\partial r}\right)\right]$$
$$- \left(\frac{\partial \overline{u^2}}{\partial x} + \frac{1}{r}\frac{\partial}{\partial r}(r\overline{uv})\right) \tag{5.13}$$

Averaged Momentum Equation in Radial Direction:

$$U\frac{\partial V}{\partial x} + V\frac{\partial V}{\partial r} - \frac{W^2}{r} = -\frac{1}{\rho}\frac{\partial P}{\partial r} + \nu\left[\frac{\partial^2 V}{\partial x^2} + \frac{\partial}{\partial r}\left(\frac{1}{r}\frac{\partial}{\partial r}(rV)\right)\right]$$
$$- \left(\frac{\partial \overline{uv}}{\partial x} + \frac{\partial \overline{v^2}}{\partial r} - \frac{\overline{w^2} - \overline{v^2}}{r}\right) \tag{5.14}$$

Averaged Momentum Equation in Tangential Direction:

$$U\frac{\partial W}{\partial x} + V\frac{\partial W}{\partial r} + \frac{VW}{r} = \nu\left[\frac{\partial^2 W}{\partial x^2} + \frac{\partial}{\partial r}\left(\frac{1}{r}\frac{\partial}{\partial r}(rW)\right)\right]$$
$$- \left(\frac{\partial \overline{uw}}{\partial x} + \frac{\partial \overline{vw}}{\partial r} + \frac{\overline{vw}}{r}\right) \tag{5.15}$$

5.2 Reynolds Stress Transport Equations

To calculate the transport equations for the Reynolds stresses in an incompressible, high-Reynolds number flow, we subtract instantaneous momentum equations (5.2,5.3 and 5.4) from averaged momentum equations (5.13, 5.14 and 5.15):

$$U\frac{\partial u}{\partial x}+V\frac{\partial u}{\partial r}+\frac{W}{r}\frac{\partial u}{\partial \theta}=-\frac{1}{\rho}\frac{\partial p}{\partial x}+\frac{2}{\rho}\nabla\cdot(\mu s'_x)-\left\{u\frac{\partial U}{\partial x}+v\frac{\partial U}{\partial r}+\frac{w}{r}\frac{\partial U}{\partial \theta}\right\}$$

$$-\left\{\left(u\frac{\partial u}{\partial x}+v\frac{\partial u}{\partial r}+\frac{w}{r}\frac{\partial u}{\partial \theta}\right)-\left(\overline{u\frac{\partial u}{\partial x}}+\overline{v\frac{\partial u}{\partial r}}+\overline{\frac{w}{r}\frac{\partial u}{\partial \theta}}\right)\right\} \quad (5.16)$$

$$U\frac{\partial v}{\partial x}+V\frac{\partial v}{\partial r}+\frac{W}{r}\frac{\partial v}{\partial \theta}-W\frac{w}{r}=-\frac{1}{\rho}\frac{\partial p}{\partial r}+\frac{2}{\rho}\nabla\cdot(\mu s'_r)-\left\{u\frac{\partial V}{\partial x}+v\frac{\partial V}{\partial r}+\frac{w}{r}\frac{\partial V}{\partial \theta}-w\frac{W}{r}\right\}$$

$$-\left\{\left(u\frac{\partial v}{\partial x}+v\frac{\partial v}{\partial r}+\frac{w}{r}\frac{\partial v}{\partial \theta}-\frac{w^2}{r}\right)-\left(\overline{u\frac{\partial v}{\partial x}}+\overline{v\frac{\partial v}{\partial r}}+\overline{\frac{w}{r}\frac{\partial v}{\partial \theta}}-\overline{\frac{w^2}{r}}\right)\right\} \quad (5.17)$$

$$U\frac{\partial w}{\partial x}+V\frac{\partial w}{\partial r}+\frac{W}{r}\frac{\partial w}{\partial \theta}+V\frac{w}{r}=-\frac{1}{\rho}\left(\frac{1}{r}\frac{\partial p}{\partial \theta}\right)+\frac{2}{\rho}\nabla\cdot(\mu s'_\theta)-\left\{u\frac{\partial W}{\partial x}+v\frac{\partial W}{\partial r}+\frac{w}{r}\frac{\partial W}{\partial \theta}+v\frac{W}{r}\right\}$$

$$-\left\{\left(u\frac{\partial w}{\partial x}+v\frac{\partial w}{\partial r}+\frac{w}{r}\frac{\partial w}{\partial \theta}+\frac{vw}{r}\right)-\left(\overline{u\frac{\partial w}{\partial x}}+\overline{v\frac{\partial w}{\partial r}}+\overline{\frac{w}{r}\frac{\partial w}{\partial \theta}}+\overline{\frac{vw}{r}}\right)\right\} \quad (5.18)$$

where s' refers to fluctuating viscous stress terms. Now each equation above is multiplied with each fluctuating velocity, and averaged. Combinations of the multiplied/averaged equations are then added together to form the Reynolds stress component transport equations as follow:

- Average ($u\times$ Eqn 5.16) + Average ($u\times$ Eqn 5.16):

$$U\frac{\partial \overline{u^2}}{\partial x}+V\frac{\partial \overline{u^2}}{\partial r}+\frac{W}{r}\frac{\partial \overline{u^2}}{\partial \theta}=-\frac{2}{\rho}\left\{\frac{\partial \overline{pu}}{\partial x}-<p\frac{\partial u}{\partial x}>\right\}+\frac{2}{\rho}<2u\nabla\cdot(\mu s'_x)>$$

$$-2\left\{\overline{u^2}\frac{\partial U}{\partial x}+\overline{uv}\frac{\partial U}{\partial r}+\frac{\overline{uw}}{r}\frac{\partial U}{\partial \theta}\right\}-\left\{\frac{\partial \overline{u^3}}{\partial x}+\frac{1}{r}\frac{\partial\, r\overline{u^2 v}}{\partial r}+\frac{1}{r}\frac{\partial \overline{u^2 w}}{\partial \theta}\right\} \quad (5.19)$$

- Avarage($v\times$ Eqn.5.17) + Average($v\times$ Eqn.5.17):

$$U\frac{\partial \overline{v^2}}{\partial x}+V\frac{\partial \overline{v^2}}{\partial r}+\frac{W}{r}\frac{\partial \overline{v^2}}{\partial \theta}-2W\frac{\overline{vw}}{r}=-\frac{2}{\rho}\left\{\frac{\partial \overline{pv}}{\partial r}-<p\frac{\partial v}{\partial r}>\right\}+\frac{2}{\rho}<2v\nabla\cdot(\mu s'_r)>$$

$$-2\left\{\overline{uv}\frac{\partial V}{\partial x}+\overline{v^2}\frac{\partial V}{\partial r}+\frac{\overline{vw}}{r}\frac{\partial V}{\partial \theta}-\overline{vw}\frac{W}{r}\right\}-\left\{\frac{\partial \overline{uv^2}}{\partial x}+\frac{1}{r}\frac{\partial\, r\overline{v^3}}{\partial r}+\frac{1}{r}\frac{\partial \overline{v^2 w}}{\partial \theta}-2\frac{\overline{vw^2}}{r}\right\}$$

$$(5.20)$$

84

- Average($w\times$ Eqn.5.18) + Average($w\times$ Eqn.5.18):

$$U\frac{\partial \overline{w^2}}{\partial x}+V\frac{\partial \overline{w^2}}{\partial r}+\frac{W}{r}\frac{\partial \overline{w^2}}{\partial \theta}+2V\frac{\overline{w^2}}{r} = -\frac{2}{r\,\rho}\left\{\frac{\partial \overline{pw}}{\partial \theta}-<p\frac{\partial w}{\partial \theta}>\right\}+\frac{2}{\rho}<2w\nabla\cdot(\mu s'_\theta)>$$

$$-2\left\{\overline{uw}\frac{\partial W}{\partial x}+\overline{vw}\frac{\partial W}{\partial r}+\frac{\overline{w^2}}{r}\frac{\partial W}{\partial \theta}+\overline{vw}\frac{W}{r}\right\}-\left\{\frac{\partial \overline{uw^2}}{\partial x}+\frac{1}{r}\frac{\partial r\overline{vw^2}}{\partial r}+\frac{1}{r}\frac{\partial \overline{w^3}}{\partial \theta}+2\frac{\overline{vw^2}}{r}\right\}$$

(5.21)

- Average($v\times$ Eqn.5.16) + Average($u\times$ Eqn.5.17)

$$U\frac{\partial \overline{uv}}{\partial x}+V\frac{\partial \overline{uv}}{\partial r}+\frac{W}{r}\frac{\partial \overline{uv}}{\partial \theta}-W\frac{\overline{uw}}{r} = -\frac{1}{\rho}\left\{\frac{\partial \overline{pv}}{\partial x}+\frac{\partial \overline{pu}}{\partial r}\right\}$$

$$+\frac{1}{\rho}\left\{<p\frac{\partial v}{\partial x}>+<p\frac{\partial u}{\partial r}>\right\}+\frac{2}{\rho}\left\{<v\nabla\cdot(\mu s'_x)>+<u\nabla\cdot(\mu s'_r)>\right\}$$

$$-\left\{\overline{uv}\frac{\partial U}{\partial x}+\overline{v^2}\frac{\partial U}{\partial r}+\frac{\overline{vw}}{r}\frac{\partial U}{\partial \theta}+\overline{u^2}\frac{\partial V}{\partial x}+\overline{uv}\frac{\partial V}{\partial r}+\frac{\overline{uw}}{r}\frac{\partial V}{\partial \theta}-\overline{uw}\frac{W}{r}\right\}$$

$$-\left\{\frac{\partial \overline{u^2v}}{\partial x}+\frac{1}{r}\frac{\partial r\,\overline{uv^2}}{\partial r}+\frac{1}{r}\frac{\partial uvw}{\partial \theta}-\frac{\overline{uw^2}}{r}\right\}$$

(5.22)

- Average($w\times$ Eqn.5.16) + Average($u\times$ Eqn.5.18)

$$U\frac{\partial \overline{uw}}{\partial x}+V\frac{\partial \overline{uw}}{\partial r}+\frac{W}{r}\frac{\partial \overline{uw}}{\partial \theta}+V\frac{\overline{uw}}{r} = -\frac{1}{\rho}\left\{\frac{\partial \overline{pw}}{\partial x}+\frac{1}{r}\frac{\partial \overline{pu}}{\partial \theta}\right\}$$

$$+\frac{1}{\rho}\left\{<p\frac{\partial w}{\partial x}>+\frac{1}{r}<p\frac{\partial u}{\partial \theta}>\right\}+\frac{2}{\rho}\left\{<w\nabla\cdot(\mu s'_x)>+<u\nabla\cdot(\mu s'_\theta)>\right\}$$

$$-\left\{\overline{uw}\frac{\partial U}{\partial x}+\overline{vw}\frac{\partial U}{\partial r}+\frac{\overline{w^2}}{r}\frac{\partial U}{\partial \theta}+\overline{u^2}\frac{\partial W}{\partial x}+\overline{uv}\frac{\partial W}{\partial r}+\frac{\overline{uw}}{r}\frac{\partial W}{\partial \theta}+\overline{uv}\frac{W}{r}\right\}$$

$$-\left\{\frac{\partial \overline{u^2w}}{\partial x}+\frac{1}{r}\frac{\partial r\,\overline{uvw}}{\partial r}+\frac{1}{r}\frac{\partial \overline{uw^2}}{\partial \theta}+\frac{\overline{uvw}}{r}\right\}$$

(5.23)

- Average($w\times$ Eqn.5.17) + Average($v\times$ Eqn.5.18)

85

$$U\frac{\partial \overline{vw}}{\partial x} + V\frac{\partial \overline{vw}}{\partial r} + \frac{W}{r}\frac{\partial \overline{vw}}{\partial \theta} - W\frac{\overline{w^2}}{r} + V\frac{\overline{vw}}{r} = -\frac{1}{\rho}\left\{\frac{\partial \overline{pw}}{\partial r} + \frac{1}{r}\frac{\partial \overline{pv}}{\partial \theta}\right\}$$

$$+\frac{1}{\rho}\left\{< p\frac{\partial w}{\partial r}> + \frac{1}{r}< p\frac{\partial v}{\partial \theta}>\right\} + \frac{2}{\rho}\{< v\nabla \cdot (\mu s'_\theta)> + < w\nabla \cdot (\mu s'_r)>\}$$

$$-\left\{\overline{uw}\frac{\partial V}{\partial x} + \overline{vw}\frac{\partial V}{\partial r} + \frac{\overline{w^2}}{r}\frac{\partial V}{\partial \theta} + \overline{uv}\frac{\partial W}{\partial x} + \overline{v^2}\frac{\partial W}{\partial r} + \frac{\overline{vw}}{r}\frac{\partial W}{\partial \theta} + (\overline{v^2} - \overline{w^2})\frac{W}{r}\right\}$$

$$-\left\{\frac{\partial \overline{uvw}}{\partial x} + \frac{1}{r}\frac{\partial r\,\overline{v^2w}}{\partial r} + \frac{1}{r}\frac{\partial vw^2}{\partial \theta} + \frac{\overline{v^2w}}{r} - \frac{\overline{w^3}}{r}\right\} \qquad (5.24)$$

Turbulent kinetic energy equation:

The equation for the turbulent kinetic energy in cylindrical coordinate can be obtained by adding the normal Reynolds stress equations and defining k, the average fluctuating kinetic energy per unit mass, as:

$$k \equiv \frac{1}{2}\overline{q^2} = \frac{1}{2}\left[\overline{u^2} + \overline{v^2} + \overline{w^2}\right] \qquad (5.25)$$

Turbulent kinetic energy equation:

$$U\frac{\partial k}{\partial x} + V\frac{\partial k}{\partial r} + \frac{W}{r}\frac{\partial k}{\partial \theta} - W\frac{\overline{vw}}{r} + V\frac{\overline{w^2}}{r} =$$

$$-\frac{1}{\rho}\left\{\frac{\partial \overline{pu}}{\partial x} + \frac{1}{r}\frac{\partial (r\overline{pv})}{\partial r} + \frac{1}{r}\frac{\partial \overline{pw}}{\partial \theta}\right\} - \frac{1}{2}\left\{\frac{\partial \overline{uq^2}}{\partial x} + \frac{1}{r}\frac{\partial (r\overline{vq^2})}{\partial r} + \frac{1}{r}\frac{\partial \overline{wq^2}}{\partial \theta}\right\} + \frac{2}{\rho}\nabla \cdot \mu < \vec{v}s_{ij}>$$

$$-\left\{\overline{u^2}\frac{\partial U}{\partial x} + \overline{uv}\frac{\partial U}{\partial r} + \frac{\overline{uw}}{r}\frac{\partial U}{\partial \theta} + \overline{uv}\frac{\partial V}{\partial x} + \overline{v^2}\frac{\partial V}{\partial r} + \frac{\overline{vw}}{r}\frac{\partial V}{\partial \theta} + \overline{uw}\frac{\partial W}{\partial x} + \overline{vw}\frac{\partial W}{\partial r} + \frac{\overline{w^2}}{r}\frac{\partial W}{\partial \theta}\right\}$$

$$-\frac{2}{\rho}\mu < \overline{s_{ij}s_{ij}}> \qquad (5.26)$$

Note that the incompressibility condition for the fluctuating continuity was used to eliminate the pressure-strain rate term.

In the turbulent kinetic energy e2quation, theviscous terms are split into the turbulence transport (or divergence) terms and dissipations, shown below:

- **Transport of kinetic energy due to viscous stresses:**

$$\frac{2}{\rho}\nabla\cdot\mu<\vec{\mathbf{v}}s_{ij}>\equiv\frac{\partial}{\partial x}\frac{\mu}{\rho}\left\{\frac{\partial k}{\partial x}+\frac{\partial\overline{u^2}}{\partial x}+\frac{1}{r}\frac{\partial r\overline{uv}}{\partial r}+\frac{1}{r}\frac{\partial\overline{uw}}{\partial\theta}\right\}$$

$$+\frac{1}{r}\frac{\partial}{\partial r}\frac{\mu}{\rho}r\left\{\frac{\partial k}{\partial r}+\frac{\partial\overline{uv}}{\partial x}+\frac{1}{r}\frac{\partial r\overline{v^2}}{\partial r}+\frac{1}{r}\frac{\partial\overline{vw}}{\partial\theta}-\frac{\overline{w^2}}{r}\right\}$$

$$+\frac{1}{r}\frac{\partial}{\partial\theta}\frac{\mu}{\rho}\left\{\frac{\partial k}{\partial\theta}+\frac{\partial\overline{uw}}{\partial x}+\frac{1}{r}\frac{\partial r\overline{vw}}{\partial r}+\frac{1}{r}\frac{\partial\overline{w^2}}{\partial\theta}+\frac{\overline{vw}}{r}\right\}\quad(5.27)$$

- **Rate of dissipation of turbulence kinetic energy:**

$$-\epsilon\equiv-\frac{2}{\rho}\mu<\overline{s_{ij}s_{ij}}>=-\frac{\mu}{\rho}\left\langle 2\left(\frac{\partial u}{\partial x}\right)^2+2\left(\frac{\partial v}{\partial r}\right)^2-2\frac{v^2}{r^2}+2\left(\frac{1}{r}\frac{\partial w}{\partial\theta}\right)^2\right.$$

$$\left.\left(\frac{\partial v}{\partial x}+\frac{\partial u}{\partial r}\right)^2+\left(\frac{1}{r}\frac{\partial v}{\partial\theta}+r\frac{\partial}{\partial r}(\frac{w}{r})\right)^2+\left(\frac{\partial w}{\partial x}+\frac{1}{r}\frac{\partial u}{\partial\theta}\right)^2\right\rangle\quad(5.28)$$

Appendix 2: Scaling of the Governing Equations

An Order of Magnitude Analysis is conducted here to identify leading order terms in the governing equations. The swirling turbulent wake is a free shear layer flow, and the so-called "thin shear layer hypothesis"

$$\frac{\partial}{\partial x} \sim \frac{1}{L} \ll \frac{\partial}{\partial y} \sim \frac{1}{\delta} \tag{5.29}$$

states that changes in the streamwise direction occur much more gradually than changes in the cross-stream direction. Here L is a streamwise length scale and δ is cross-stream length scale, both to be defined more precisely at a later stage.

A scale for the streamwise velocity in the wake is defined as

$$U \sim U_s \sim (U - U_\infty) \tag{5.30}$$

Note that the wake is characterized by the difference of the mean velocity from the free stream velocity, $(U - U_\infty)$, which is small compared to the free stream velocity if one moves sufficiently far downstream. Therefore

$$U_s \ll U\infty \tag{5.31}$$

The scaling of the streamwise velocity in the governing equations has two distinct cases:

- $U \sim U_s$ when U occurs inside a derivative, i.e., is inside the wake.

- $U \sim U_\infty$ when U is a convective velocity.

This scaling is unique to the turbulent wake and distinguishes the results from the order of magnitude from other free turbulent shear flows such as the jet.

$$
\begin{aligned}
U &\sim U_s \\
\overline{u^2}, \quad \overline{v^2}, \quad \overline{w^2}, \quad \overline{uv} &\sim \overline{u_s^2} \\
\partial/\partial x &\sim 1/L \\
\partial/\partial r &\sim 1/\delta \\
\partial/\partial \theta &= 0 \\
r &\sim \delta
\end{aligned} \tag{5.32}
$$

The order of magnitude scaling is demonstrated in detail for continuity and the three momentum equations. Any equation governing a turbulent shear flow within a "thin shear layer hypothesis", such as turbulent kinetic energy equation and Reynolds stress component equations for the axisymmetric wake with swirl discussed here, can can be scaled using the same procedure.

The averaged continuity equation within the assumptions of incompressibility and axisymmetry is

$$\boxed{\frac{\partial U}{\partial x} + \frac{1}{r}\frac{\partial(rV)}{\partial r} = 0}$$ (5.33)

and the terms occurring in it scale as follows

$$\frac{U_s}{L} + \frac{1}{r}\frac{rV_s}{\delta} \sim 0$$ (5.34)

The scale for the mean radial velocity V_s is then found as

$$V_s \sim U_s\frac{\delta}{L}$$ (5.35)

x-Momentum:

The x-momentum equation will be considered first. Within the assumptions of incompressibility, constant viscosity and axisymmetry, and Reynolds decomposition and averaging the x-momentum equation is

$$U\frac{\partial(U - U_\infty)}{\partial x} + V\frac{\partial(U - U_\infty)}{\partial r} = -\frac{1}{\rho}\frac{\partial P}{\partial x} + \nu\left(\frac{\partial^2 U}{\partial x^2} + \frac{1}{r}\frac{\partial}{\partial r}\left(r\frac{\partial U}{\partial r}\right)\right)$$
$$-\left(\frac{\partial \overline{u^2}}{\partial x} + \frac{1}{r}\frac{\partial}{\partial r}(r\overline{uv})\right)$$ (5.36)

Upon substituting the order of magnitude scaling from equation 5.32 above the x-momentum equation becomes

$$U_\infty\frac{U_s}{L} + U_s\frac{\delta}{L}\frac{U_s}{\delta} \quad \sim \quad ? \quad + \nu\frac{U_s}{L^2} + \nu\frac{1}{r}\frac{1}{\delta}r\frac{U_s}{\delta} + \frac{u^2}{L} + \frac{1}{r}\frac{1}{\delta}ru^2$$ (5.37)

where the symbol " $\sim$ " is used instead of an equal sign to mean "order of magnitude". Equation 5.37 is then multiplied through by $L/U_\infty U_s$ to non-dimensionalize and help group/clear terms

$$1 + \frac{U_s}{U_\infty} \quad \sim \quad ? \quad + \frac{\nu}{LU_\infty} + \frac{\nu}{LU_\infty}\left(\frac{L^2}{\delta^2}\right) + \frac{u^2}{U_\infty U_s} + \frac{u^2}{U_\infty U_s}\left(\frac{L}{\delta}\right)$$ (5.38)

The first fraction in the two viscous terms is identified as the inverse of the Reynolds number, $1/Re_L = \nu/U_\infty L$. The two velocity scalings for the turbulent wake outlined at the beginning of this appendix lead to the second convection term being an order of magnitude smaller than the first convection term. On the right-hand side of the equation, the pressure gradient term is of unknown magnitude at this point in the order of magnitude scaling, hence the " ? ". The second term on the right-hand side

89

(first viscous term) is small compared to the third term (second viscous term), and the fourth term (first turbulence term) is small compared to the fifth term (second turbulence term). The larger of the two viscous terms can be made as small as desired by increasing Reynolds number, in fact a Reynolds number $Re_L > (L/\delta)^3$ would suffice to make it a second order term in this equation. It is easy to see how turbulent free shear flows such as this wake can develop without viscous terms, as they do not have ti satisfy a no-slip condition at a solid wall.

$$1 + \frac{U\!\!\!\!/}{\cancel{U}_\infty} \quad \sim \quad ? \quad + \frac{1\!\!\!\!/}{\cancel{Re}_L} + \frac{1}{Re_L}\left(\frac{L^2\!\!\!\!\!\!/}{\cancel{\delta}}\right) + \frac{u^2\!\!\!\!/}{\cancel{U}_\infty U_s} + \frac{u^2}{U_\infty U_s}\left(\frac{L}{\delta}\right) \tag{5.39}$$

For the larger of the two turbulence terms to remain in the equation, it is required that

$$\frac{u^2}{U_\infty U_s}\left(\frac{L}{\delta}\right) \longrightarrow 1 \tag{5.40}$$

For now, one convection term, the pressure gradient and one turbulence term remain. The magnitude of the pressure gradient term will be derived next.

$$U\frac{\partial(U - U_\infty)}{\partial x} \cong -\frac{1}{\rho}\frac{\partial P}{\partial x} + \frac{1}{r}\frac{\partial}{\partial r}(r\overline{uv}) \tag{5.41}$$

r-Momentum:

Now conservation of radial momentum is considered. Within the assumptions of incompressibility, constant viscosity and axisymmetry, and Reynolds decomposition and averaging the r-momentum equation is

$$U\frac{\partial V}{\partial x} + V\frac{\partial V}{\partial r} - \frac{W^2}{r} = -\frac{1}{\rho}\frac{\partial p}{\partial r} + \nu\left(\frac{\partial^2 V}{\partial x^2} + \frac{\partial}{\partial r}\left(\frac{1}{r}\frac{\partial}{\partial r}(rV)\right)\right)$$
$$-\left(\frac{\partial\overline{uv}}{\partial x} + \frac{\partial\overline{v^2}}{\partial r} - \frac{\overline{w^2} - \overline{v^2}}{r}\right) \tag{5.42}$$

Upon substituting the order of magnitude scaling from equation 5.32 above the r-momentum equation becomes

$$U_\infty U_s\frac{\delta}{L^2} + U_s^2\frac{\delta^2}{L^2}\frac{1}{\delta} - \frac{W_s^2}{r} \quad \sim \quad ? \quad + \nu\frac{U_s}{L^2}\frac{\delta}{L} + \nu\frac{1}{\delta}\frac{1}{r}\frac{1}{\delta}rU_s\frac{\delta}{L}$$
$$+ \frac{u^2}{L} + \frac{u^2}{\delta} + \frac{u^2}{r} \tag{5.43}$$

where the mean azimuthal (swirl) velocity was given its own order of magnitude scaling $W \sim W_s$. The radial coordinate r is assumed to scale with the cross-stream

90

length scale, $r \sim \delta$. Equation 5.43 is then multiplied through by $\delta/U_\infty U_s$ to non-dimensionalize and help group and clear terms

$$
\left(\frac{\delta}{L}\right)^2 + \frac{U_s}{U_\infty}\left(\frac{\delta}{L}\right)^2 + \frac{W_s^2}{U_\infty U_s} \quad \sim \quad ? \quad + \frac{1}{Re_L}\left(\frac{\delta}{L}\right)^2 + \frac{1}{Re_L}
$$
$$
+ \frac{u^2}{U_\infty U_s}\left(\frac{\delta}{L}\right) + \frac{u^2}{U_\infty U_s} + \frac{u^2}{U_\infty U_s}
$$

(5.44)

The second term on the left-hand side is small compared to the first term. If $(\delta/L)^2 \ll W_s^2/U_\infty U_s$, then both the first and second terms on the left-hand side are small compared to the third term. On the right-hand side of the equation, the pressure gradient term is of unknown magnitude. The second term on the right-hand side (first viscous term) is small compared to the third term (second viscous term), and the fourth term (first turbulence term) is small compared to the fifth and sixth terms (second and third turbulence terms). The larger of the two viscous terms scales as $\sim 1/Re_L$ and can be made arbitrarily small by increasing Reynolds number.

$$
\cancel{\left(\frac{\delta}{L}\right)^2} + \cancel{\frac{U_s}{U_\infty}\left(\frac{\delta}{L}\right)^2} + \frac{W_s^2}{U_\infty U_s} \quad \sim \quad ? \quad + \cancel{\frac{1}{Re_L}\left(\frac{\delta}{L}\right)^2} + \cancel{\frac{1}{Re_L}}
$$
$$
+ \cancel{\frac{u^2}{U_\infty U_s}\left(\frac{\delta}{L}\right)} + \frac{u^2}{U_\infty U_s} + \frac{u^2}{U_\infty U_s}
$$

(5.45)

We can now compare the scaling of the azimuthal velocity W_s to the largest turbulence terms: For $W_s^2/U_\infty U_s$ to be of second order compared to the fifth and sixth terms on the right-hand side of equation 5.45 would require that

$$
\frac{W_s^2}{U_\infty U_s} << \frac{u^2}{U_\infty U_s} \quad \text{or:} \quad W_s^2 << u^2
$$

$$
\frac{W_s^2}{u_s^2} \longrightarrow 0
$$

(5.46)

While $W_s^2 << u^2$ is in principal possible for the far, far wake, it is not the expected scaling behavior for the far wind turbine wake, which in this study is defined as $10 \leq x/D \leq 20$. Hence the third term on the right-hand side of equations 5.42, 5.45 remains, and the **reduced r-momentum equation** for the turbulent axisymmetric wake becomes

$$
\boxed{\frac{1}{\rho}\frac{\partial p}{\partial r} = \frac{W^2}{r} - \frac{\partial \overline{v^2}}{\partial r} + \frac{\overline{w^2} - \overline{v^2}}{r}}
$$

(5.47)

Back to $\partial p/\partial x$ and x-Momentum:
Returning to the question of order of magnitude of the pressure gradient in the x—momentum equation: Equation 5.47 can be integrated from r to ∞

$$\int_r^\infty \frac{1}{\rho} dp = \frac{1}{\rho}(p_\infty - p) = \int_r^\infty \frac{W^2}{r} dr - \int_r^\infty \frac{\partial \overline{v^2}}{\partial r} dr + \int_r^\infty \frac{\overline{w^2} - \overline{v^2}}{r} dr \qquad (5.48)$$

which results in

$$-\frac{1}{\rho}(p - p_\infty) = \int_r^\infty \frac{W^2}{r} dr + -\overline{v^2}\Big|_r^\infty + \int_r^\infty \frac{\overline{w^2} - \overline{v^2}}{r} dr \qquad (5.49)$$

where

$$-\overline{v^2}\Big|_r^\infty = -\left(0 - \overline{v^2}\right) \qquad (5.50)$$

Equation 5.49 can be differentiated with respect to x to obtain an expression for the streamwise pressure gradient as

$$-\frac{1}{\rho}\frac{\partial p}{\partial x} = \frac{\partial \overline{v^2}}{\partial x} + \int_r^\infty \frac{1}{r}\left(\frac{\partial \overline{w^2}}{\partial x} - \frac{\partial \overline{v^2}}{\partial x}\right) dr + \int_r^\infty \frac{1}{r}\frac{dW^2}{dx} dr \qquad (5.51)$$

A quick check of the orders of magnitudes of the terms in the $\partial p/\partial x$ expression gives:

$$\left(\frac{1}{\rho}\frac{\partial p}{\partial x}\right) \quad \sim \quad \frac{u^2}{L} + \frac{1}{r}\left(\frac{u^2}{L}\right)r + \frac{W^2}{L} \qquad (5.52)$$

and multiplying equation 5.52 by $L/U_\infty U_s$ yields:

$$\left(\frac{L}{U_\infty U_s}\right)\left(\frac{1}{\rho}\frac{\partial p}{\partial x}\right) \quad \sim \quad \frac{u^2}{U_\infty U_s} + \frac{u^2}{U_\infty U_s} + \frac{W^2}{U_\infty U_s}\left(\frac{W}{U_\infty}\right)\left(\frac{W}{U_s}\right) \qquad (5.53)$$

It is evident that both the turbulence terms, which scale as $u_s^2/U_\infty U_s$, are second order terms when compared to the leading order term in equation 5.39. For now we can assume that $W_s/U_s \sim 1$, and since W_s/U_∞ is small in comparison to the leading order convective term, the third term in equation 5.51 is also of second order.

Equation 5.51 can now be substituted into equation 5.41 to yield the **reduced x-momentum equation** for the turbulent axisymmetric swirling wake

$$\boxed{U_\infty \frac{\partial(U - U_\infty)}{\partial x} = -\frac{1}{r}\frac{\partial}{\partial r}(r\overline{uv}) + \left\{\frac{\partial}{\partial x}\left(\overline{v^2} - \overline{u^2} + \int_0^\infty \frac{1}{r}(\overline{w^2} - \overline{v^2}) + W^2\right)\right\}} \qquad (5.54)$$

The terms in curly brackets are of second order. To first order the reduced x-momentum consists of a balance between the leading order convection term and the leading order Reynolds stress.

Azimuthal (θ)-Momentum:
Finally conservation of azimuthal momentum is considered. Within the assumptions

92

of incompressibility, constant viscosity and axisymmetry, and Reynolds decomposition and averaging the azimuthal (θ)-momentum equation is

$$U\frac{\partial W}{\partial x} + V\frac{\partial W}{\partial r} + \frac{\overline{VW}}{r} = \nu\left[\frac{\partial^2 W}{\partial x^2} + \frac{\partial}{\partial r}\left(\frac{1}{r}\frac{\partial}{\partial r}(rW)\right)\right]$$
$$-\left(\frac{\partial\overline{uw}}{\partial x} + \frac{\partial\overline{vw}}{\partial r} + \frac{\overline{vw}}{r}\right) \tag{5.55}$$

The mean pressure gradient in the azimuthal direction is zero due to axisymmetry. Upon substituting the order of magnitude scaling from equation 5.32 above into the θ-momentum equation it becomes

$$\frac{U_\infty W_s}{L} + U_s\frac{\delta}{L}\frac{W_s}{\delta} + U_s\frac{\delta}{L}\frac{W_s}{\delta} \quad \sim \quad \nu\frac{W_s}{L^2} + \nu\frac{1}{\delta^2}W_s + \frac{u^2}{L} + \frac{u^2}{\delta} + \frac{u^2}{\delta} \tag{5.56}$$

Equation 5.56 is then multiplied through by $L/U_\infty U_s$ to non-dimensionalize and help group and clear terms:

$$1 + \frac{U_s}{U_\infty} + \frac{U_s}{U_\infty} \quad \sim \quad \frac{1}{Re_L} + \frac{1}{Re_L}\left(\frac{L}{\delta}\right)^2 + \frac{u^2}{U_\infty W_s} + \frac{u^2}{U_\infty W_s}\left(\frac{L}{\delta}\right) + \frac{u^2}{U_\infty W_s}\left(\frac{L}{\delta}\right) \tag{5.57}$$

The second and third convection term on the left-hand side are small compared to the first term, which scaled with $U \sim U_\infty$ as convection velocity. The first viscous term on the right-hand side is small compared to the second viscous term, but the larger of the two viscous terms can be made arbitrarily small by increasing Reynolds number. The third term (first turbulence term) is small compared to the fourth and fifth terms (second and third turbulence terms). This yields the **reduced θ-momentum equation** for the turbulent axisymmetric swirling wake

$$\boxed{U_\infty\frac{\partial W}{\partial x} \approx -\left(\frac{\partial}{\partial r}\overline{vw} + \frac{\overline{vw}}{r}\right) = \frac{1}{r}\frac{\partial}{\partial r}(r\overline{vw})} \tag{5.58}$$

where the two leading order turbulence terms can be combined into a single term. The reduced θ-equations states that, to leading order, the change in streamwise transport of azimuthal momentum is equal to the radial transport of radial-azimuthal Reynolds stress $\overline{vw}$. This is the primary transport mechanism for redistributing azimuthal momentum as the swirling wake evolves downstream.